

PHOTOASSOCIATIVE IONIZATION IN COLD RUBIDIUM

by

MARC LAWRENCE TRACHY

B. S., Drake University 2004

---

AN ABSTRACT OF A DISSERTATION

submitted in partial fulfillment of the  
requirements for the degree

DOCTOR OF PHILOSOPHY

Department of Physics  
College of Arts and Sciences

KANSAS STATE UNIVERSITY

Manhattan, Kansas

2008

## ABSTRACT

Many people in the science community are interested in the prospect of cold molecules for such applications as quantum computing and molecular Bose-Einstein condensates. Current methods of production fall short of the requirements for such projects. Photoassociation is a promising technique for forming cold molecules, but is currently facing significant obstacles. By understanding the photoassociation process and utilizing higher excited states, it is hoped that cold molecules can be formed from more easily produced cold atoms. Photoassociative Ionization (PAI) is presented as a means to study excited state molecular dynamics at large internuclear separation, including photoassociation. This thesis presents a number of techniques for studying PAI in cold rubidium and a number of results obtained with the techniques. Excitation pathways for the process are explored in both narrow linewidth (MHz) and ultrafast (fs), large bandwidth (20 nm) domains.

# PHOTOASSOCIATIVE IONIZATION IN COLD RUBIDIUM

by

MARC LAWRENCE TRACHY

B. S., Drake University 2004

---

A DISSERTATION

submitted in partial fulfillment of the  
requirements for the degree

DOCTOR OF PHILOSOPHY

Department of Physics  
College of Arts and Sciences

KANSAS STATE UNIVERSITY

Manhattan, Kansas

2008

Approved by:

Major Professor  
B. D. DePaola

## ABSTRACT

Many people in the science community are interested in the prospect of cold molecules for such applications as quantum computing and molecular Bose-Einstein condensates. Current methods of production fall short of the requirements for such projects. Photoassociation is a promising technique for forming cold molecules, but is currently facing significant obstacles. By understanding the photoassociation process and utilizing higher excited states, it is hoped that cold molecules can be formed from more easily produced cold atoms. Photoassociative Ionization (PAI) is presented as a means to study excited state molecular dynamics at large internuclear separation, including photoassociation. This thesis presents a number of techniques for studying PAI in cold rubidium and a number of results obtained with the techniques. Excitation pathways for the process are explored in both narrow linewidth (MHz) and ultrafast (fs), large bandwidth (20 nm) domains.

# TABLE OF CONTENTS

Table of Contents	v
List of Figures	vii
List of Tables	ix
Acknowledgments	x
Dedication	xi
<b>1 Introduction</b>	<b>1</b>
1.1 Cold molecules . . . . .	1
1.2 Photoassociation . . . . .	2
1.3 Photoassociative Ionization . . . . .	3
1.4 Photoassociative-Dissociative Ionization . . . . .	4
1.5 Ultrafast vs CW . . . . .	5
1.6 Motivation . . . . .	6
1.7 Overview . . . . .	6
<b>2 Theoretical considerations</b>	<b>8</b>
2.1 Production rates . . . . .	8
2.2 Potential curves . . . . .	8
2.3 Nearest neighbors . . . . .	11
2.4 Ultrafast coherent excitation . . . . .	13
<b>3 Experimental setup</b>	<b>15</b>
3.1 Basic apparatus . . . . .	15
3.2 CW PADI-PAI . . . . .	19
3.3 KLS . . . . .	21
<b>4 Results</b>	<b>26</b>
4.1 CW PADI-PAI . . . . .	26
4.2 KLS results . . . . .	33
4.2.1 Spectral amplitude . . . . .	35
4.2.2 L2 delay . . . . .	36
4.2.3 Phase based spectroscopy . . . . .	36
4.2.4 Control . . . . .	48

<b>5</b>	<b>Conclusions &amp; Future Possibilities</b>	<b>53</b>
5.1	CW PAI/PADI . . . . .	53
5.2	KLS PAI . . . . .	53
5.3	Summary . . . . .	54
5.4	Future . . . . .	54
	<b>Bibliography</b>	<b>56</b>
<b>A</b>	<b>Nearest Neighbors</b>	<b>60</b>
<b>B</b>	<b>TOF to KER derivation</b>	<b>62</b>
<b>C</b>	<b>Circuits</b>	<b>64</b>
C.1	Delay stepping . . . . .	64
C.2	Delay Gate . . . . .	66
C.3	Optical beat note lock . . . . .	66
C.4	Pointing Stabilizer (ALPS) . . . . .	70
<b>D</b>	<b>Data Acquisition Software</b>	<b>73</b>
<b>E</b>	<b>Locking the Lasers</b>	<b>75</b>
<b>F</b>	<b>Automatic Laser Pointing Stabilizer (ALPS) Manual</b>	<b>77</b>
F.1	Optics . . . . .	77
F.2	Connection . . . . .	79
F.3	Operation . . . . .	79

# LIST OF FIGURES

1.1	Photoassociation explained . . . . .	2
1.2	Photoassociative Ionization in Na MOT . . . . .	4
1.3	Schematic representation of PADI . . . . .	5
2.1	Model incubation time . . . . .	9
2.2	Potential curves . . . . .	10
2.3	Gallagher-Pritchard model prediction . . . . .	12
2.4	Sample model calculation . . . . .	14
3.1	Vacuum chamber contents . . . . .	16
3.2	Basic laser locking . . . . .	17
3.3	Rb hyperfine structure . . . . .	18
3.4	CW PADI PAI experimental setup . . . . .	20
3.5	Sample CW TOF spectrum . . . . .	21
3.6	KLS basic electronics . . . . .	23
3.7	Simplified schematic of the KLS and Dazzler setup . . . . .	25
4.1	Count rates as functions of L1 and L2 powers . . . . .	27
4.2	CW PAI TOF spectra . . . . .	29
4.3	PAI potential curves . . . . .	30
4.4	PADI KER spectrum . . . . .	32
4.5	Relevant potential curves for PADI . . . . .	34
4.6	Spectral notches configuration . . . . .	35
4.7	KLS L2 delay . . . . .	37
4.8	Sample pi edge phase profile . . . . .	38
4.9	TOF spectrum <i>versus</i> pi edge wavelength . . . . .	39
4.10	Counts <i>versus</i> pi edge wavelength . . . . .	40
4.11	Theoretical pi edge results . . . . .	41
4.12	$\pi/2$ step phase sample . . . . .	42
4.13	Atomic ion counts <i>versus</i> $\pi/2$ edge wavelengths . . . . .	43
4.14	TOF spectrum <i>versus</i> $\pi/2$ step number . . . . .	45
4.15	Counts <i>versus</i> $\pi/2$ step edge positions . . . . .	46
4.16	Theoretical counts <i>versus</i> $\pi/2$ step positions . . . . .	47
4.17	Simple calculation for second order phase . . . . .	49
4.18	Temporal shape of a sinusoidal phase . . . . .	50
4.19	Sinusoidal phase counts . . . . .	51
4.20	Sinusoidal phase theory results . . . . .	52

A.1	Nearest neighbors . . . . .	61
C.1	Schematic for the programmable delay stepper . . . . .	65
C.2	Schematic for the delay gate . . . . .	67
C.3	Block diagram for the optical beat note lock (beat box) . . . . .	68
C.4	Schematic for the optical beat note lock (beat box) . . . . .	69
C.5	Schematic for the Automatic Laser Pointing Stabilizer (ALPS) . . . . .	71
E.1	Laser locking signals . . . . .	76
F.1	ALPS setups . . . . .	78
F.2	ALPS detector . . . . .	80
F.3	Back panel of the ALPS . . . . .	81
F.4	Front panel of the ALPS . . . . .	82
F.5	ALPS circuit board . . . . .	84



# LIST OF TABLES

2.1	Hund's cases . . . . .	10
4.1	$\pi/2$ step number to wavelength . . . . .	44
C.1	Optical beat lock possibilities . . . . .	70

## Acknowledgments

I am grateful for the help and advice of many people in completing this work. I hate writing though, so I'll keep this short. My adviser, Brett DePaola (note the capital 'P'!), has been a huge source of knowledge, advice, general mentoring and good food (beamtime doughnuts are the best food in the world). He taught me more of electronics than I thought I knew I wanted to know. I don't agree with his political stances on a number of things, but that just makes afternoon discussions more interesting. My labmates throughout the years have influenced my development, for better or worse, almost as much as Brett. Alan Camp (How) taught me everything about the old system, data acquisition in XSYS, CAMAC and NIM electronics, optics and vacuums. Mudessar Shah tried to teach me patience. . . I think I failed. Alina Gearba taught me the value of the word "punk" as a general purpose descriptor. Goga Veshapidze always thinks outside what I would have considered, often frustrating me to no end. Hyoung-Uk Jang has been a diligent student, always asking questions; he's the next generation of the MOTRIMS line.

The people outside our group have always been very helpful. Scott Chainey was instrumental in the production of the electronics, including putting a lot of time into laying out the circuits and making sense of the crazy diagrams I handed him. Mike Wells was always willing to help out with even the strangest of requests, including checking out a turbopump I thought was singing (that turned out to be OK). Al Rankin, Hiroki Mashiko, and recently, He Wang have performed miracles in getting us a good ultrafast beam all tuned up the way we like it.

My friends and family have been a huge support in this. I've complained a lot to them about all sorts of things, and they've managed to endure it. Very impressive, I'd say. My parents and sister especially helped me to stay sane during this. . . interesting experience. I thought I was going to never finish the writing of this thesis, but I found the music of "Ali Project" to be an upbeat inspiration. I don't know what most of the lyrics are, but it's fun anyway!

This work was supported by the Chemical Sciences, Geosciences, and Biosciences Division, Office of Basic Energy Sciences, Office of Science, U.S. Department of Energy.

## Dedication

*To my family. Thanks for your support. I love you; I'm proud of you; and I miss you.*

# Chapter 1

## Introduction

### 1.1 Cold molecules

Developments in atom cooling and trapping have made it possible to work with small clouds of atoms in the gaseous state at temperatures below a nanokelvin<sup>1</sup>. The same cannot be said for molecules. It is currently unknown how to obtain clouds of gas molecules in their electronic, vibrational and rotational ground states with temperatures below a few tens of millikelvin. In atoms, the most convenient way to cool and trap is the Magneto Optical Trap (MOT)<sup>2,3</sup>. This requires a small number of lasers tuned near hyperfine resonances in the target atoms, as well as a weak magnetic field gradient. Applying the same technique to molecules has resulted in failure, due mainly to the complicated level structure of molecules. There are no convenient closed cycling transitions in molecules. This is largely due to the fact that there is no strict selection rule for the vibrational quantum number<sup>4</sup>.

There are other methods of cooling, which work very well for molecules. One is to rapidly expand a gas. This is generally accomplished by forcing the gas through a small aperture, a nozzle, at high velocity. While this method is adequate for Cold Target Recoil Ion Momentum Spectroscopy (COLTRIMS)<sup>5</sup>, its ultimate low temperature limit of a few hundreds of millikelvin<sup>6</sup> leaves something to be desired. Another method is called Stark deceleration. This method uses electric field gradients to cool a molecular beam for loading into an electrostatic trap. Temperatures of 50 mK can be achieved<sup>7</sup>. A third technique called buffer gas cooling, used by Doyle's group, passes a gas of atoms or molecules over liquid helium to cool to temperatures down to a few hundred millikelvin<sup>8</sup>.

Since cooling warm molecules has proven to be difficult, the idea of creating molecules from cold atoms, which has shown great promise, is attractive. One method of doing this association is to tune a quantum degenerate gas, such as a Bose-Einstein Condensate (BEC), through a Feshbach resonance<sup>9,10</sup>. This produces very cold molecules, on the order of the temperature of the constituent atoms (typically several tens of nanokelvin), but has the disadvantage that the molecules are created in very high vibrational states, near

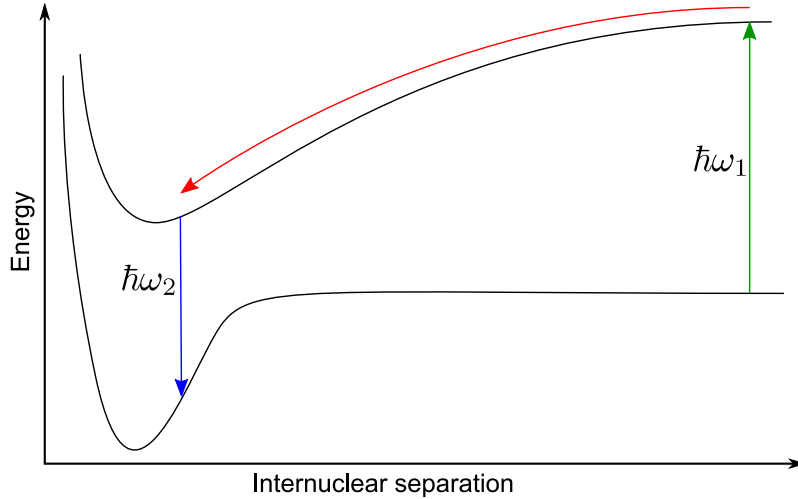


Figure 1.1: In photoassociation, an atom pair is excited from the ground electronic state with photon  $\hbar\omega_1$ . The atoms then move together under the influence of the sloping upper potential curve until they emit a photon  $\hbar\omega_2$ , which has a frequency less than  $\omega_1$ , and are trapped in the bound lower electronic state.

the dissociation limit, making them inappropriate for many uses<sup>(1)</sup>. Also, if one is merely interested in microkelvin temperatures, it is troublesome to make a quantum degenerate gas.

## 1.2 Photoassociation

Another technique for creating cold molecules from cold atoms which has shown some promise is photoassociation (PA)<sup>11–13</sup>. This process is shown schematically in Fig 1.1. It consists of exciting the target atom pair with photon  $\hbar\omega_1$  to a higher, steeper, potential curve so the electrostatic interaction is strong enough to pull the atoms close together, then letting (or forcing) the new molecule to decay, emitting photon  $\hbar\omega_2$  to the electronic ground state, stranding the molecule in the bound electronic ground state. In the literature, the designation PA is often used to refer to the first step in this process, which results in a bound molecule in an excited electronic state. Some confusion exists because it is also used, in a restricted sense, for the process that results in bound molecules in the electronic ground state. *Here, the former process, resulting in excited bound molecules, will be referred to as PA\*, while the latter, more restricted definition will be referred to as PA.*

PA has been observed for quite some time in the form of loss from a MOT of  $^{85}\text{Rb}$ <sup>14</sup>. This particular isotope of Rb has a hyperfine structure in its molecular curves that lends itself to photoassociation at frequencies very near resonance (1 to 3 linewidths from resonance).

<sup>(1)</sup>Ospelkaus *et al.*<sup>10</sup> report advancements in the area of bringing molecules created with a Feshbach resonance down lower into the potential well. They have, so far, achieved depths of a few GHz, which is still considered a high vibrational state.

This small detuning is always present in the trapping lasers in a MOT. It is interesting to note that the more easily trapped  $^{87}\text{Rb}$  does not seem to exhibit this behavior<sup>(2)</sup>. To get similar trap losses with that isotope, experimenters had to introduce a catalysis, or photoassociation, laser detuned from the atomic resonance by orders of magnitude more than the trapping lasers<sup>14</sup>.

The discovery of PA in cold atomic gasses led to the development of photoassociation spectroscopy. In photoassociation spectroscopy, one traps cold atoms and uses a photoassociation laser that is detuned from atomic resonance by a variable amount. The production of molecules is usually inferred from trap loss, but is also often measured by Resonantly Enhanced Multi-Photon Ionization (REMPI)<sup>16,17</sup>. Molecular production is measured as a function of the photoassociation laser frequency. By looking for and measuring the frequencies of resonances, where production is enhanced, it is possible to map out the vibrational energy structure of the excited state of the molecule. This technique results in extremely high resolution maps of the potential curves<sup>15,18</sup>, and can even give significant information about the atoms, such as lifetime, with unprecedented precision<sup>19</sup>.

While photoassociation is a powerful tool to create cold molecules and to study the long range behavior of the low excited states of a molecule, it is difficult to detect slow neutral molecules in small numbers. Instead, it is possible to photoionize the molecules from the electronic ground state. Then an electric field can be used to extract the ions and common tools such as micro channel plates can detect them with high efficiency.

### 1.3 Photoassociative Ionization

A process related to PA takes this idea a step further. In this process, the atoms are excited and associated ( $\text{PA}^*$ ) and subsequently ionized *without*<sup>(3)</sup> going back down to the electronic ground state. The resulting cold molecular ions are easily counted. This process is called photoassociative ionization (PAI), since the ionization is part of getting to the final state, without going through a stable intermediate state.

The first observations of PAI were made in a sodium MOT<sup>20,21</sup>. In sodium, the structure is such that the  $\text{Na}_2^+$  potential curve dips below the combined energy of two atoms in the  $3\text{P}_{3/2}$  state as shown in Fig 1.2, which is populated in large numbers in the trapping process. After the excitation of one atom in the pair, the electrostatic interaction brings the two atoms closer together until the second transition in the molecule is resonant with the trapping laser, which is tuned a few linewidths to the red of the atomic transition. At this point, a second photon is absorbed, and the atoms accelerate toward each other until there is a curve crossing with the  $\text{Na}_2^+$  curve, at which point, the molecule ionizes and is bound

---

<sup>(2)</sup>Though Kemmann *et al.*<sup>15</sup> claim to see significant production of  $^{87}\text{Rb}_2$  in MOT, others that have looked for it have not detected it, and there is reason to believe that they are detecting  $\text{PA}^*$  as opposed to PA proper. A good explanation for the lack of *in MOT* production of  $^{87}\text{Rb}_2$  is given by Hoffmann *et al.*<sup>14</sup>

<sup>(3)</sup>While the term PAI is sometimes used to refer to the process where a molecule is ionized from its ground state, I consider this usage misleading and will not be using it.

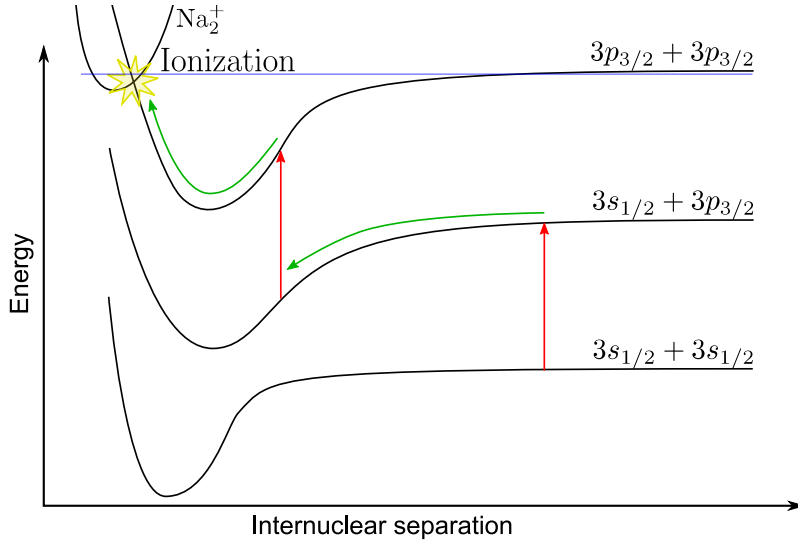


Figure 1.2: In photoassociative ionization in sodium, a single laser color is sufficient. The first photon is absorbed, and the atoms in the molecule move toward each other until the second photon is in resonance, which, due to the curvature of the levels, will not be at the same internuclear separation at which the first photon was resonant. The second photon is absorbed, taking the molecule to a state comprised, asymptotically, of two atoms in the  $3p_{3/2}$  state. The molecule now has a total energy indicated by the blue line. The atoms continue to move closer to each other until the curve they are on crosses the curve labeled  $\text{Na}_2^+$ , at which point they lose an electron.

and trapped in the electronic ground state of the ion. This process, in which ionization happens during a curve crossing is called collisional PAI.

Another form of PAI is called direct PAI. In this process,  $\text{PA}^*$  is followed by direct photoionization of the excited molecule. The resulting ion will be bound and in the ground electronic state, if the final photon has the proper frequency. An example of direct PAI has been reported by Leonhardt *et al.*<sup>22</sup>, in which two radically different color lasers were used. This is one of the few examples of PAI in rubidium. In this thesis which is concerned with collisional PAI in rubidium, the term PAI will refer only to collisional PAI, and not to direct PAI.

## 1.4 Photoassociative-Dissociative Ionization

A process similar to PAI except that the auto-ionization takes the molecule to a *dissociative* curve, to date, has not been observed outside of this work. The process is shown schematically in Fig 1.3, and involves excitation to a bound state *above* the dissociated ion energy limit. As the atoms in the molecule move closer together, they approach the curve crossing with a dissociative curve of the electronic ground state of the molecular ion and gain kinetic energy. Any time before this curve crossing, the molecule can auto-ionize, putting it on the dissociative curve with some potential energy above the dissociation limit. This energy

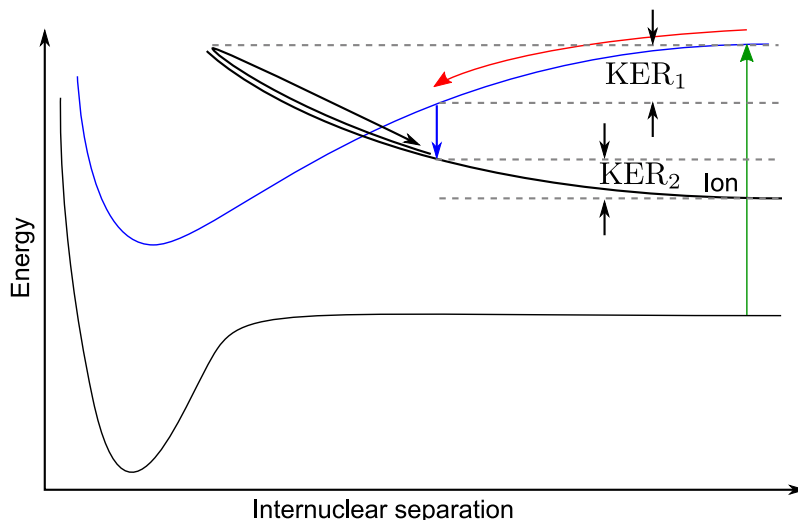


Figure 1.3: Schematic representation of PADI. The excitation represented by the green arrow can consist of many photons and go through many levels. Once excited, the atoms in the molecule move closer to each other (red arrow), until they are close enough to auto-ionize (blue arrow), at which point they slide down the dissociative potential curve, and dissociate with a kinetic energy release ( $KER = KER_1 + KER_2$ ) as shown.

is converted to kinetic energy of the dissociated atom and ion and is added to the kinetic energy already accumulated; it can be measured simply by measuring the momentum of the ion produced. This process has been named Photoassociative-Dissociative Ionization (PADI)<sup>23</sup>. PADI will be discussed in this work, but is not prominently featured.

## 1.5 Ultrafast vs CW

Traditionally, PAI has been performed with narrow linewidth continuous wave (CW) lasers. This has the advantage of having a wavelength that is known to better than a hundredth of a nanometer. The recent development of powerful, robust, ultrafast, wide bandwidth lasers presents another option for such studies.

One of the main disadvantages of CW lasers is that the frequency tuning range tends to be very narrow, allowing for sometimes only one fine structure split level to be accessed with a particular laser. Also, a CW laser is designed to output only one frequency at a time. To excite a large number of transitions, then, requires a large number of lasers. This is expensive both in cost of purchasing such lasers and also in the large amount of labor that goes into keeping them at the proper frequencies and all aligned on the same target. Ultrafast lasers, with their large bandwidth, typically spanning tens of nanometers, are able to access a large number of transitions at one time.

In many instances, it is desirable to phase-lock all of the lasers in an experiment. Such conditions are often needed in coherent control experiments. Phase locking CW lasers that have a difference in frequencies of more than a few gigahertz (equivalent to about 0.01 nm



in the near infrared) is troublesome, and often requires additional lasers to bridge the gap. By the very nature of an ultrafast laser, however, all of the frequency components are phase locked to each other. This greatly simplifies coherent control experiments.

A disadvantage of using wide bandwidth ultrafast lasers is that, with all of those frequency components interacting with the target, it can be difficult to tell exactly which of a number of closely spaced states is involved with a particular phenomenon. A CW laser, with its well defined frequency will only interact with a very small number of closely spaced states, often only one. In order to utilize the benefits and minimize the disadvantages of each of the kinds of lasers, this work makes use of both, often simultaneously.

## 1.6 Motivation

Any scientific work must be motivated by something. This one is no exception. As discussed previously, PAI can be used to investigate PA which has promising implications for the realization of trapping cold neutral molecules. These molecules are sought after for a number of reasons. Cold hetero-nuclear diatomic molecules have been proposed as a good candidate for scalable quantum computing and quantum information<sup>24</sup>, which are hot fields of interest to many scientific communities. Additionally, after the great success of the dilute gas Bose-Einstein condensate (BEC), there is at least one group working on creating molecular BECs<sup>10</sup>. Current methods of production have proven inadequate in manufacturing vibrationally, rotationally and translationally cold molecules. Photoassociation, as traditionally done with the first excited state of the molecule has limitations, and has been shown theoretically to be most efficient with pulses that are very difficult to produce<sup>25</sup>. We believe that going to higher electronically excited states and exploiting larger curvatures of the potential curves and longer lifetimes will improve production efficiency. A good understanding of these higher excited states would be invaluable to researchers pursuing this line of work.

It is also hoped that the work done here will extend the field of photoassociative ionization spectroscopy, which can yield significant understanding of homo-nuclear and hetero-nuclear diatomic molecules to higher excited states. The higher excited states, which are not usually probed to date, are particularly well suited to PAI spectroscopy. Such states are hard to probe with traditional PA spectroscopy, and no other techniques work with the precision that the close level spacing at large internuclear separations requires.

Also, this lab already has a very good ultrafast laser, and a lot of experience with narrow linewidth CW lasers. It seems prudent to take advantage of this co-location of the two technologies that make us uniquely positioned to do this kind of study.

## 1.7 Overview

The overall goal of this thesis is to demonstrate a number of effective techniques for studying and controlling the PAI process in both ultrafast and narrow linewidth regimes. A number

of experiments were done to explore the PAI and PADI processes in cold Rb in order to fulfill this goal. These can be separated into two broad classifications: CW laser PAI, in which the atoms are excited with quasi-CW lasers, and the entire process happens on the nanosecond time scale; and ultrafast (KLS) PAI, in which the atoms are excited by a combination of an ultrafast Ti:Sapphire laser near 800 nm and a quasi-CW laser near 1529 nm.

The CW laser experiments are centered around determining the excitation pathway for the PAI process with lasers tuned very near atomic resonance. Studies include determining the number of photons of each wavelength that are needed for the process by examining the count rate as a function of intensity, and determining the photon absorption order by controlling the timing of laser pulses. PADI is also studied briefly to determine the kinetic energy release in the process with the wavelengths in use.

The KLS PAI experiments are further divided into two groups. The first group is oriented toward determining the excitation pathway and the relevant wavelengths of the ultrafast pulse in the process. This is done by examining the effects of timing between the KLS pulse and the quasi-CW pulse, measuring the effects of spectral notches, or holes, covering atomic resonances in the KLS pulse, and a novel spectroscopic technique using the *phase* as a function of frequency of the ultrafast pulse to find important wavelengths. The second group of experiments is designed to demonstrate control of the PAI process with simple spectral phase profiles of the ultrafast pulse.

# Chapter 2

## Theoretical considerations

### 2.1 Production rates

It is reasonable to break the production rate of either PAI or PA up into a number of factors. One obvious way of doing this is

$$\gamma = N (P_{available}) (\gamma_{excitation}) (P_{survival}) (P_{finishing}) \quad (2.1)$$

where  $\gamma$  is the production rate,  $N$  is the total number of atoms,  $P_{available}$  is the probability of an atom having an available (meaning within a given range of distances away) partner for excitation,  $\gamma_{excitation}$  is the rate that available pairs of atoms will be excited,  $P_{survival}$  is the probability that an excited molecule will survive to the appropriate internuclear separation without spontaneous emission, and  $P_{finishing}$  is the probability that a molecule at the appropriate internuclear separation will form the appropriate state. In PA,  $P_{finishing}$  will be the probability of emission of a photon dropping the molecule into the desired state; in PAI, it will be the probability of autoionization into the desired state and is expected to be near unity.

It is instructive to visit each of these terms in more detail separately.

### 2.2 Potential curves

As soon as the molecules are excited to a higher lying electronic state, they will begin to decay. Thus, the time spent in the excited state will have a large impact on the desired production rate, if this time is comparable to the lifetimes of the states. So, for a given molecular species,  $P_{survival}$  will be directly related to the curvature of the excited state curve or curves (which will increase acceleration, thereby reducing the time required), as well as inversely to the internuclear separation at which the excitation occurs (which would increase the distance to be traversed and thereby the time required). It is also important that the slope of the diabatic curves decreases with increasing internuclear separation, giving more importance to the shape of the curves in the large internuclear separation regime.

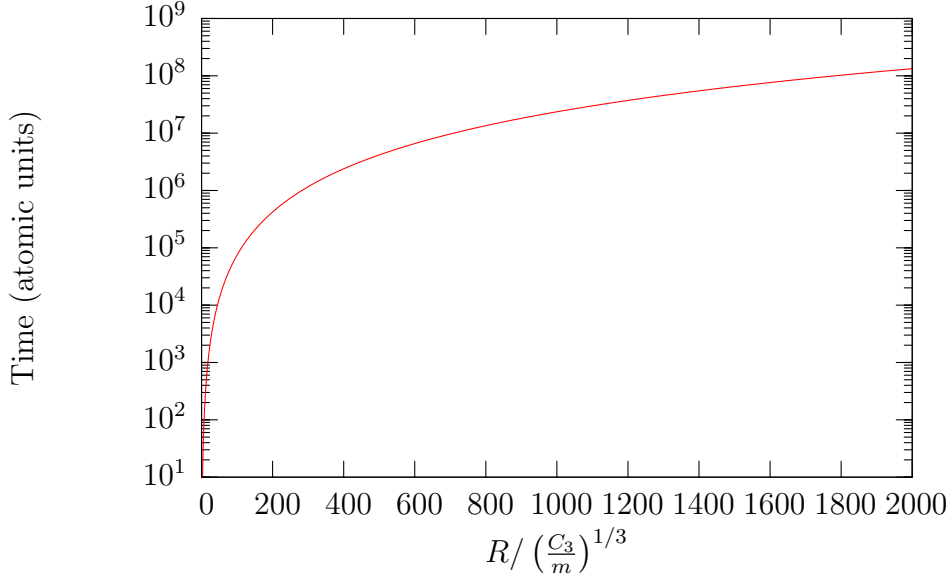


Figure 2.1: A model calculation for the incubation time on a  $1/R^3$  curve.  $R$  is the internuclear separation and  $m$  is the mass of the particle.

The shape of a *diabatic* potential curve, at large internuclear separations can be approximated by

$$E = E_0 + \frac{C_1}{R} + \frac{C_2}{R^2} + \frac{C_3}{R^3} + \dots \quad (2.2)$$

where  $E_0$  is the asymptotic atomic energy,  $R$  is the internuclear separation, and  $C_n$  are coefficients belonging to a given state. For most curves, some of the first coefficients are identically zero. The general rules for which term is the first nonzero term (aside from the  $E_0$  term) are as follows. ion+ion:  $C_1$ ; ion+atom:  $C_2$ ;  $s+p$ ,  $p+d$ , and any other dipole allowed transition:  $C_3$ ;  $s+d$  and  $p+p$ :  $C_5$ ;  $s+s$ :  $C_6$ <sup>4</sup>. Since this work does not deal with atoms having larger angular momentum, these rules will be sufficient. At large internuclear separations, then, there will be very little attractive force between the atoms in a  $\text{Rb}_2$  molecule, since the force is just  $-\partial E/\partial R$ . To get significant motion in the internuclear coordinate, will therefore require going to states with more curvature. A simple classical model calculation, in which Newton's second law is integrated for the potential curves, gives the time required to move from an internuclear separation  $R$ , to small internuclear separations (taken in the model to be 0) on a  $1/R^3$  potential; the result is given in Fig 2.1. This time has been dubbed the incubation time of the system, and can be measured in experiments.

While the diagrams in sections 1.2 and 1.3 are quite simple, the reality of molecules, especially at large internuclear separations, is significantly more complicated. Figure 2.2 shows the potential energy curves<sup>15</sup> of the  $\text{Rb}_2$  molecule at long range and small detuning for only a single fine structure split asymptotic limit, namely the  $5p_{3/2} + 5s_{1/2}$ . As the angular momentum of each atom increases, the number of states also increases.

There are a number of common ways of coupling the angular momenta inside the molecule

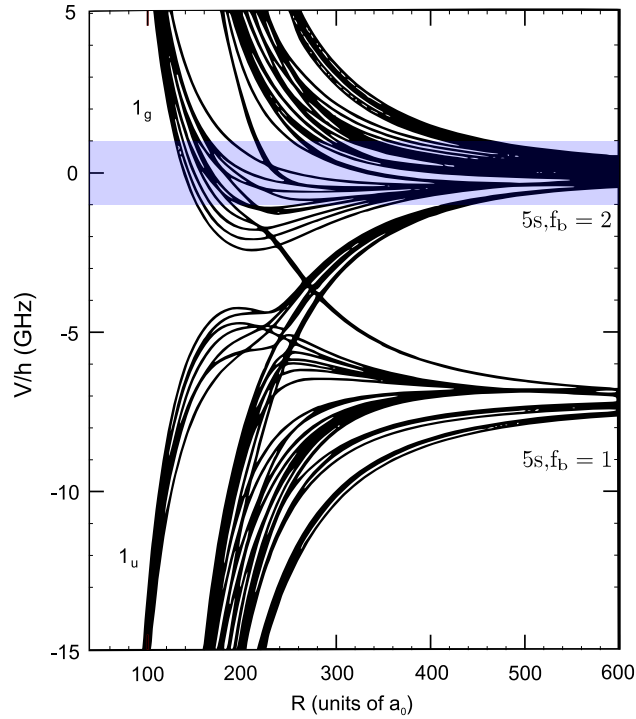


Figure 2.2: Potential energy curves for the  $5p_{3/2} + 5s_{1/2}$   $\text{Rb}_2$  states. Notice the high density of states in the blue shaded area, where some of this work takes place. Adapted from Kemmann *et al.*<sup>15</sup>

Hund's Case	Description
(a)	Electrostatic $\gg$ Spin-Orbit $\gg$ Rotation
(b)	Electrostatic $\gg$ Rotation $\gg$ Spin-Orbit
(cs)	Spin-Orbit $\gg$ Electrostatic $\gg$ Rotation
(d)	Rotation $\gg$ Electrostatic $\gg$ Spin-Orbit
(e)	Spin-Orbit $\gg$ Rotation $\gg$ Electrostatic

Table 2.1: Hund's cases

to get the appropriate quantum numbers; these are called Hund’s cases. Each Hund’s case is useful for different situations. Table 2.1 summarizes when these cases are applicable. Notice that the hyperfine interaction is not mentioned in the table. None of the Hund’s cases are appropriate when the hyperfine interaction is significant compared to the electrostatic interaction. At small photoassociation laser detunings, less than a few gigahertz, the hyperfine interaction can be larger than the electrostatic term which governs the curvature of molecular potential curves. That said, the literature still often refers to states by their Hund’s case (c) notation. As shown in Fig 2.2, many states belong to each of the  $1_g$  and  $0_u$  curves, while beyond 200 atomic units curves cannot be uniquely identified with any of the Hund’s case (c) states.

One convention that is used to identify hyperfine states in molecules, for example, in Kemmann *et al.*<sup>15</sup>, is characterized by the identifier  $j(\phi p)$  where  $\phi$  is the projection of the total angular momentum,  $\vec{F}$ , on the internuclear axis (this is very analogous to  $\Omega$  in Hund’s case (c) notation, but includes nuclear spin);  $p$  is total parity and  $j$  is a counting index to distinguish the different states with the same symmetry. In the special case that  $\phi = 0$ , another identifier is tacked on, to represent the Kronig symmetry or the parity with respect to reflection in the plane of rotation<sup>26</sup>.

For molecular states above the  $5s+5p_{3/2}$  in Rb, high resolution calculations have not been done. Indeed, the only calculations to date for small detunings have neglected spin-orbit coupling, as well as nuclear spin and use Hund’s case (a) couplings, leaving significantly fewer states than would be resolvable at current experimental resolutions. While these calculations are useful for qualitative understanding of experimental data, they are insufficient for making any sort of quantitative predictions.

## 2.3 Nearest neighbors

$P_{available}$  is dominated by the distribution of the distances between atoms. It is straightforward to calculate the statistical distribution of distances from a given atom to its nearest neighbors. This distribution is derived in appendix A and is given by

$$P_{available}(R)dR = 4\pi\rho R^2 dR \exp\left(-\frac{4}{3}\rho\pi R^3\right) \quad (2.3)$$

where  $R$  is the internuclear separation between nearest neighbors and  $\rho$  is the number density of the cloud of atoms, assumed to have constant density. From this, it is apparent that it is much more probable to have pairs of atoms with a larger internuclear separation. Therefore,  $P_{available}$  will increase with the internuclear separation at the time of excitation, up to about  $0.6\rho^{1/3}$ , which, for typical MOT densities, is roughly  $5\ \mu\text{m}$ . This is in opposition to the relationship based on lifetimes and curvature of potential curves.

A simple model, for a single curve taking into account both  $P_{available}$  and  $P_{survival}$  for a  $1/R^3$  potential is known as the Gallagher-Pritchard model<sup>27</sup> which is given a nice, short, treatment by Hoffmann *et al.*<sup>14</sup>. A plot of the Gallagher-Pritchard model prediction for Rb is given in Fig 2.3.

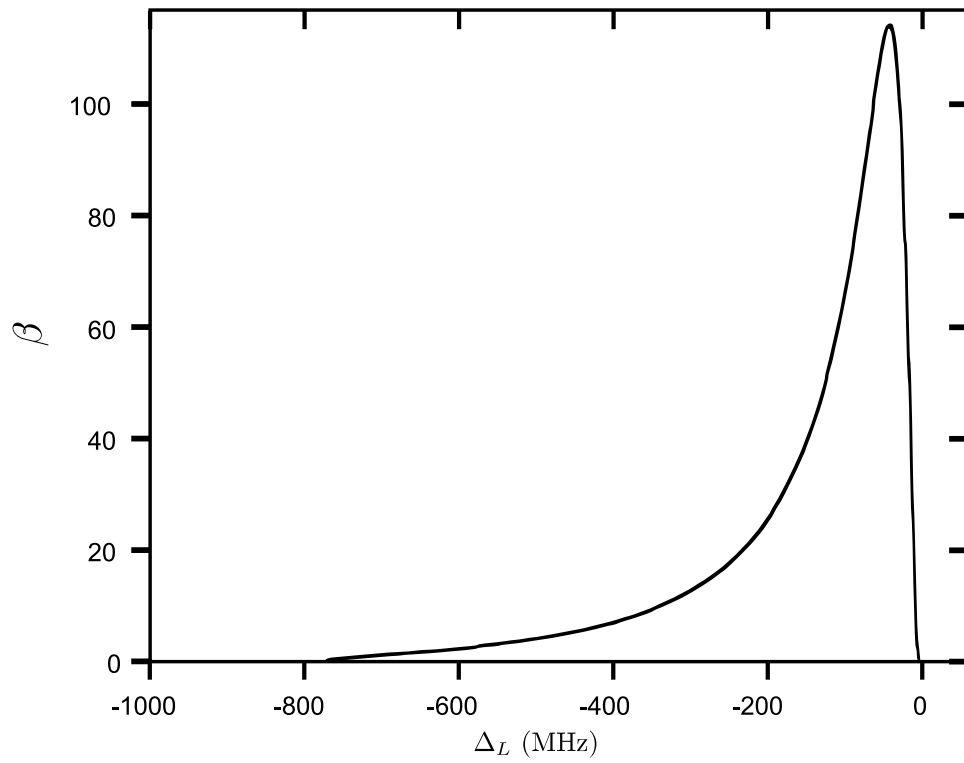


Figure 2.3: A plot of the Gallagher-Pritchard model predicted PA rate,  $\beta$  as a function of detuning from atomic resonance. Taken from Hoffmann *et al.*<sup>14</sup>.

## 2.4 Ultrafast coherent excitation

In the case of an ultrafast laser, there are a number of things that can be done to modify  $P_{excitation}$ . One example, with huge potential and flexibility, is to shape the pulse in the frequency domain, both in phase and in amplitude. Such a shaped pulse has an electric field in the frequency domain of the form

$$E(\omega) = A(\omega)e^{-i\phi(\omega)} \quad (2.4)$$

where  $A(\omega)$  and  $\phi(\omega)$  are arbitrary functions. While this is equivalent to shaping the pulse in the time domain, related by a Fourier transform, it is more common to consider the shaping in the frequency domain, with rare exceptions.

Simple second order perturbation theory dictates that the excitation probability amplitude  $a$  from a ground state  $g$  to a final state  $f$  via an intermediate state  $i$  is given by

$$a(t) = -\frac{1}{\hbar^2}\mu_{fi}\mu_{ig} \int_{-\infty}^t \int_{-\infty}^{t_1} e(t_1)e(t_2) \exp(i\omega_{fi}t_1) \exp(i\omega_{igt_2}) dt_2 dt_1, \quad (2.5)$$

where  $e$  is the electric field in the time domain,  $\mu_{ij}$  is the dipole matrix element coupling states  $i$  and  $j$  and  $\hbar\omega_{ij}$  is the energy difference between levels  $i$  and  $j$ .

In the case of a linear chirp, which is a second order term in the phase *versus* frequency, Merkel *et al.*<sup>28</sup> have derived a closed form expression for the excitation probability amplitude based on the complex error function.

Dudovich *et al.*<sup>29</sup> demonstrate the usefulness of a simple model, which is the second order perturbation theory result, in describing the effects of the ultrafast laser pulse, shaped in the frequency domain, on the resonant excitation rate in atoms. The simplicity of the model is its most endearing feature. For resonant (or near resonant) two photon absorption from ground state  $g$  to final state  $f$  via intermediate states  $i$ , it has the simple form

$$a \approx \sum_i -\frac{1}{i\hbar^2}\mu_{fi}\mu_{ig} \left[ i\pi E(\omega_{ig})E(\omega_{fg} - \omega_{ig}) + \wp \int_{-\infty}^{\infty} \frac{E(\omega)E(\omega_{fg} - \omega)}{\omega_{ig} - \omega} d\omega \right] \quad (2.6)$$

where subscripts designate the relevant levels,  $a$  is the probability amplitude of excitation to the final state,  $\mu$  is the dipole matrix element and  $\wp$  is the Cauchy principal value. The first term in the square brackets accounts for the resonant excitation, while the second term in the square brackets accounts for the near resonant excitation.

This model makes some intuitive sense. A classical driven oscillator will have a displacement that is in phase with the driving force when the oscillator is driven at a frequency far below the resonant frequency, like the model. At the resonant frequency, the displacement is  $\pi/2$  out of phase with the driving force, just like the resonant term in the model. Far above the resonant frequency, it is  $\pi$  out of phase with the driving force, again, like the model. Also, the amplitude of oscillations in a classical oscillator will drop as the frequency difference between the driving force and the resonant frequency increases, much like in the model.



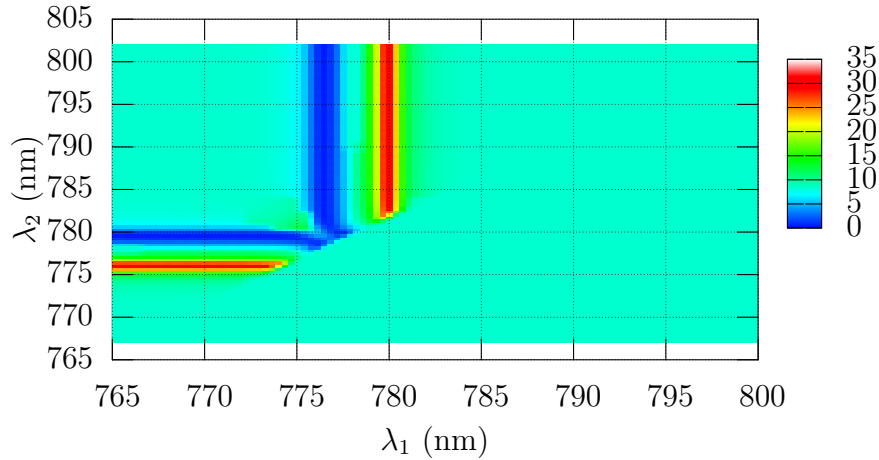


Figure 2.4: Sample model calculation for a pulse with a phase given by Eq 2.7, where the approximately-equal-to sign represents the finite rise and fall derivatives to preserve continuity. The first transition has a wavelength of 780 nm, and the second transition has a wavelength of 776 nm.

Since this model is a single integral, and requires little knowledge of the structure of the system of interest, it is very nice for quick calculations to determine the usefulness of a particular experiment in gaining information, since  $P_{excitation}$  is simply the magnitude squared of  $a$  times some constant for any further excitation, which would presumably not be changed while changing the shape of the ultrafast pulse. An example of a calculation made for a pulse shaped such that

$$\phi(\omega) \approx \begin{cases} 0 & \omega < \lambda_1 \\ -\frac{\pi}{2} & \lambda_1 < \omega < \lambda_2 \\ 0 & \lambda_2 < \omega \end{cases} \quad (2.7)$$

is shown in Fig 2.4.

Second order perturbation theory is valid for small driving fields, or for off resonant excitation. In this thesis, the ultrafast experiments are neither weak field nor off resonant. Therefore, the model is not expected to always give quantitative agreement with the experiments. Despite this, the model is useful in understanding the physics, and will be used. A more robust approach would be to solve the appropriate optical Bloch equations. However, this has the disadvantages of longer computation time, less flexible (system dependent) formulation and a loss of intuition, compared to the second order perturbation theory of Eq 2.6.

# Chapter 3

## Experimental setup

### 3.1 Basic apparatus

The basic apparatus used in these experiments is a  $^{87}\text{Rb}$  magneto-optical trap recoil ion momentum spectroscopy (MOTRIMS) setup. This setup, and its basic uses, has been documented elsewhere<sup>30–36</sup>.  $^{87}\text{Rb}$  atoms are trapped and laser cooled to about  $120\ \mu\text{K}$  in a vapor cell loaded MOT. The vapor cell is actually a stainless steel vacuum chamber. The trapping region is inside of an electrostatic momentum spectrometer. Any ions produced in the MOT are extracted by the electric field and detected by a micro-channel plate and resistive anode 2-dimensional position sensitive detector. This arrangement, shown in Fig 3.1, and the time and spatial focusing configuration of the spectrometer allows for high resolution 3-dimensional momentum measurements of any ions produced in the MOT. The spectrometer also allows easy separation of  $\text{Rb}^+$  and  $\text{Rb}_2^+$  ions via time of flight. This separation is critical for many measurements, especially those using ultrafast pulses, with relatively high intensity lasers. This method of time of flight measurement also allows accurate determination of the “incubation time” which is defined as the time from the initial laser pulse input into the system to the time of ionization, limited in resolution to the longer of the length of the input laser pulse, or the resolution of the spectrometer and electronics ( $\sim 2\ \text{ns}$ ). The magnetic field of the MOT is non-uniform and very small (roughly 1 gauss), leading to Zeeman shifts of  $\sim 1\ \text{MHz}$  so can be safely ignored for the purposes of this experiment.

The trapping is done by two CW lasers. In all experiments in this work, part of the excitation is done by a laser that will be referred to as L2. This is a CW laser, chopped by an Acousto-Optical Modulator (AOM), at a wavelength of 1529 nm, tuned slightly to the blue of the atomic  $5p_{3/2} - 4d_{5/2}$  transition.

In order to trap, and to get the maximum benefit from L2, all of these CW lasers must have a fixed, known frequency in relation to the atomic hyperfine structure. This is accomplished in a scheme shown diagrammatically in Fig 3.2. The master laser is locked to the so-called 2-3 crossover peak, which is halfway between the  $5s_{1/2}F = 2 - 5p_{3/2}F' = 3$  and  $5s_{1/2}F = 2 - 5p_{3/2}F' = 2$  lines in Fig 3.3, in the saturated absorption spectrum of a Rb cell using a Zeeman dither locking scheme<sup>35</sup>. This places its frequency  $\sim 133\ \text{MHz}$  to the red of

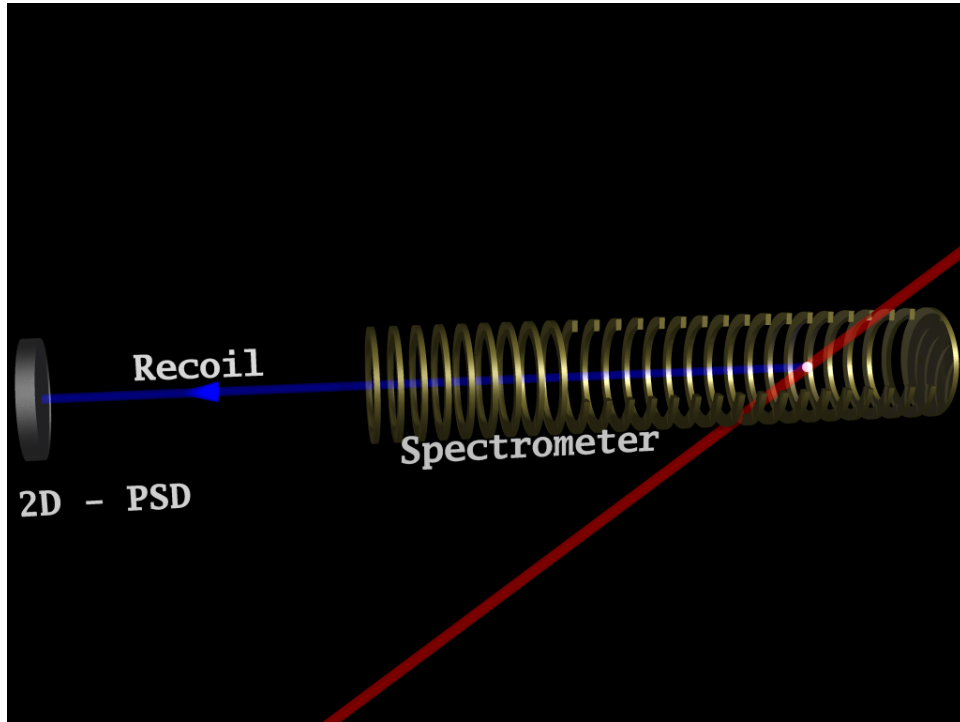


Figure 3.1: The internals of the vacuum chamber. The red beam represents the excitation laser beams. The trap beams have been removed for clarity. Ions are produced in the MOT (white), and extracted by the spectrometer (brass rings, some cut away for clarity) to hit the 2d position sensitive detector (PSD).

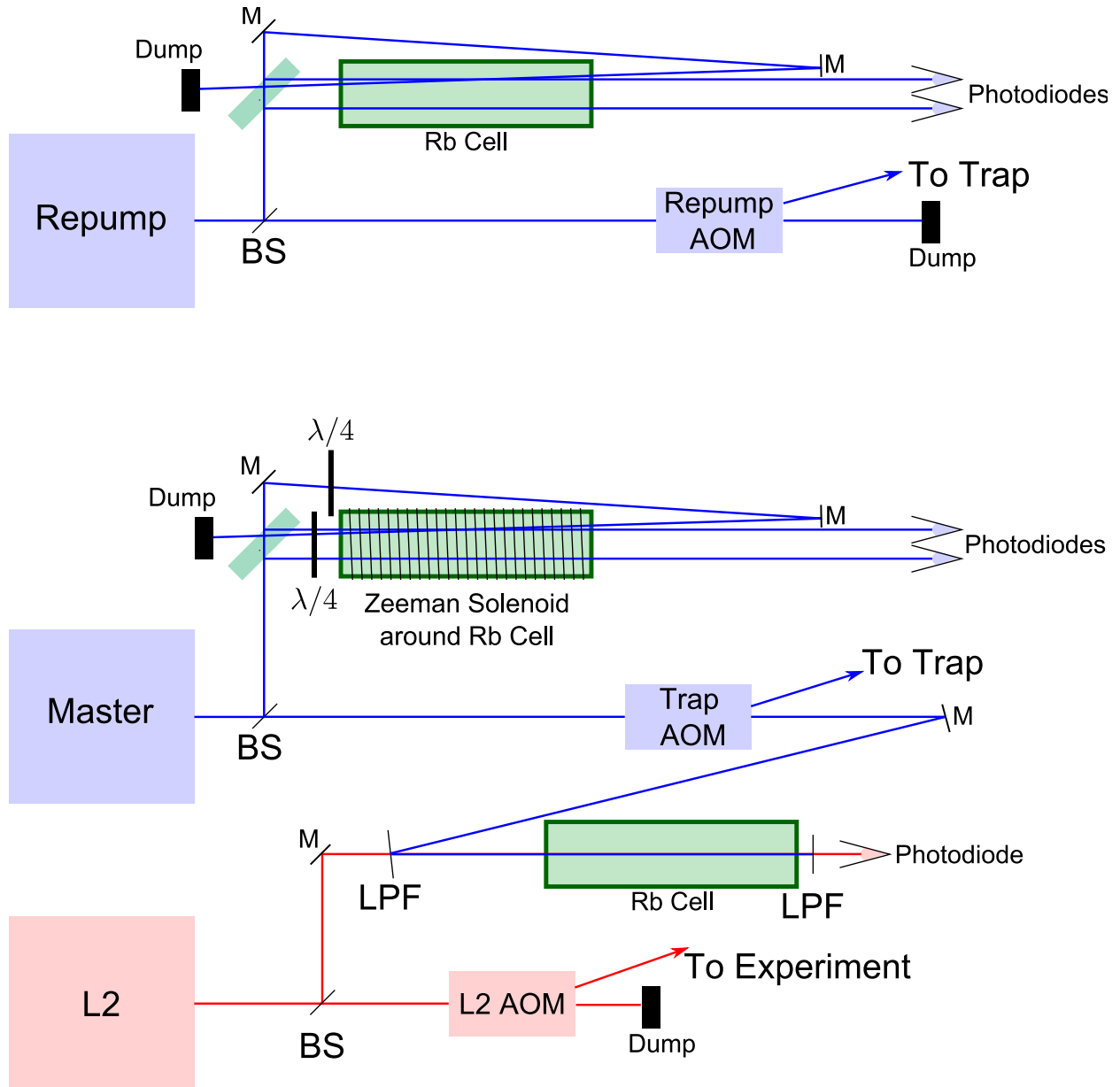


Figure 3.2: Schematic of the basic locking apparatus. M: Mirror; LPF: Long Pass Filter, reflects 780 nm and passes 1529 nm; BS: Beam Splitter;  $\lambda/4$ : quarter wave plate, converts linear polarized light into circular polarized light; AOM: Acoustico-Optical Modulator

the  $5s_{1/2}F = 2 - 5p_{3/2}F' = 3$  trapping transition. An AOM is used to shift the frequency upward by  $\sim 115$  MHz to bring the final trap frequency to within a few linewidths of the trapping transition for optimal trapping.

To lock L2 the zero order diffraction from the trapping AOM (the zero order diffraction from an AOM has the same frequency as the incident laser) is sent to a second cell where it excites atoms having a particular thermal velocity. L2 light is then sent through this

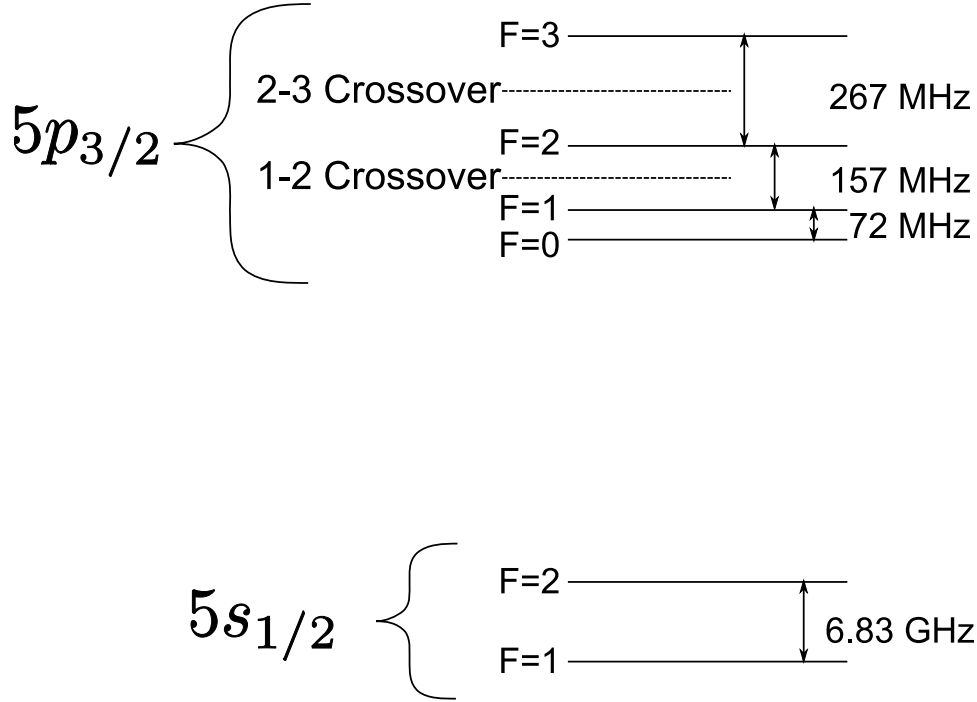


Figure 3.3: Rubidium hyperfine structure showing where the crossovers are located. The crossovers are shown as dashed lines and are a consequence of saturated absorption spectroscopy. The energy axis is not to scale.

cell collinear with the master laser. Because of the wavelength dependent frequency shift of the Doppler effect, absorption of L2 is then at a maximum when L2 is detuned to the red of atomic resonance by  $133 \text{ MHz} \times 780 \text{ nm}/1529 \text{ nm}$ . While the hyperfine structure in the  $4d_{5/2}$  level is not very well resolved, the largest absorption peak comes from the  $5p_{3/2}F = 3 - 4d_{5/2}F' = 4$  state, and this is what L2 is locked to. The L2 light is then passed through an AOM to increase its frequency by  $\sim 120 \text{ MHz}$  to place the final detuning of L2 at  $\sim 50 \text{ MHz}$  to the blue of atomic resonance.

The repump laser is locked independently of the other lasers. It is locked to the so-called 1-2 crossover peak, halfway between the  $5s_{1/2}F = 2 - 5p_{3/2}F' = 3$  and  $5s_{1/2}F = 2 - 5p_{3/2}F' = 2$  lines in Fig 3.3, placing it  $\sim 79 \text{ MHz}$  to the red of the  $5s_{1/2}F = 1 - 5p_{3/2}F' = 2$  repump transition. An AOM is used to increase the frequency by  $80 \text{ MHz}$  to place it within a fraction of a linewidth of atomic resonance.

It is worth noting that each of the lasers mentioned so far is passing through an AOM before reaching the MOT. This is useful, not only to shift frequencies with ease and confidence, but, perhaps more importantly, to allow the lasers to be chopped on and off on nanosecond time scales.

For most of the experimental results, the trap and repump lasers are “turned off” by the AOMs for a time between hundreds of nanoseconds and a few microseconds before the excitation lasers are pulsed. This assures that none of the excitation from the ground state is done by the trap and repump lasers.

Data are collected in event mode, recording, for each ion detected, parameters such as time of flight, position of the ion hit on the detector, and any parameters that are being changed in a particular experiment.

## 3.2 CW PADI-PAI

For the first series of experiments, all excitation is done by AOM-pulsed CW lasers. The goal of the first experiment is to determine the number of photons required for PAI in Rb, using 780 nm and 1529 nm light. The setup for this experiment is shown diagrammatically in Fig 3.4. Two excitation lasers are used, overlapped using a long pass filter, and are collinear with each other going into the MOT. One laser, as already discussed, is L2, while the other is dubbed L1. The L1 light is produced by inserting an AOM between the trap AOM and the Rb cell for the L2 lock. This AOM shifts the L1 frequency to the blue of the master frequency by 80 MHz, thereby putting it  $\sim 53$  MHz to the red of atomic resonance. The zero order diffraction output, which is not frequency shifted, of this AOM is sent to a separate Rb cell for locking L2. L1 and L2 AOM controllers each have a voltage staircase generator connected to their amplitude control inputs. These produce intensities at the MOT that step through 16 different discrete values for each laser. A sample of the output of the staircase generator, only one of which is used at a time, is sent to an Analog to Digital Converter (ADC) which is read by the data acquisition system.

The lasers are pulsed asynchronously with respect to the staircase generator, with a period of  $7.2 \mu\text{s}$  controlled by a separate computer board called (for historical reasons) the “Johnny Box”. This board, a DIO-64 from Viewpoint Systems, produces TTL pulses of a user controllable width and is a key component in controlling the various lasers. For as many ion hits as possible, the data acquisition system measures the time of flight (TOF), ion position on the detector, and the voltage of the staircase generators. For this experiment, the time of flight of each ion is measured starting with its hit on the detector, and stopping with the arrival of the next laser pulse, and is measured with a Time to Digital Converter (TDC)<sup>(1)</sup>. A typical spectrum is shown in Fig 3.5. Note that since the TDC is started with the ion hit, and stopped with the next laser pulse, the TOF spectrum has its time axis reversed, has an arbitrary offset, and is a measure of the time of flight *modulo* the time between laser pulses, thus, the ratio of the displayed TOF for the  $\text{Rb}^+$  and the  $\text{Rb}_2^+$  is not the expected  $\sqrt{2}$ . In a separate, trivial measurement, it was verified that the ratio of the true TOFs is indeed the expected  $\sqrt{2}$ . Since the system can only cope with full data for up to  $\sim 1000$  events per second, while the raw count rate at the detector (almost all of them relevant hits) can reach 30 kHz, another technique has to be used to compensate for this deadtime. The chosen method, shown in Fig 3.4, is to sort, in hardware, the laser pulses according to time of flight, and send the pulses to different channels of a scaler according to the type of ion they correspond to ( $\text{Rb}^+$  or  $\text{Rb}_2^+$ ), these pulses are also sent to other channels of the TDC for diagnostic purposes, including helping to set the gates that sort the pulses.

---

<sup>(1)</sup>LeCroy 4208

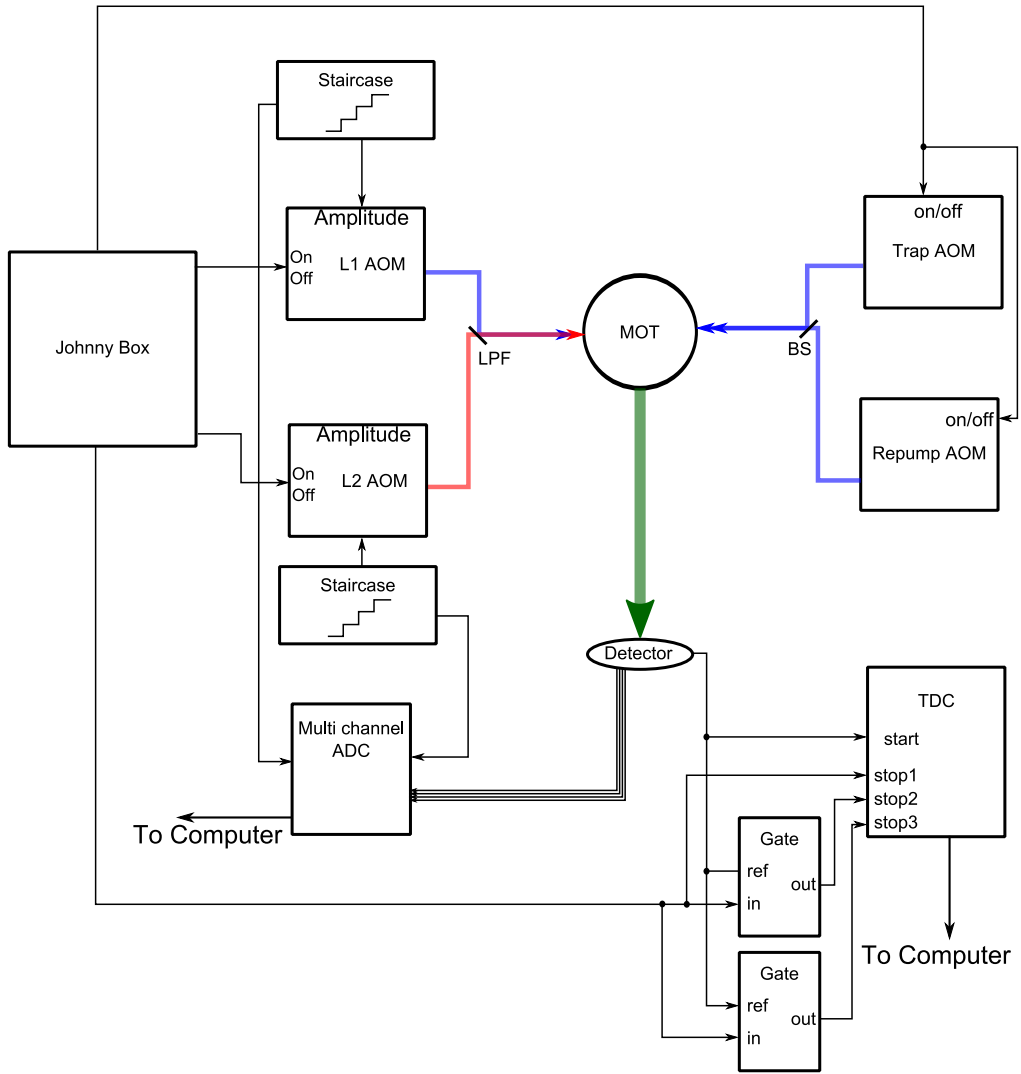


Figure 3.4: Schematic of the CW PADI/PAI experimental setup. The blue and red colored lines correspond to laser light, while the green colored line indicates the ions produced in the MOT. BS: Beam splitter; LPF: Long Pass Filter, reflects L1 while passing L2

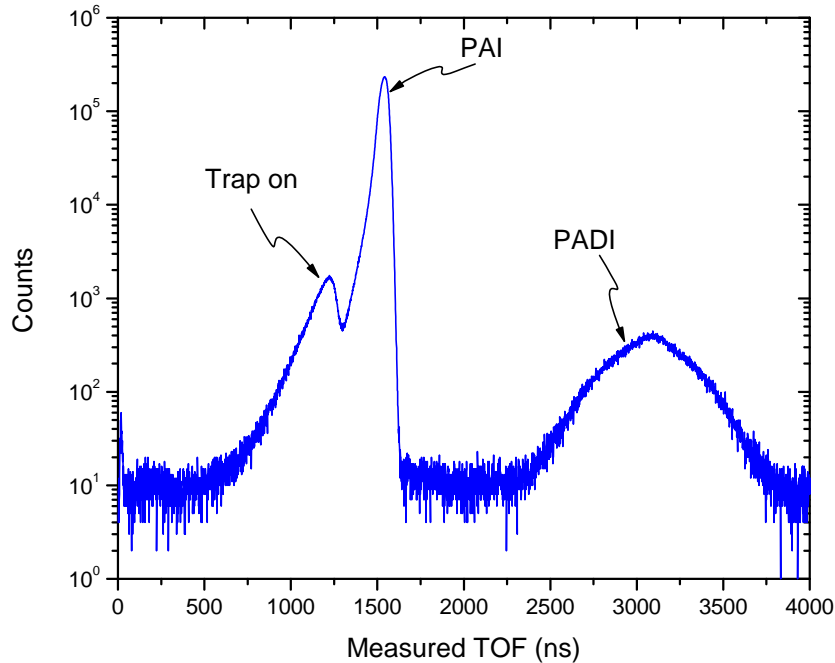


Figure 3.5: A sample TOF spectrum from the CW experiments. Since the time of flight measurements start with the ion hit on the detector and stop with the arrival of the next laser pulse, the time of flight scale is reversed, there is an offset, and the TOF is measured modulo  $7.2 \mu\text{s}$ . The leftmost peak shows that more  $\text{Rb}_2^+$  ions are produced when the trap laser turns back on. This will be discussed in Chapter 4.

At the beginning of each step, the scaler is read and cleared. In this way the number of missed counts is minimized, while the number of events with full data are maximized.

For this experiment, the trap and repump lasers were turned off  $\sim 200$  ns before the excitation lasers were turned on and left off for between 200 ns and  $1 \mu\text{s}$  after the excitation lasers are turned off.

### 3.3 KLS

For the experiments involving the ultrafast laser called the Kansas Light Source (KLS), excitation is done with the KLS and L2 only. It is necessary to be able to synchronize L2, the trap, and the repump signals to the  $\sim 1$  kHz repetition rate of the KLS laser. To do this, a circuit, a delay gate generator, was designed and built to produce the signals (TTL) to control the AOMs and to feed the data acquisition system the appropriate pulses (NIM) for timing. This particular delay gate generator is called the main delay gate generator. More details on this circuit can be found in appendix C.



The data acquisition electronics are significantly more complicated than is the case with the CW lasers, as shown in Fig 3.6. A NIM level pulse from the main delay gate generator constitutes the start of a *potential* event. (Most laser shots do *not* produce an ion, and are therefore not considered events). The arrival of an appropriate ion at the detector constitutes the end of the event, and the proof that there was an event. The multi-channel ADC, which measures (at least) the position of the ion on the detector, is strobed by a delay gate generator triggered by the timing signal corresponding to the arrival of an ion at the detector. This timing signal is also sent to the TDC as a stop signal. Because most signals are unwanted  $\text{Rb}^+$  signals, it is necessary to gate these out. To this end, a gate is generated that is a NIM false for the range of times after the arrival of a pulse from the KLS in which a  $\text{Rb}_2^+$  ion can reasonably fall, but is otherwise a NIM true. This signal is used to inhibit the delay gate generator that strobes the ADC and is also used as a veto input to the TDC. Both of these signals are needed to prevent unwanted counts from registering with the data acquisition system. At the end of this gate (which *must* be less than  $80 \mu\text{s}$ ), a pulse is sent to the TDC as an End Of Window pulse, to signal the end of the event. In addition, since the TDC is started with *every* KLS shot, a signal must be generated to clear the TDC in the event that no ion was detected. This signal is generated nearly one full KLS period after the arrival of the KLS pulse, in order to give the data acquisition system as much time as possible to complete its transactions with the CAMAC crate when there is an event.

In some experiments with the KLS the goal is to identify the wavelengths that are important to the PAI process, and thereby facilitate understanding of the process itself. Other experiments with the KLS are intended to demonstrate control of the PAI process. In all of these experiments with the KLS, it is desirable, or necessary, to shape the pulse in phase and/or amplitude in the frequency domain. To do this, a device called an acousto-optical programmable dispersive filter (AOPDF) is used. This device, which goes by the commercial name “Dazzler”<sup>37,38</sup>, is composed of an arbitrary waveform RF generator, transparent  $\text{TeO}_2$  crystal and a piezoelectric transducer (to generate RF acoustic waves in the crystal). It is based primarily on two effects: birefringence, or a difference in the speed of propagation for two different polarizations of light through a crystal; and the coupling of an acoustic wave with an electromagnetic wave, which it uses to selectively rotate the polarization of light.

The simplest way to think about the operation of the Dazzler is that it works independently with each frequency component. To control the amplitude of a frequency component, it rotates the polarization of that component; for the output magnitude to be zero, it would not rotate at all, while to get the maximum output magnitude it would rotate by 90 degrees. Because of the birefringence of the crystal, the component of the polarization that is perpendicular to the input polarization is sent to the experiment while the rest of the light is dumped. To control the phase of a frequency component, the Dazzler controls the distance the light travels in the crystal after rotation. Since the speed of light of the two polarizations are different, the frequency component will accumulate a phase shift that depends on the distance traveled after rotation. The main limitation of the Dazzler comes from the finite length of the crystal. The length of the crystal limits the maximum group delay that can be put on any frequency component. In other words, it places an upper limit on  $\partial\phi/\partial\omega$ .

The KLS itself is a large facility and will only be described briefly, mentioning the parts

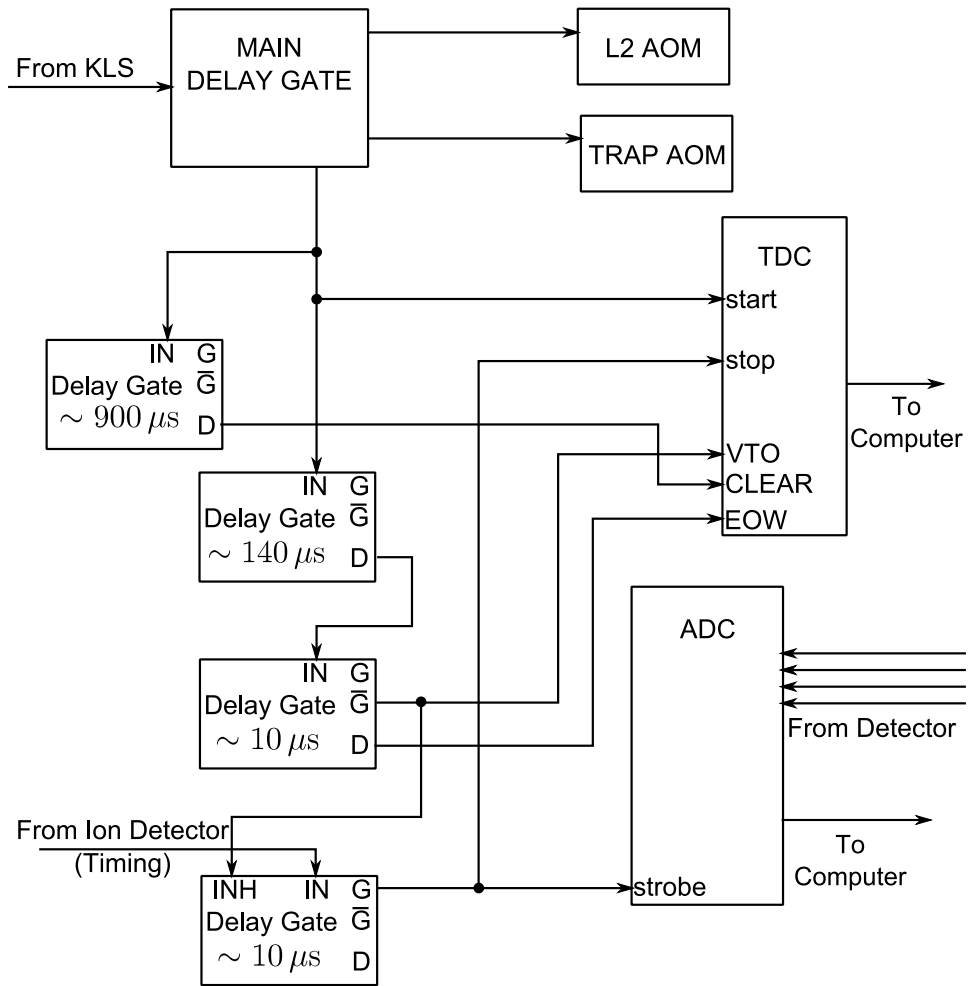


Figure 3.6: Basic electronics setup for the KLS experiments.

that are of importance to this work. The ultrafast, wide-bandwidth pulses are generated in the oscillator<sup>(2)</sup>, which has a repetition rate of  $\sim 80$  MHz. These pulses each have an energy on the nanojoule scale. Since experiments typically need pulse energies on the scale of a millijoule, the pulses must be amplified. Pulses to be amplified are picked out of the oscillator pulse train, at a rate of  $\sim 1$  kHz by a Pockels cell. The pulses are then normally sent to a grating stretcher, which adds a large positive second order phase term to the pulses in order to stretch them temporally from  $\sim 20$  fs to  $\sim 80$  ps; they are then amplified in a multi-pass amplifier to  $\sim 1 - 2$  mJ. A grating compressor is used to remove the large second order phase term, caused by both the stretcher and the amplifier, from the pulse before the pulse is sent on. The pulse then goes through a  $\sim 10$  m evacuated transport line to the experiment. Since the transport line is very long, it is often the case that the beam can wander, since a small angular deviation of the beam at the laser produces a large displacement of the beam at the experiment. To help combat this, a circuit can be used to stabilize the position and pointing of the beam at the experiment. This circuit, and the accompanying optics, is called the Automatic Laser Pointing Stabilizer (ALPS) and is detailed in appendix C.

The Dazzler AO crystal is inserted into the optical path between the stretcher and the amplifier as shown in Fig 3.7. While it is possible to run with no other modifications, working in this way uses much of the length of the Dazzler crystal to compensate for the dispersion of the crystal itself. This is unacceptable in many experiments. To compensate, the grating pulse compressor can be adjusted to remove most of the second order phase term added by the Dazzler crystal.

While the Dazzler was calibrated upon installation, some time after a software update, it was discovered that the calibration was no longer valid. The calibration procedure is rather simple: the light after the Dazzler is directed into a spectrometer; a notch is introduced into the spectral amplitude and the position of the notch in the measured spectrum is compared to the intended position of the notch. The calibration can be easily changed by altering a variable in a configuration file.

The Dazzler is controlled by a LabVIEW program on a Windows laptop to which it is connected via USB. Since the data acquisition is done on a Linux machine in another room, a method was developed to patch the two systems together in order to control the Dazzler from the Linux based data acquisition computer via the Windows based laptop. This is discussed in further detail in appendix D. For now, it suffices to point out that this was done, and that the data packet for each event contains information about the state of the Dazzler. The system steps sequentially through a number of Dazzler configurations, up to several hundred in these experiments, in a round-robin order, at regular intervals (typically dwelling on each configuration for 15 s) asynchronously with respect to anything else in the experiment. This allows for an averaging out of any long term, slow variations in experimental parameters that are not sufficiently controlled, to do individual runs with sufficient statistics for each configuration. It also allows for a much more automated experiment, reducing the stress on the experimenters during beam-times.

---

<sup>(2)</sup>Femtolasers Femtosource Pro

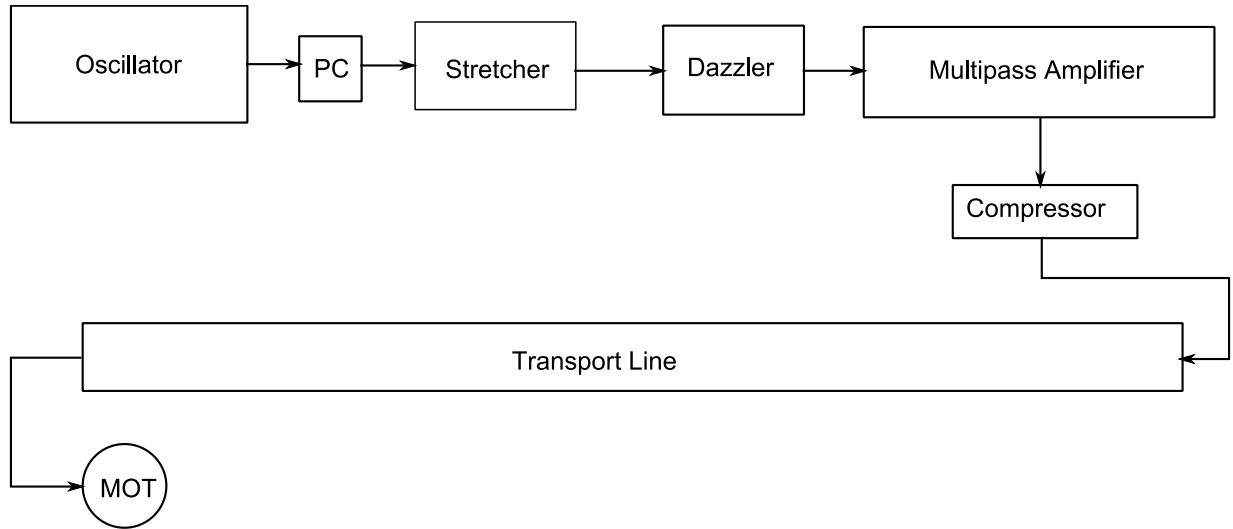


Figure 3.7: Simplified schematic of the KLS and Dazzler setup. PC refers to a Pockels cell

In one experiment, which does not use the Dazzler, the goal was to determine the excitation pathway for the combination of ultrafast and CW lasers that resulted in PAI. To this end, the electronics were changed to allow a variable delay between a  $\sim 50$  ns pulse from L2 and the ultrafast pulse from KLS with nanosecond precision. A circuit was constructed to allow asynchronous stepping of the delay in 5 ns steps. Details on this circuit are in appendix C. The time difference between the KLS pulse and the L2 pulse is then measured by the TDC. In order to allow the TDC to respond to the L2 pulse, it was necessary to reorganize the veto gate. This is accomplished by simply changing it from a gate that is true except for when a molecular ion would hit, to a gate that is false except when an atomic ion would hit (and for a large margin on either side of that time).

# Chapter 4

## Results

### 4.1 CW PADI-PAI

The first of the CW experiments is designed to determine the number of photons used in the PADI and PAI processes in Rb with light at 780 nm and 1529 nm. This is mostly a sanity check, to show that nothing unexpected is happening. For a process requiring  $n$  photons of the same color, the count rate will, neglecting saturation, vary with the intensity of that color light,  $I$ , like  $I^n$ . To determine the number of photons, then, is the simple matter of determining the scaling of the count rate with intensity. To do this, the intensity of L1 and L2 were stepped through 16 values each, and the count rate was measured for each intensity. To prevent unknown variables from influencing the results, all values of intensity for a given laser are taken in the same run, cycling through many times, to average out variations in other parameters.

Plots of the total number of counts in a given run, as a function of intensity are given in Fig 4.1. It is relatively obvious that, even at these low powers, saturation cannot be neglected. A more sophisticated model is found by solving the rate equations representing a system of  $n + 1$  levels for the highest excited state's population fraction  $f_{n+1}$  in terms of the intensity,  $I$ , and coupling constants<sup>(1)</sup>  $k_{ij}$  and  $\gamma_{ij}$  at steady state. For  $n = 1$ , that is a two level system,

$$f_2 = \frac{k_{01}I}{2k_{01}I + \gamma_{01}}. \quad (4.1)$$

For  $n = 2$ , a three level ladder system with the two transitions resonant with the same color photon,

$$f_3 = \frac{k_{01}I^2}{3k_{01}I^2 + \left(2\frac{k_{01}}{k_{12}}\gamma_{12} + \gamma_{01}\right)I + \frac{\gamma_{12}\gamma_{01}}{k_{12}}}. \quad (4.2)$$

A quick examination of Eqs 4.1 and 4.2 reveals that a number of parameters are not necessary for the fit. In both equations, one can *define*  $k_{01} = 1$ . In Eq 4.2,  $\gamma_{12}$  and  $k_{12}$

---

<sup>(1)</sup> $\gamma_{ij}$  is the decay rate, and  $k_{ij}$  is related to the transition strength, which is itself related to the decay rate. They are essentially the Einstein A and B parameters, respectively, for the transitions.

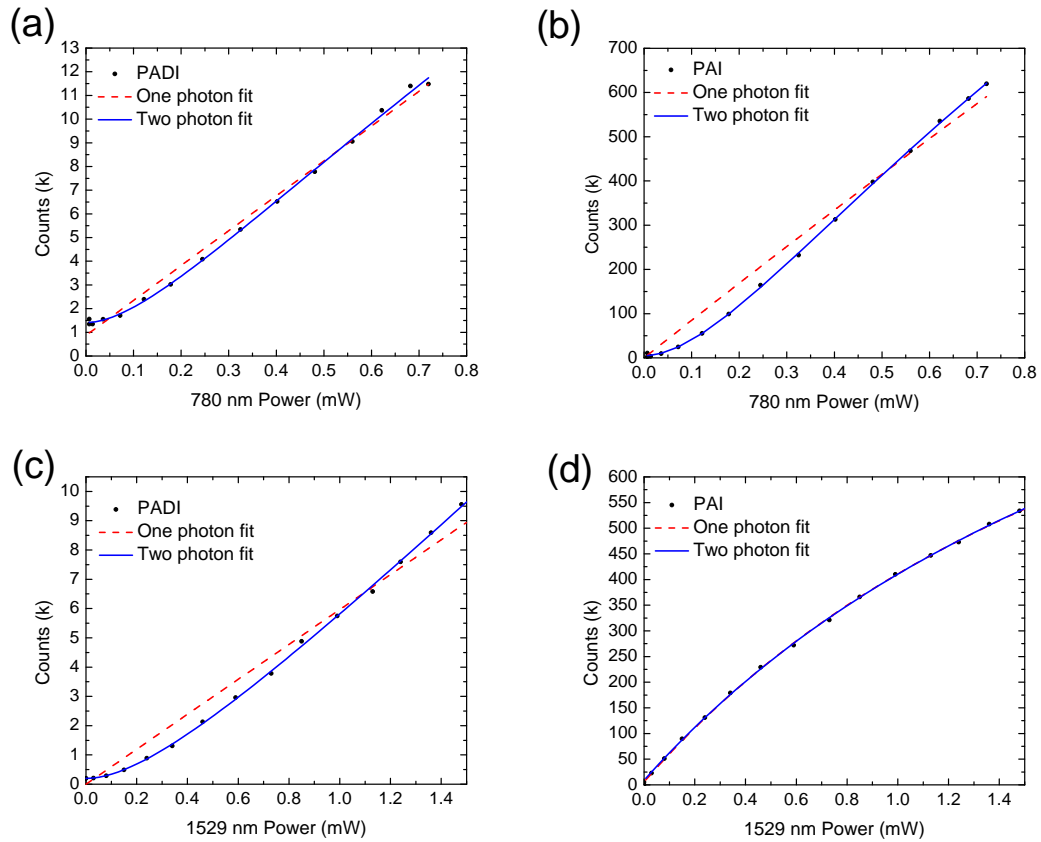


Figure 4.1: Count rate as a function of L1 and L2 powers. (a) PADI vs L1, (b) PAI vs L1, (c) PADI vs L2, (d) PAI vs L2. The dashed red lines are fits to one photon rate equations. The solid blue lines are fits to two photon rate equations.

are not found by themselves, but only the ratio of the two matters. The fraction of the population in the highest excited state is not what is measured, but a rate is, so a scaling factor must be added. In experiment, there is always background, so a term must be added to accommodate this. The resultant equations that are fit to the data are given by

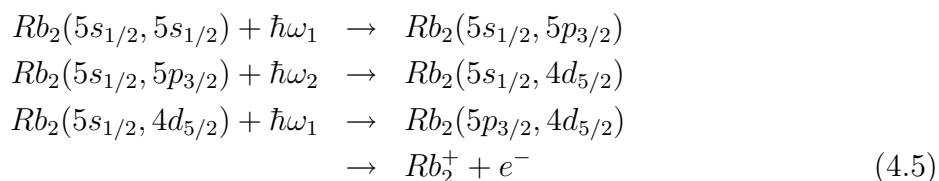
$$R = C_1 \frac{I}{2I + B_1} + G_1 \quad (4.3)$$

for the one photon case and

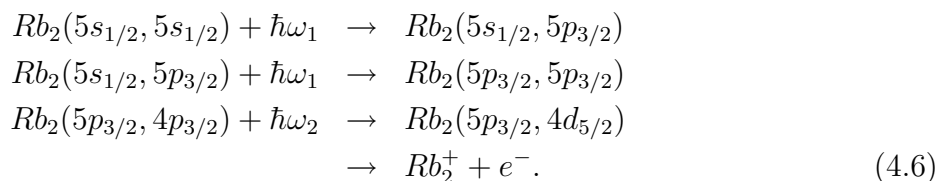
$$R = C_2 \frac{I^2}{3I^2 + A_2I + B_2} + G_2 \quad (4.4)$$

for the two photon case. By fitting these equations to the data, the curves in Fig 4.1 are obtained. The red dashed curve is the one photon fit, Eq 4.3, while the blue solid curve is the two photon fit, Eq 4.4. For the plot in part (d) of that figure, the fitting procedure determined that  $B_2 = 0$ . This is the limiting case of a lack of decay in one of the transitions, which collapses a three level system into an effective two level system<sup>(2)</sup>, resulting in identical curves for both models. These plots, therefore, clearly show that PADI requires two 1529 nm photons and two 780 nm photons while PAI requires two 780 nm photons and only one 1529 nm photons.

The order in which photons are absorbed in PAI, along with the detunings used, determines the excitation pathway, that is, which manifolds of molecular states corresponding to which asymptotic atomic energy levels are involved in the process. There are two possibilities:



and



Here,  $\hbar\omega_1$  and  $\hbar\omega_2$  refer to photons from L1 and L2, respectively. The narrow linewidth lasers in use in these experiments precludes interaction with the  $5p_{1/2}$  states which are several

---

<sup>(2)</sup>When there is no spontaneous emission, a vanishingly small amount of resonant laser light is enough to completely saturate the transition. In a steady state situation, this means that the two levels have the same population regardless of intensity, so the transition doesn't count toward the number of photons needed.

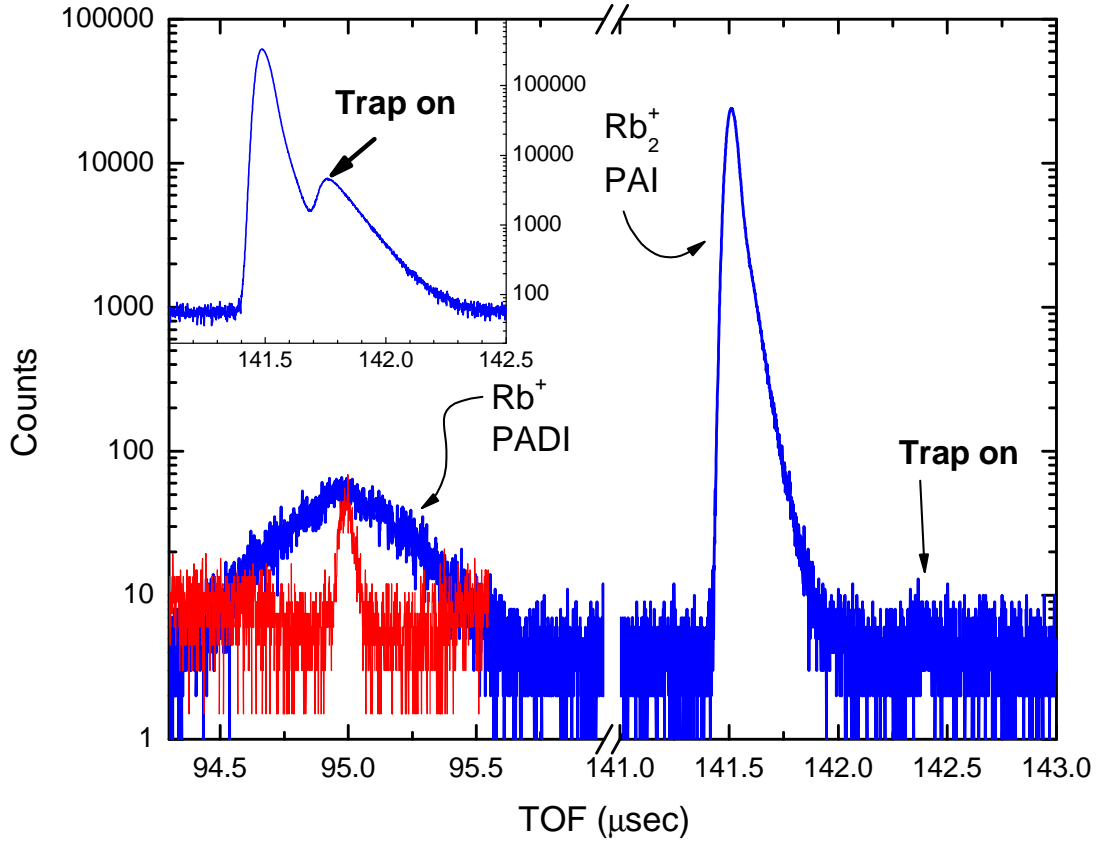


Figure 4.2: TOF spectra. The inset contains data from a different (longer) experiment that shows what the  $Rb_2$  peak looks like when L1 and L2 are pulsed simultaneously and 300 ns later, the trap is turned on, showing that the population moves through the relatively long-lived states near the  $5s+4d$  asymptote. The longer lifetime on this second peak is because the trap is left on. A close examination of the main part of the figure shows a hint of a second peak  $1 \mu s$  after the main peak, when the trap turns back on. For comparison, a photoionization peak, obtained without L2, is shown in red.

nanometers away from resonance. Equation 4.5 is referred to as the L1-L2-L1 process while Eq 4.6 is referred to as the L1-L1-L2 process. Even without doing the experiment, there would be reason to believe that the process follows the L1-L2-L1 path. The reason is that the  $Rb_2(5p_{3/2}, 5p_{3/2})$  levels in the L1-L1-L2 path are very flat at large internuclear separations. Since the lasers are detuned many linewidths from resonance, these levels are far outside the bandwidth of the lasers. While compelling, this reason is far from conclusive.

The key to determining the photon order for PAI can be seen in the TOF plot in Fig 4.2. The trap laser is turned off  $\sim 200$  ns before L1 and L2 are pulsed. The main part of the



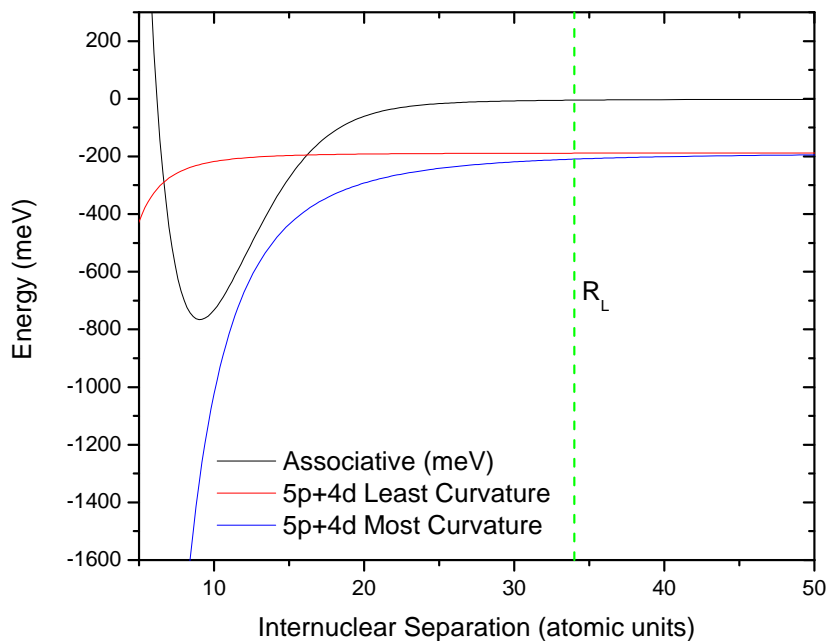


Figure 4.3: Plotted PAI potential curves. Only the most and least bound  $5p + 4d$  states are plotted. Inside the vertical green line, the LeRoy radius, the accuracy of the curves should not be relied on, as the approximation used in calculation is not valid.

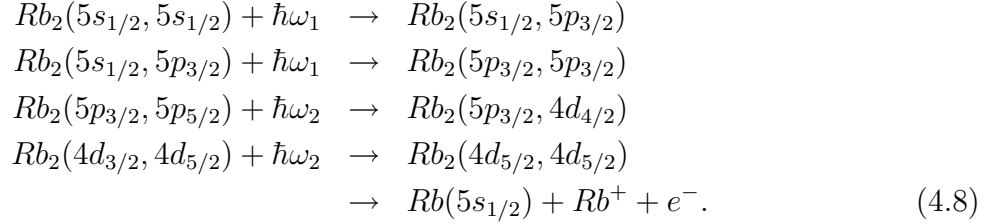
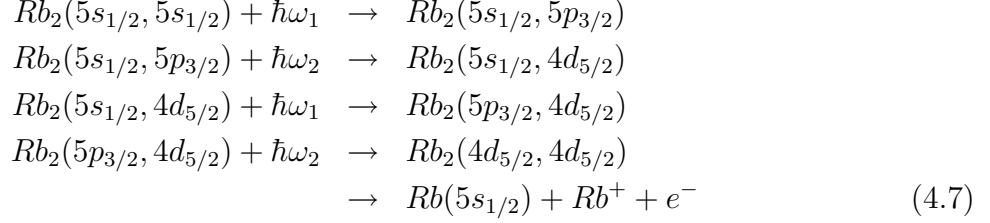
figure shows a TOF spectrum in the case that the trap is turned on a full microsecond after L1 and L2 are pulsed. The inset shows the PAI peak when the trap is turned on 300 ns after L1 and L2 are pulsed. The PAI peak in the inset has two peaks, like in Fig 3.5. This second peak appears when the trap laser is turned back on. Since there is no L2 in the system at this point in time, the molecules must be in a state that can reach the molecular ion *without* L2. The only process that has such a state is the L1-L2-L1 process. A quick study of the size of this peak as a function of the delay between L1/L2 and the trap turning back on suggests a decay with a lifetime similar to the lifetime of the atomic  $4d$  state ( $\sim 90$  ns). This is further evidence in support of the L1-L2-L1 excitation pathway. This second peak can be used to isolate the second L1 transition for study such as CW spectroscopy.

The exponential tail on the PAI peak results from the radiative decay of the  $5p + 4d$  state and has a lifetime near the atomic  $5p$  lifetime.

Looking at potential energy curves, supplied by Monique Frécon's group in Lyon<sup>39,40</sup> plotted in Fig 4.3, shows that, to the limit of the accuracy of the curves, the autoionization at the end of the PAI process happens within about 15 au. For the most deeply bound potential curves, there is a possibility that there would not be a curve crossing, and that such curves would not contribute to the PAI rate. It should be noted that the colored curves, corresponding to the neutral  $\text{Rb}_2$  molecule are approximate. Inside the LeRoy radius,

indicated as  $R_L$  in the figure, the approximation used in calculating the curves breaks down. The accuracy of these curves near the autoionization point, then is questionable.

For PADI, there are two excitation pathways:



The former possibility (L1-L2-L1-L2) is considered most likely since it is very similar to the CW PAI pathway, however, since the final photon in both cases is an L2 photon, the technique applied to PAI cannot be applied to PADI. It is unclear how to conclusively determine the photon order.

Even more data can be gleaned from the TOF spectrum. While the PAI peak's width is dominated by a decay lifetime and the  $\sim 50$  ns pulse width, the PADI peak has significant width, especially compared to a photoionization peak obtained without L2 (shown in red in Fig 4.2). Since the ionization is performed in a momentum spectrometer, it is possible to turn this width into a distribution of the kinetic energies of the  $Rb^+$  ions produced. The relationship between the time of flight spectrum,  $C_t(t)$ , and the energy spectrum,  $C_E(E)$ , derived in appendix B, is given by

$$C_E(E) = \left| \frac{dC_t(t)}{dt} \right| \frac{1}{2A} \tag{4.9}$$

where  $E = A(t-t_0)^2$  and  $A$  is a constant determined by the mass of the ion and the spectrometer geometry and voltage; for the spectrometer used and  $^{87}Rb$ ,  $A = 3.75 \times 10^{-5}$  meV/ns<sup>2</sup> as determined by SIMION simulations. From conservation of momentum, the Kinetic Energy Release (KER) is simply twice the energy of the  $Rb^+$  fragment. A plot of the KER spectrum is shown in Fig 4.4. The two red lines in the spectrum correspond to the rising and falling edge of the TOF peak. Ideally, these curves should lie on top of each other, however the differences are within the uncertainty in KER. The blue dashed lines indicated that the half-max of the distribution occurs at  $\sim 13.5$  meV, or  $\sim 6.75$  meV for the ion kinetic energy. This energy is roughly 3 orders of magnitude larger than could be expected for photoionization of an isolated atom, proving that the process is indeed PADI.

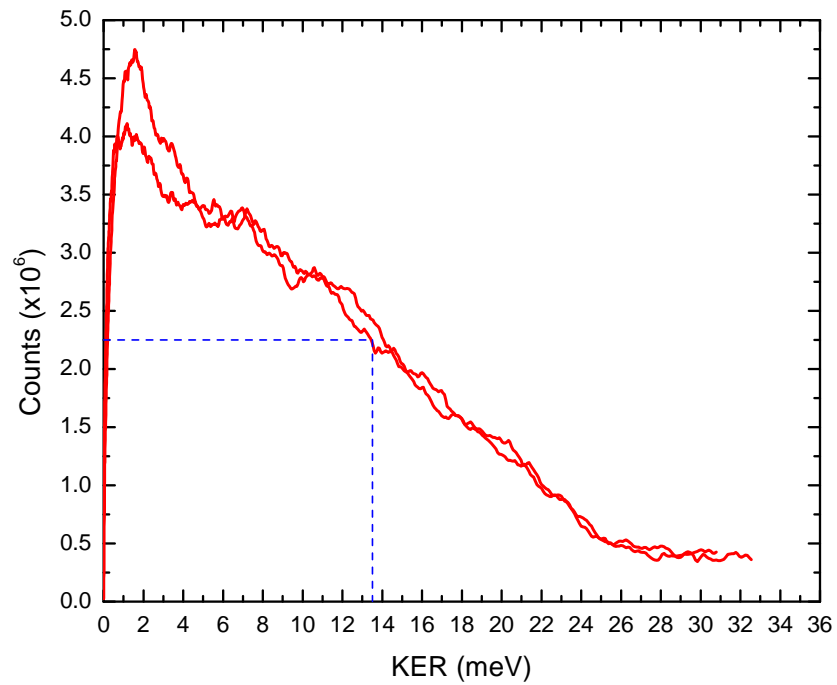


Figure 4.4: The distribution of the kinetic energy release (KER) of the PADI process. What looks like two traces is a result of the conversion from time of flight to energy giving distributions from both rising and falling edges of the time of flight peak. The dip near zero KER is likely an artifact of the resolution of the measurement and smoothing.

A large source of uncertainty in the energies from Eq 4.9 comes from an uncertainty in the value of  $t_0$ . The uncertainty from this source is discussed in appendix B and is shown to have a value of less than 2 meV in KER at the half max of the energy distribution.

To learn more from this energy distribution, it is necessary to examine the potential curves for the 4d+4d states and the  $\text{Rb}_2^+$  states. Some of the relevant curves<sup>39,40</sup>, are plotted in Fig 4.5(a). For simplicity, only the most and least bound of the 30 4d+4d curves (not counting spin-orbit coupling) are plotted. The vertical green line at 40 au is at the LeRoy radius, the internuclear separation inside of which, the approximations used in the calculation of the curves are no longer valid. The curves in Fig 4.5(b) are a plot of the sum of the energies labeled “Energy<sub>1</sub>” and “Energy<sub>2</sub>” in part (a) of the figure, as a function of internuclear separation for each of the two 4d+4d curves. When this energy is negative its absolute value is the binding energy. When the energy is positive it is the KER. When a curve in Fig 4.5(b) is below zero, autoionization from the corresponding state would result in a bound molecule, i.e. an electronically excited  $\text{Rb}_2^+$ . The blue horizontal line is at 14 meV, corresponding to the half max of the observed energy distribution. The curves cross the blue line between 20 and 25 atomic units of internuclear separation. Since this is well within the LeRoy radius, there are unknown error bars on these numbers due to the limited accuracy of the calculation.

Outside of 20 to 30 atomic units, the curves in Fig 4.5(b) are below zero. This implies that if autoionization takes place at internuclear separations larger than this, the resulting ion will be a bound  $\text{Rb}_2^+$  in the  $\Omega_g = 3/2$  state. Since the ground state also has gerade symmetry, the excited state is metastable and the molecules produced through this mechanism will remain in the excited state until they decay via a dipole forbidden transition. The contribution of these molecules to the overall PAI rate is small at low intensities, as evidenced by the measurements of photon number for the PAI process.

## 4.2 KLS results

The focus of some of the KLS experiments is much the same as the CW experiments already described: to determine the excitation pathway for the PAI process, including the asymptotic atomic transitions involved, and the order of photon absorption. To this end, a number of experiments were conducted. To determine the asymptotic atomic transitions that play an important role, the Dazzler was used to remove wavelengths from the spectrum of the pulse. The order of photon absorption was determined by using an L2 pulse that was delayed with respect to the KLS pulse. More wavelength information, intended to help solidify understanding of the molecular levels and internuclear separations involved is obtained by shaping the phase of the KLS pulse in the frequency domain.

Other experiments are intended as demonstrations that the PAI system with KLS and 1529 nm CW light is controllable in the sense of using simple spectral phase shapes to greatly modify the production rate of  $\text{Rb}_2^+$ . Two phase profiles are used in these demonstrations, a sinusoidal phase and a simple chirp. Both of these are favorites of the coherent control community.

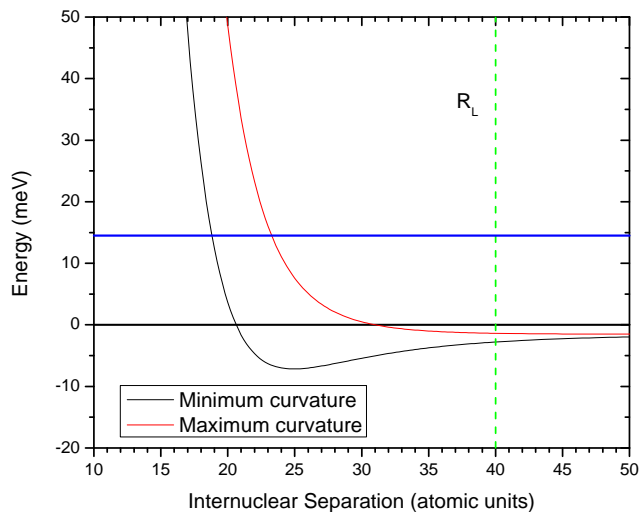
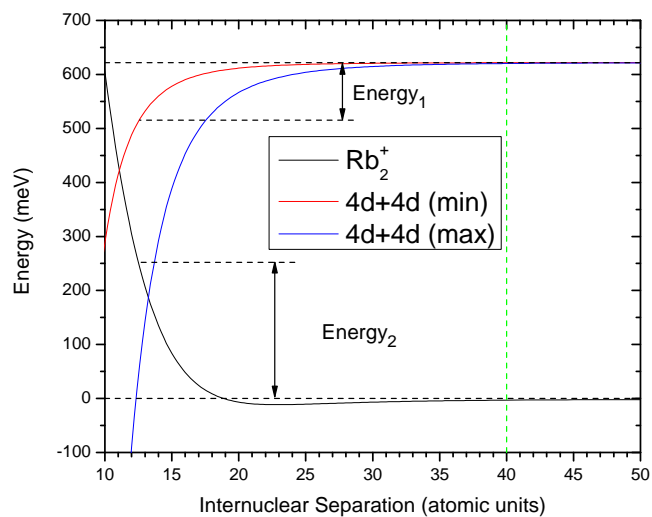


Figure 4.5: Plots of relevant potential curves for PADI (a). From the bound  $4d+4d$  curves, only the ones with the most and least curvature are plotted. Panel (b) is a plot of the sum of the energies marked “ $\text{Energy}_1$ ” and “ $\text{Energy}_2$ ” in (a). When the energy is negative, it is the additive inverse of the binding energy. When the energy is positive it is the KER. The vertical line at 40 au is the LeRoy radius, inside of which the approximation in the calculations of the curves breaks down.

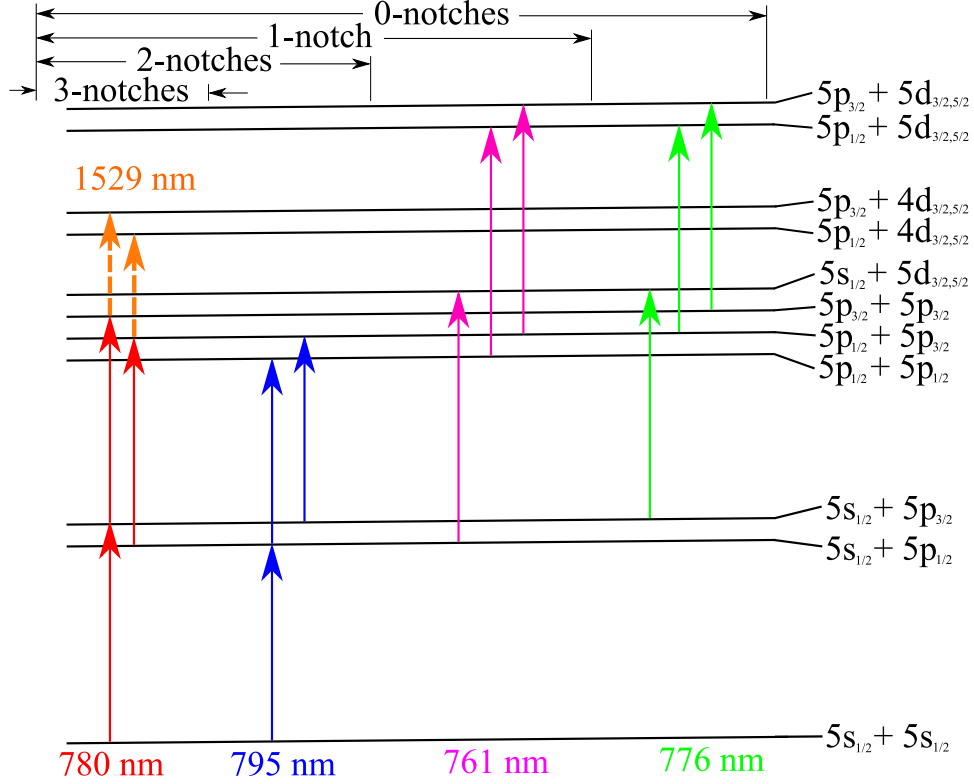


Figure 4.6: Schematic (not to scale) of the molecular energy levels relevant to the excitation pathways discussed in the text. The “notches” labels indicate which wavelengths are available under the different notch conditions. For example, in the “2-notches” case, 780 nm and 795 nm wavelengths are available, while 761 nm and 776 nm are not in the ultrafast pulse. L2’s 1529 nm radiation, indicated by dashes, was available during all notch configurations. Figure and caption taken from Veshapidze *et al.*<sup>41</sup>.

### 4.2.1 Spectral amplitude

The Dazzler supports easy removal of spectral components from an ultrafast pulse. Four configurations were used to help determine the asymptotic atomic transitions involved in our ultrafast PAI process. These configurations, named for the number of notches, or holes, placed in the spectrum, are shown in Fig 4.6. Each notch was 3 nm wide FWHM, centered on the indicated atomic transition wavelength. So, for example, in the “2-notches” case, 780 nm and 795 nm wavelengths are available, while 761 nm and 776 nm are not in the pulse. The trap is turned off several microseconds before the KLS is pulsed, and turned back on several microseconds after the KLS is pulsed. For nearly the entire time that the trap is off, L2 is on, with just enough room on either side to ensure that L2 and trap will not combine to produce molecular ions. The main reason for the long times is to relax the requirements on the main delay gate generator.

For each configuration, a count rate measurement was made for both atomic and molecular Rb. It was determined that all of the configurations resulted in nearly the same  $\text{Rb}_2^+$

count rate, while the  $\text{Rb}^+$  count rate varied by nearly two orders of magnitude. These results indicate that the  $5p_{1/2}$  and  $5d$  atomic states do not have an appreciative effect on the PAI rate.

### 4.2.2 L2 delay

Much like in CW PAI, there are two possibilities for the photon absorption order. Either the photons can be absorbed in a KLS-L2-KLS order, or in a KLS-KLS-L2 order. The latter case seems the more likely, since the very low fluence of L2 during the duration of the KLS pulse would have very little chance of exciting the molecule in time for the molecule to absorb another KLS photon. To get a more definitive answer to the question of photon order, the following experiment was performed. A short,  $\sim 50$  ns, pulse of L2 is stepped through the KLS pulse in time. In the case that L2 precedes KLS, no excitation should occur because L2 is not resonant with any transitions from the ground state of Rb. In the case that L2 and KLS overlap, there should be maximal excitation. In the case that L2 trails KLS, though, excitation will only occur if the photon order is KLS-KLS-L2. Also, if this is the photon order, a TOF spectrum, started with the KLS pulse will show the peaks shifting in time as trailing edge of the L2 pulse comes later and later after the KLS pulse.

Figure 4.7 summarizes the results of this experiment. The color contour plot shows the time of flight spectrum as a function of delay between KLS and L2; the white line connects the peaks of the TOF spectrum for each delay value. The right portion of the spectrum shows the number of  $\text{Rb}_2^+$  counts as a function of the delay between KLS and L2. The figure shows that, for delays greater than  $\sim 12$  ns, the TOF peak moves to longer times in the same manner as the trailing edge of the L2 pulse. The count rate is also more tolerant of a positive delay between KLS and L2, meaning that the KLS precedes L2. All of this supports the KLS-KLS-L2 model of excitation.

### 4.2.3 Phase based spectroscopy

A quick look at the theory in section 2.4 will reveal that there is a  $\pi$  phase shift in the response of the system as a function of frequency near the resonance. Putting a  $\pi$  phase shift at this resonance will compensate for the natural phase shift, giving a larger excitation rate. This can be exploited by looking at the count rate as a function of position of this shift. Resonances will appear as troughs or peaks in such a spectrum. As a first step, a phase profile given by

$$\phi(\omega) = \frac{\pi}{2}(1 - \text{erf}[2(\lambda_1 - \lambda)]) \approx \begin{cases} \pi & \lambda < \lambda_1 \\ 0 & \lambda_1 < \lambda \end{cases} \quad (4.10)$$

is used. This profile, plotted in Fig 4.8 for  $\lambda_1 = 760$  nm, is called a “pi edge” for obvious reasons. It has a finite rise, going from  $\pi/10$  to  $9\pi/10$  in roughly 0.9 nm. A plot of the TOF spectrum, with an offset of  $\sim 152$   $\mu\text{s}$ , as a function of  $\lambda_1$  is given in Fig 4.9(a). There are several things worth noting in this figure: the TOF peaks change position depending

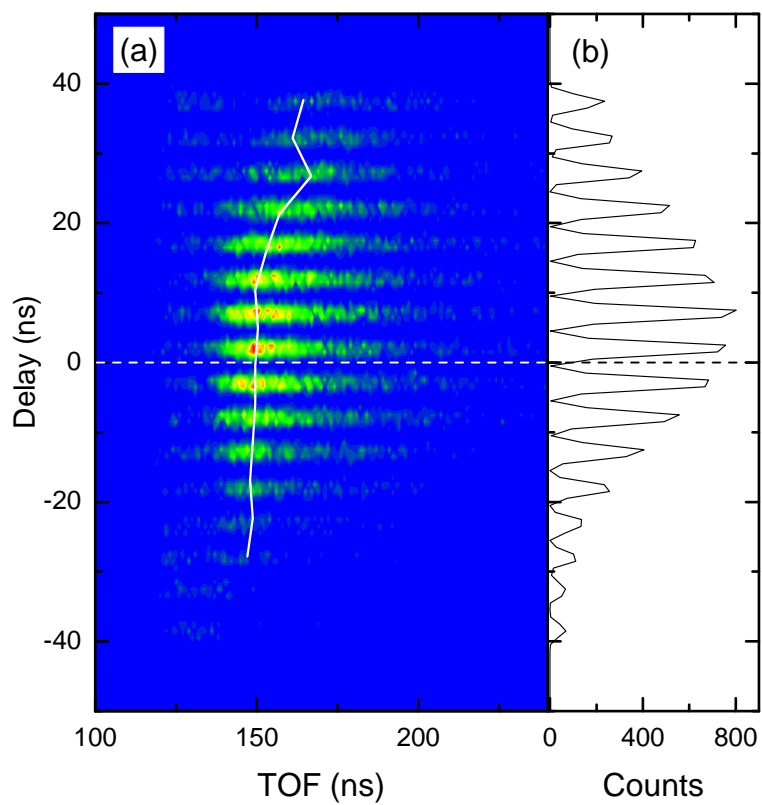


Figure 4.7: (a) Density plot of  $\text{Rb}_2^+$  TOF spectra as a function of the delay between the KLS and L2 pulses. Negative delay means L2 preceded KLS. (b) Horizontal projection of (a). Figure and caption taken from Veshapidze *et al.*<sup>41</sup>.



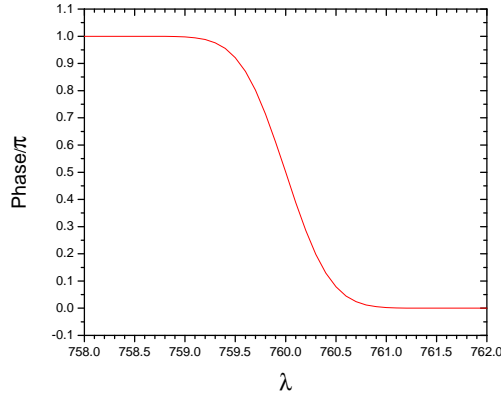


Figure 4.8: A sample pi edge phase profile. This profile is for the case of  $\lambda_1 = 760.0$  nm. The fall from  $9\pi/10$  to  $\pi/10$  takes  $\sim 1$  nm and the profile is actually an error function.

on the value of  $\lambda_1$ ; the width of the TOF peaks also change with  $\lambda_1$ ; and the total count rates change. Figure 4.9(b) shows the same spectrum, but normalized such that the number of counts in the TOF channel with the largest number of counts for each  $\lambda_1$  is constant. This normalization helps to emphasize the shapes and positions of the peaks, and how they change with  $\lambda_1$ . The TOF peak positions and widths seem to take on a few discrete values; this is taken as evidence that these different widths and positions correspond to different states. The positions are related to the incubation time as discussed in section 2.2, which is a product of the combination of internuclear separation and the curvature of the states, most likely dominated by the curvature of the  $5p + 4d$  states. The width is also likely a product of the curvature of the  $5p + 4d$  states and the initial width of the wave-packet by the time it reaches the  $5p + 4d$  states. Figure 4.10(a) shows the number of counts *versus*  $\lambda_1$ . By gating on only short TOF in Fig 4.9, say from 0 ns to 150 ns the spectrum of count rate *versus*  $\lambda_1$  in Fig 4.10(b) is obtained. Conversely, by gating on only long TOF, from 380 ns to 600 ns, the spectrum in Fig 4.10(c) is revealed.

Since the spectrum in Fig 4.10(c) has the fewest sharp features, it is assumed that this spectrum involves the fewest states and should therefore agree with a few level theory best. Qualitative agreement with the Dudovich model from section 2.4, namely Eq 2.6, can be easily achieved with the four level system shown in Fig 4.11(a). The positions of the two intermediate states were adjusted manually to fit the data. While the contributions from the two intermediate levels are summed coherently, there is not much difference in the spectrum when the summing is incoherent. The results of this calculation are shown in Fig 4.11(b). With this theoretical model, any resonance halfway between the lowest state and the highest state reached by the ultrafast pulse will have no effect on the spectrum. This insensitivity to a symmetric system, where the upper and lower transitions have the same wavelength, can be relied upon to enhance the appearance of any other, asymmetric transitions. While the qualitative agreement is *very* good, the unpredicted large contrast

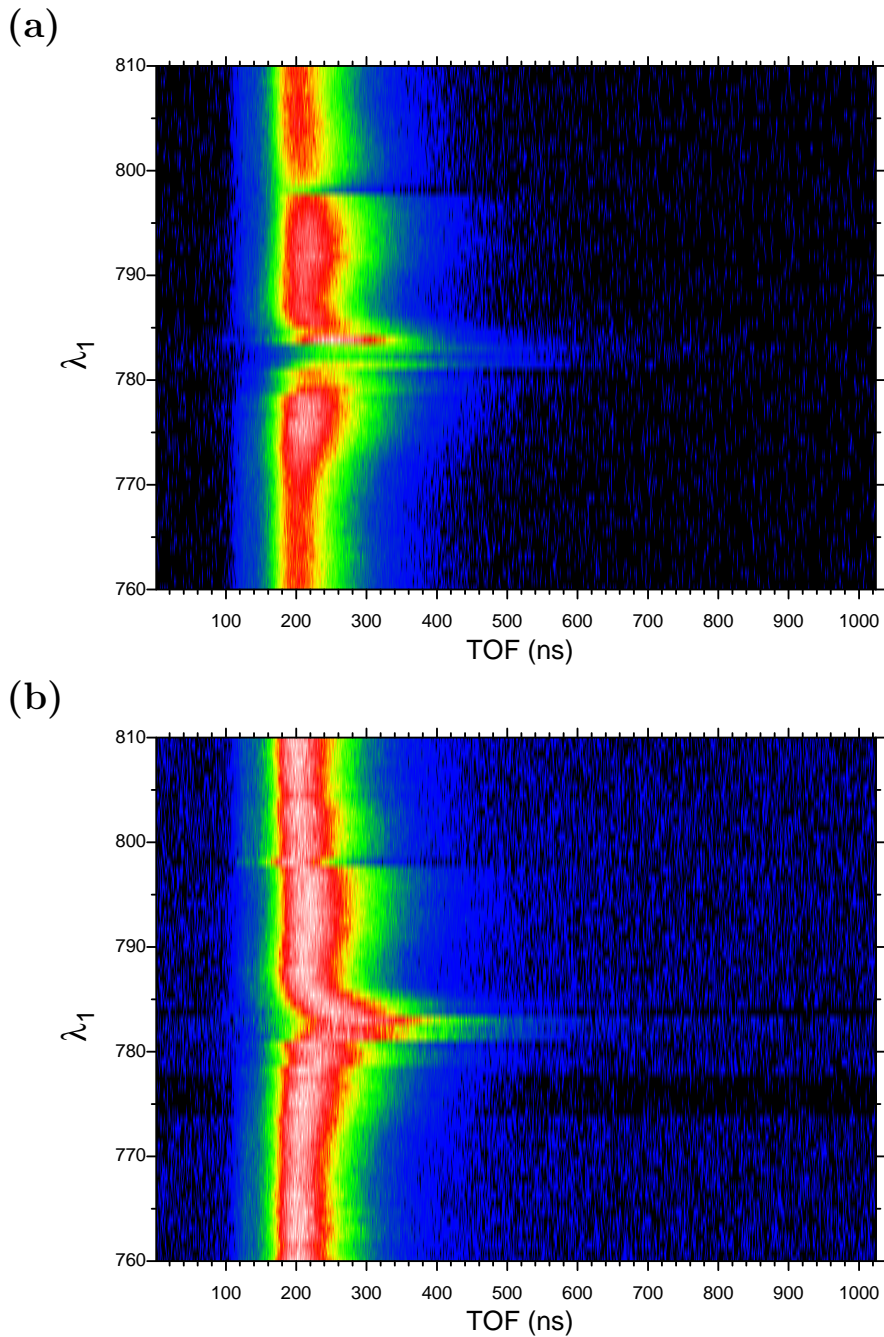


Figure 4.9: TOF spectrum *versus* pi edge wavelength. The different TOFs for different wavelengths of the pi edge is attributed to final molecular states in the  $5p + 4d$  manifold, resulting in different incubation times. The  $\lambda_1$  axis is uncalibrated. Panel (b) is the same as (a) but normalized so that the peak for each position of the pi edge has the same number of counts. This is done to improve the visibility of the shapes and locations of the TOF peaks.

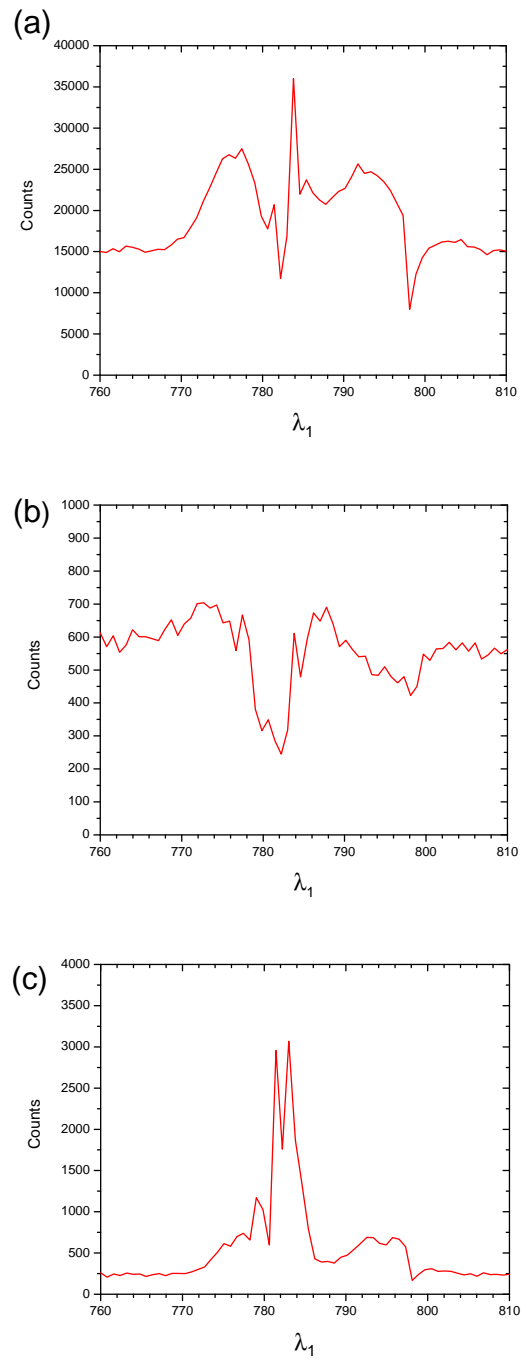


Figure 4.10: Counts *versus*  $\lambda_1$  (uncalibrated) for a pi-edge. a) All counts in the PAI peak. b) Gated on TOF from 0 to 150 ns. c) Gated on TOF from 380 ns to 600 ns.

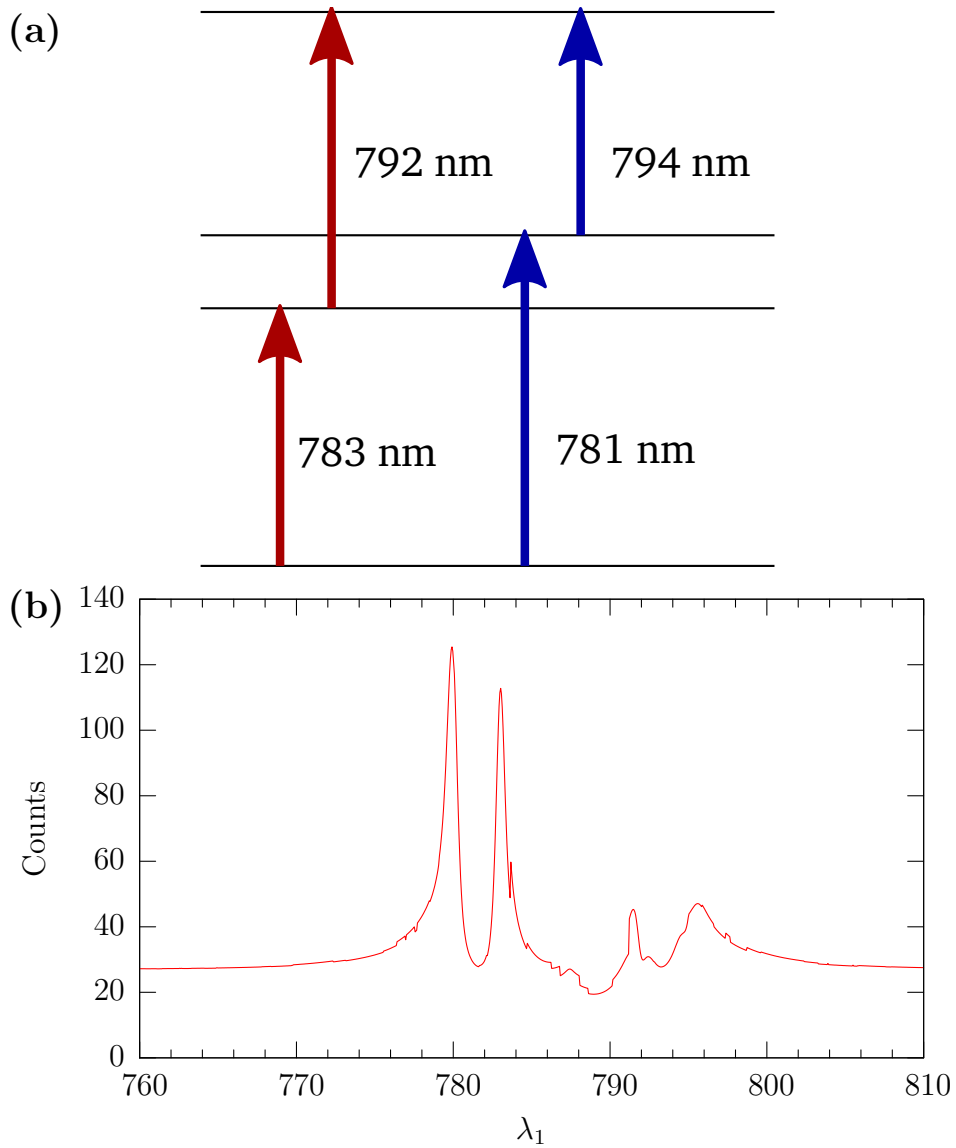


Figure 4.11: Energy level diagram (a), and the theoretical counts *versus* pi edge calculated for that system. Equation 2.6 from Dudovich was used as the model. While the major features match Fig 4.10(c), there are unexplained differences.

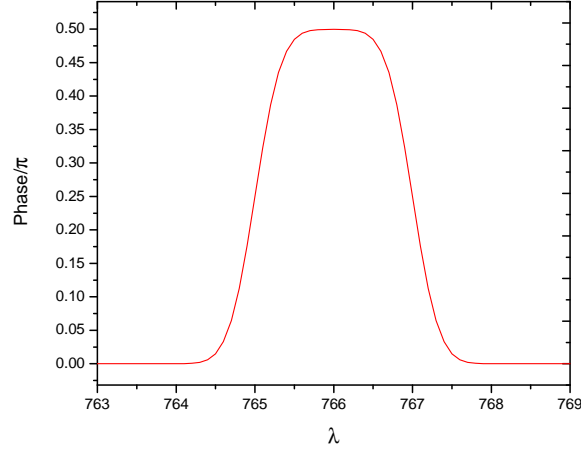


Figure 4.12: A sample  $\pi/2$  step phase profile. In this example,  $\lambda_1 = 760$  nm and  $\lambda_2 = 762$  nm. The rise and fall are similar to the pi edge case, which is partly by design, and partly due to the limitations of the Dazzler.

shown in the experiment is not well understood. Certainly, a more sophisticated model, including more states, and a better representation of the short pulse, would be more likely to provide quantitative agreement. Still, this experiment reveals what it was intended to reveal, namely the wavelengths that are important in the PAI process.

While the pi edge provides good contrast for some transitions and reveals a number of features, the contrast for the upper transitions is not as good. For example, while the level diagram in Fig 4.11(a) shows that the lower transitions have wavelengths of 792 nm and 794 nm, this is not as readily apparent from the spectrum. The wavelengths of the upper transitions do not show up very well in the pi edge system, either in theory or experiment. Dudovich *et al.*<sup>29</sup> provide a solution to this problem. By using a phase profile that looks like

$$\phi(\omega) = \begin{cases} \frac{\pi}{4}(1 - \text{erf}[2(\lambda_1 - \lambda)]) & \lambda < (\lambda_1 + \lambda_2)/2 \\ \frac{\pi}{4}(1 - \text{erf}[2(\lambda - \lambda_2)]) & (\lambda_1 + \lambda_2)/2 < \lambda \end{cases} \approx \begin{cases} 0 & \omega < 2\pi c/\lambda_1 \\ \frac{\pi}{2} & 2\pi c/\lambda_1 < \omega < 2\pi c/\lambda_2 \\ 0 & 2\pi c/\lambda_2 < \omega \end{cases} \quad (4.11)$$

which is plotted in Fig 4.12 for  $\lambda_1 = 760$  nm and  $\lambda_2 = 762$  nm, the upper and lower transitions are distinguished. The upper transitions show up as peaks in the count rate *versus*  $\lambda_1$  and the lower transition shows up as a peak in the count rate *versus*  $\lambda_2$ . Figure 2.4 shows a sample calculation to illustrate this. In that calculation, the lower transition has a wavelength of 780 nm and the upper transition has a wavelength of 776 nm. The  $\pi/2$  phase shift at resonance can cause some of the off resonant excitation to interfere constructively with the resonant excitation, giving peaks. If the  $\pi/2$  phase shift occurs at both the upper

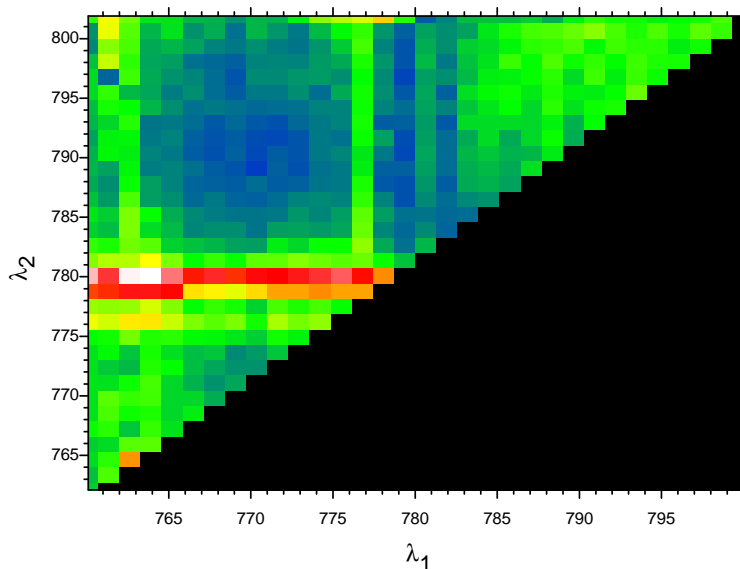


Figure 4.13: Atomic ion counts *versus*  $\pi/2$  edge wavelengths. The strong lines at 780 nm (horizontal) and 776 nm (vertical) are expected. The vertical line at 761 nm, while expected, is unexpectedly strong. The expected horizontal line at 795 nm, which should not be strong, does not show up at all.

and lower transitions, with the proper sign, all of the excitation from all frequencies, resonant and off resonant, interfere constructively, giving a very large peak.

A phase profile of this nature, scanned in two dimensions,  $\lambda_1$  and  $\lambda_2$ , adds a level of complexity to the experiment. As a check, and a learning experience, pulses with this phase profile were used to ionize atomic Rb. A plot of the count rate, gated with a 20 ns wide gate on TOF, is shown in Fig 4.13. The transition wavelengths that are within the bandwidth of the laser are  $5s_{1/2} \rightarrow 5p_{1/2}$  at 795 nm, which is paired with the  $5p_{1/2} \rightarrow 5d$  at 761 nm; and  $5s_{1/2} \rightarrow 5p_{3/2}$  at 780 nm, paired with  $5p_{3/2} \rightarrow 5d$  at 776 nm. Since 761 nm is in the far wings of the bandwidth of the pulse, the lines at 795 nm and 761 nm are not expected to be very strong. The results are very close to what one would expect.

The next step is to do such an experiment with molecules. Figure 4.14(a) shows the TOF spectrum *versus* Dazzler step for such an experiment. Table 4.1 relates the Dazzler step number to the wavelengths of the two edges<sup>(3)</sup>. Again, to get a better idea of the *shape* of the TOF peak for each Dazzler step, the spectrum is normalized to peak height for each Dazzler step. This normalized spectrum is shown in Fig 4.14(b). It is apparent that there are multiple incubation times, and consequently multiple states, represented in this spectrum. Figure 4.15(a) shows the *total* number of PAI counts recorded for each Dazzler

---

<sup>(3)</sup>A separate calibration of the Dazzler indicates that it was miscalibrated by  $\sim 0.5\%$  making the wavelengths quoted in the table, which are uncalibrated, differ from those presented in later figures, which are calibrated. The values in the table *are* consistent with the data in Fig 4.15.

$\lambda_0$	$\lambda_1$	765.0	766.3	767.6	768.9	770.2	771.5	772.7	774.0	775.3	776.6	777.9	779.2	780.5	781.8	783.1	784.4	785.6	786.9	788.2	789.5	790.8	792.1	793.4	794.7	796.0	797.3	798.5	799.8	801.1	802.4	803.7	805.0	
$\nu$	x	0	1	2	3	4	5	6	7	8	9	10	11	12	13	14	15	16	17	18	19	20	21	22	23	24	25	26	27	28	29	30	31	
807.0	31	31	62	92	121	149	176	202	227	251	274	296	317	337	356	374	391	407	422	436	449	461	472	482	491	499	506	512	517	521	524	526	527	
805.7	30	30	61	91	120	148	175	201	226	250	273	295	316	336	355	373	390	406	421	435	448	460	471	481	490	498	505	511	516	520	523	525		
804.4	29	29	60	90	119	147	174	200	225	249	272	294	315	335	354	372	389	405	420	434	447	459	470	480	489	497	504	510	515	519	522			
803.1	28	28	59	89	118	146	173	199	224	248	271	293	314	334	353	371	388	404	419	433	446	458	469	479	488	496	503	509	514	518				
801.8	27	27	58	88	117	145	172	198	223	247	270	292	313	333	352	370	387	403	418	432	445	457	468	478	487	495	502	508	513					
800.5	26	26	57	87	116	144	171	197	222	246	269	291	312	332	351	369	386	402	417	431	444	456	467	477	486	494	501	507						
799.3	25	25	56	86	115	143	170	196	221	245	268	290	311	331	350	368	385	401	416	430	443	455	466	476	485	493	500							
798.0	24	24	55	85	114	142	169	195	220	244	267	289	310	330	349	367	384	400	415	429	442	454	465	475	484	492								
796.7	23	23	54	84	113	141	168	194	219	243	266	288	309	329	348	366	383	399	414	428	441	453	464	474	483									
795.4	22	22	53	83	112	140	167	193	218	242	265	287	308	328	347	365	382	398	413	427	440	452	463	473										
794.1	21	21	52	82	111	139	166	192	217	241	264	286	307	327	346	364	381	397	412	426	439	451	462											
792.8	20	20	51	81	110	138	165	191	216	240	263	285	306	326	345	363	380	396	411	425	438	450												
791.5	19	19	50	80	109	137	164	190	215	239	262	284	305	325	344	362	379	395	410	424	437													
790.2	18	18	49	79	108	136	163	189	214	238	261	283	304	324	343	361	378	394	409	423														
788.9	17	17	48	78	107	135	162	188	213	237	260	282	303	323	342	360	377	393	408															
787.6	16	16	47	77	106	134	161	187	212	236	259	281	302	322	341	359	376	392																
786.4	15	15	46	76	105	133	160	186	211	235	258	280	301	321	340	358	375																	
785.1	14	14	45	75	104	132	159	185	210	234	257	279	300	320	339	357																		
783.8	13	13	44	74	103	131	158	184	209	233	256	278	299	319	338																			
782.5	12	12	43	73	102	130	157	183	208	232	255	277	298	318																				
781.2	11	11	42	72	101	129	156	182	207	231	254	276	297																					
779.9	10	10	41	71	100	128	155	181	206	230	253	275																						
778.6	9	9	40	70	99	127	154	180	205	229	252																							
777.3	8	8	39	69	98	126	153	179	204	228																								
776.0	7	7	38	68	97	125	152	178	203																									
774.7	6	6	37	67	96	124	151	177																										
773.5	5	5	36	66	95	123	150																											
772.2	4	4	35	65	94	122																												
770.9	3	3	34	64	93																													
769.6	2	2	33	63																														
768.3	1	1	32																															
767.0	0	0																																

Table 4.1: Conversion between Dazzler step number for the  $\pi/2$  phase pulse to wavelengths of the two edges.

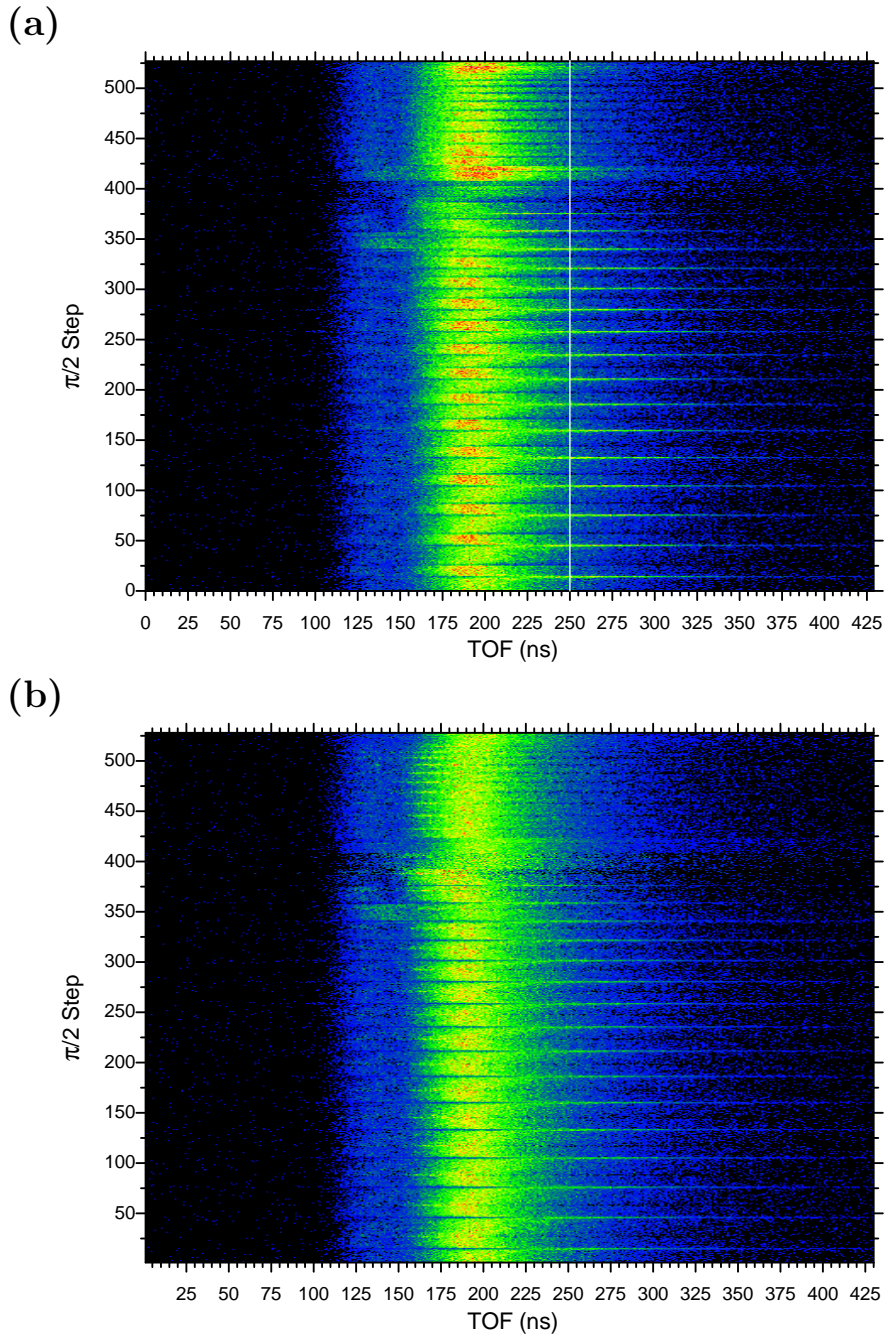


Figure 4.14: TOF spectrum *versus*  $\pi/2$  step number. The conversion from step number to actual  $\lambda_1$  and  $\lambda_2$  is given in Table 4.1. The different TOFs for different step numbers is again attributed to different states in the  $5p + 4d$  manifold, leading to different incubation times. Panel (b) is the same as panel (a) but normalized so that the peak for each step number has the same number of counts. This is again done to improve the visibility of the shapes and locations of the TOF peaks.



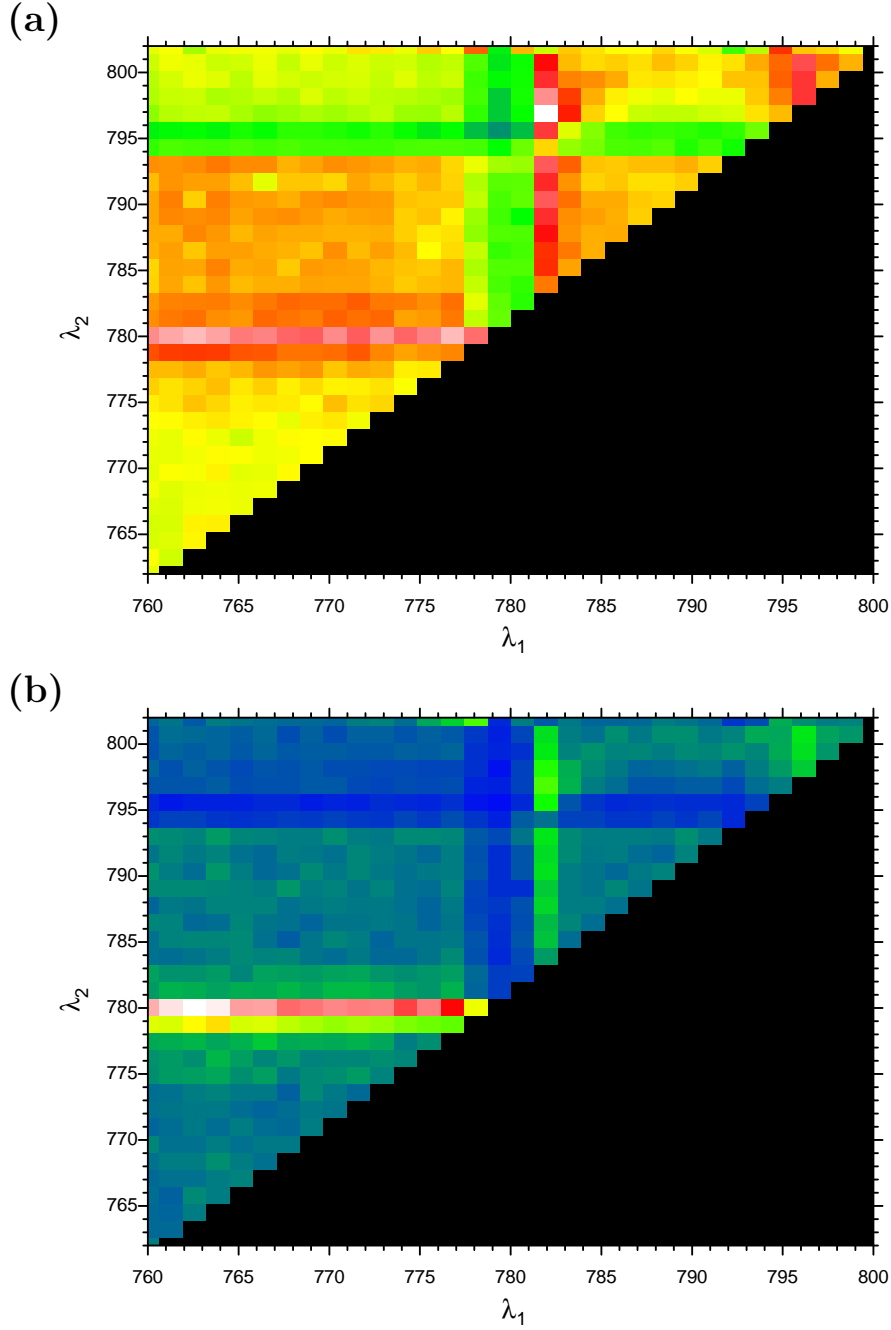


Figure 4.15: Counts *versus*  $\lambda_1$  and  $\lambda_2$  are gated on the entire PAI TOF peak (a) and on the long TOF tails (b). Note that the features in (b) are much clearer. This is attributed to the fewer number of pathways to a single state in the  $5p + 4d$  manifold.

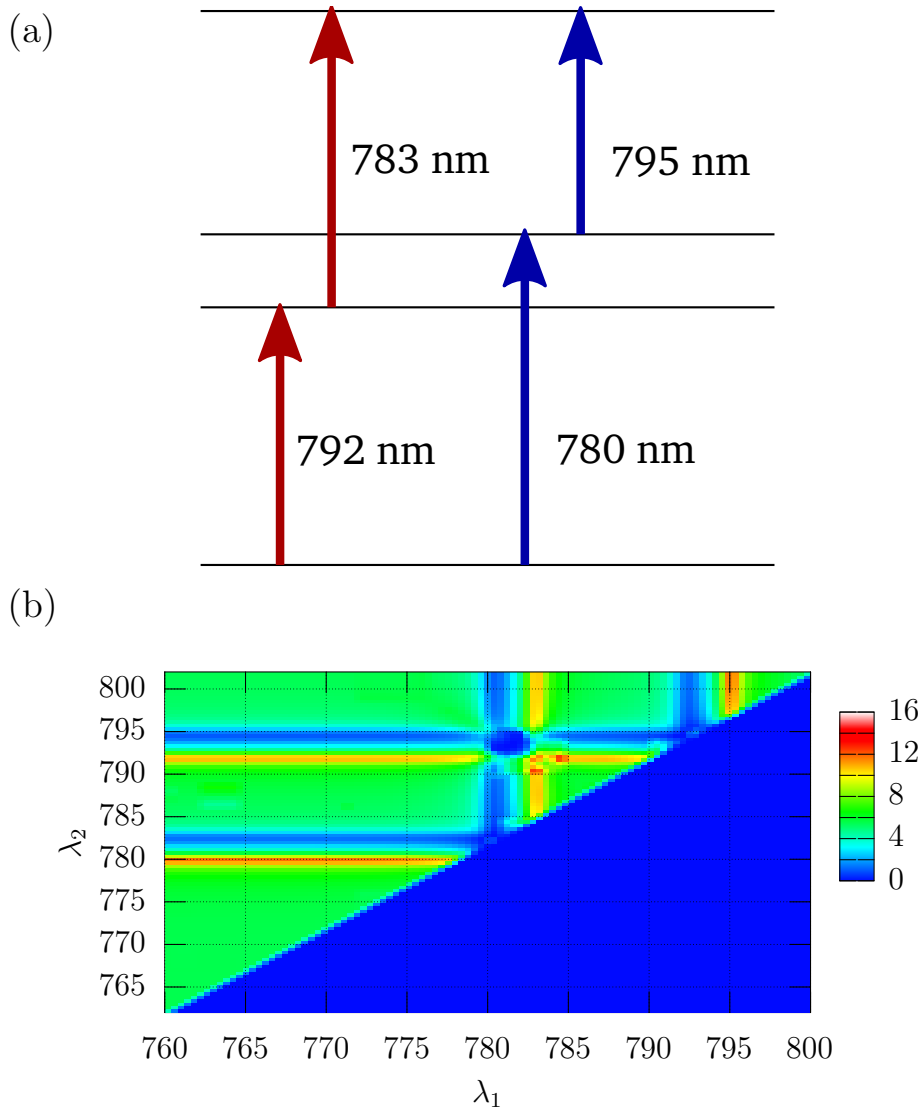


Figure 4.16: Theoretical counts *versus*  $\lambda_1$  and  $\lambda_2$ . The model used is from Dudovich, namely Eq 2.6. It agrees qualitatively very well, and quantitatively to some degree with the data in Fig 4.15(b). The positions of the intermediate states (a) were manually adjusted to fit the data.

step. To select only the long TOF states, the spectrum in Fig 4.15(b) is gated from 250 ns, where the white line is drawn in Fig 4.14, to 400 ns. The gated counts for each Dazzler step are plotted in Fig 4.15(b). A calculation for the system, shown in Fig 4.16(a), matches well with the experiment. A plot of the result of this calculation is shown in Fig 4.16(b). As in the pi-edge case, theory indicates that this test should be insensitive to levels for which the upper and lower transitions are near each other in wavelength.

That the two phase based spectroscopy methods reveal two different pathways, neither of which are the same as the one suggested by the spectral notches result, is disappointing but not surprising. This merely suggests that there are a number of different ways to get from the  $5s + 5s$  ground state to the  $\text{Rb}_2^+$  ion and that different spectral phases favor different excitation pathways. It suggests a richness in the physics involved and should lead to interesting results under future study.

#### 4.2.4 Control

Two phase profiles that are very popular in the coherent control community have been tested on this system. The first is a simple, but very large, second order phase term and the second is a sinusoidal phase given by

$$\phi(\omega) = A \sin(T(\omega - \omega_0) + \phi_0), \quad (4.12)$$

where  $A$ ,  $T$ , and  $\phi_0$  are free parameters that can be used to exert control.

A simple second order phase term is the simplest phase profile to apply to a pulse. Since all transparent materials have dispersion in the region near 800 nm, placing a large amount of glass in the beam path will add a positive second order phase term to the pulse. The limit to the size of the second order phase applied to the pulse is given by the amount of glass that can be used, the number of passes through the glass and the amount of high order dispersion that can be tolerated.

In the system under study, the phase profile is created using the Dazzler and the result is shown in Fig 4.17. Large values for the second order phase produce fast oscillations of a variety of frequencies in the real and imaginary parts of the spectral amplitude, making the integral in the Dudovich theory more difficult. For the case of a pure second order phase, Merkel *et al.*<sup>28</sup> evaluated the second order perturbation theory integrals analytically and derived a closed form expression involving error functions with complex arguments. A simple calculation with two free parameters, namely the energy of the intermediate state and an overall scale, using the formalism from Merkel and shown in Fig 4.17, shows good agreement with the experimental results. The energy difference between the final and initial states does not to have much effect, as the choice of the intermediate level position relative to the midpoint between the levels is what matters. For this calculation, the energy difference between the initial and final state corresponds to twice the atomic  $5s$  to  $5p_{3/2}$  energy, which would mean that a level at the halfway point would be connected to the initial and final states by a wavelength of 780 nm. The fit to the data gives wavelengths for the upper and lower transitions of 780.4 nm and 779.6 nm respectively. Much of the fine scale structure in

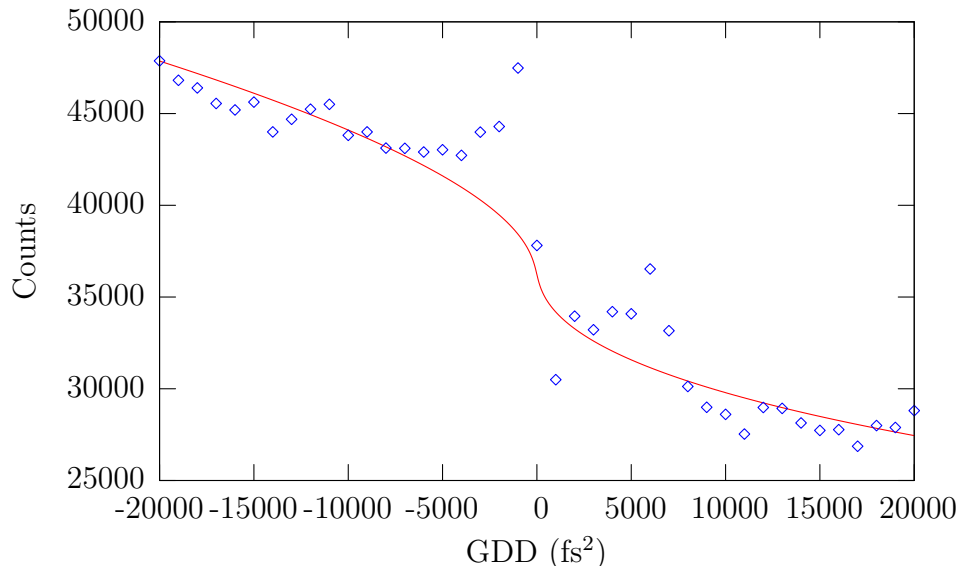


Figure 4.17: A simple calculation based on the work of Merkel *et al.*<sup>28</sup> (solid line), superimposed on experimental data. There are two free parameters, adjusted by hand, in this calculation. One is the position of the intermediate level, and the other is an overall scale factor. The transition wavelengths determined are 780.4 nm and 779.6 nm for the upper and lower transitions, respectively.

the data is difficult, if not impossible, to reproduce with this calculation. More levels can be added to the calculation to add structure, but gain in the understanding of the process is negligible. Clearly there is ample room here for future investigation, both experimental and theoretical.

A sinusoidal phase has more free parameters and has an interesting temporal profile. The Jacobi-Anger identity,

$$\exp(iz \cos(\theta)) = \sum_{n=-\infty}^{\infty} i^n J_n(z) \exp(in\theta), \quad (4.13)$$

implies that the temporal profile of a pulse that has been shaped to have the sinusoidal phase of Eq 4.12 is given by

$$E(t) = \sum_{n=-\infty}^{\infty} J_n(A) e^{-i\omega(t-T)} e^{in\phi} \quad (4.14)$$

which is plotted in Fig 4.18. The peaks in the temporal domain are separated by  $T$ , have relative amplitudes given by the J Bessel functions, and have a relative phase that changes by  $\phi$  from pulse to pulse. Each pulse is, essentially a scaled replica of the input pulse.

Applying pulses having this profile, and varying  $T$  and  $\phi_0$  for a fixed value of  $A = 1.2$ , results in the count rate spectra in Fig 4.19, which can be compared to the theoretical spectrum in Fig 4.20. That the spectra are cyclic in  $\phi_0$  is hardly a surprise. The sloping

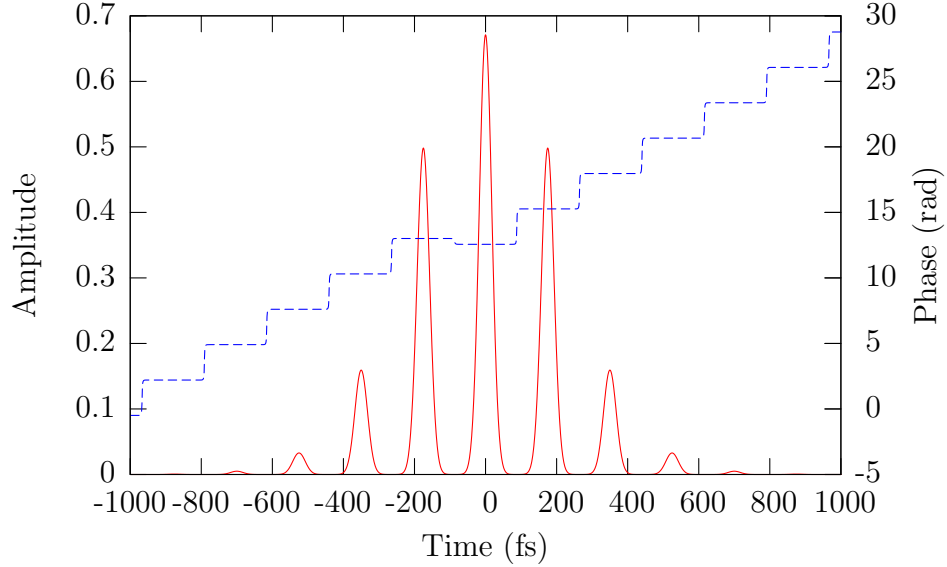


Figure 4.18: Temporal shape of a sinusoidal phase profile applied to a pulse. In this example,  $T = 175$  fs,  $\phi = 2.7$  and  $A = 1.2$ . The red solid line is amplitude, while the blue dashed line is the relative phase.

features are, however, more interesting. The theory from Eq 2.6 suggests that yield will be highest when the phase is anti-symmetric around a transition wavelength, which partially compensates for the  $\pi$  phase shift across a resonance. The sine phase is anti-symmetric when the argument is zero. From this, the slope can be related to the resonant frequency of a transition by

$$\omega_{resonant} = \omega_0 - \left( \frac{dT}{d\phi_0} \right)^{-1}. \quad (4.15)$$

Here, two wavelengths are revealed,  $\sim 781$  nm and  $\sim 783$  nm in the long TOF gated case. This agrees nicely with the spectral notch experiments.

The most striking feature of the sinusoidal phase scan is the contrast, which is as high as a ratio of 230 between the highest peak and the lowest valley in the long TOF case. Even ungated, there is a 3.5 ratio.

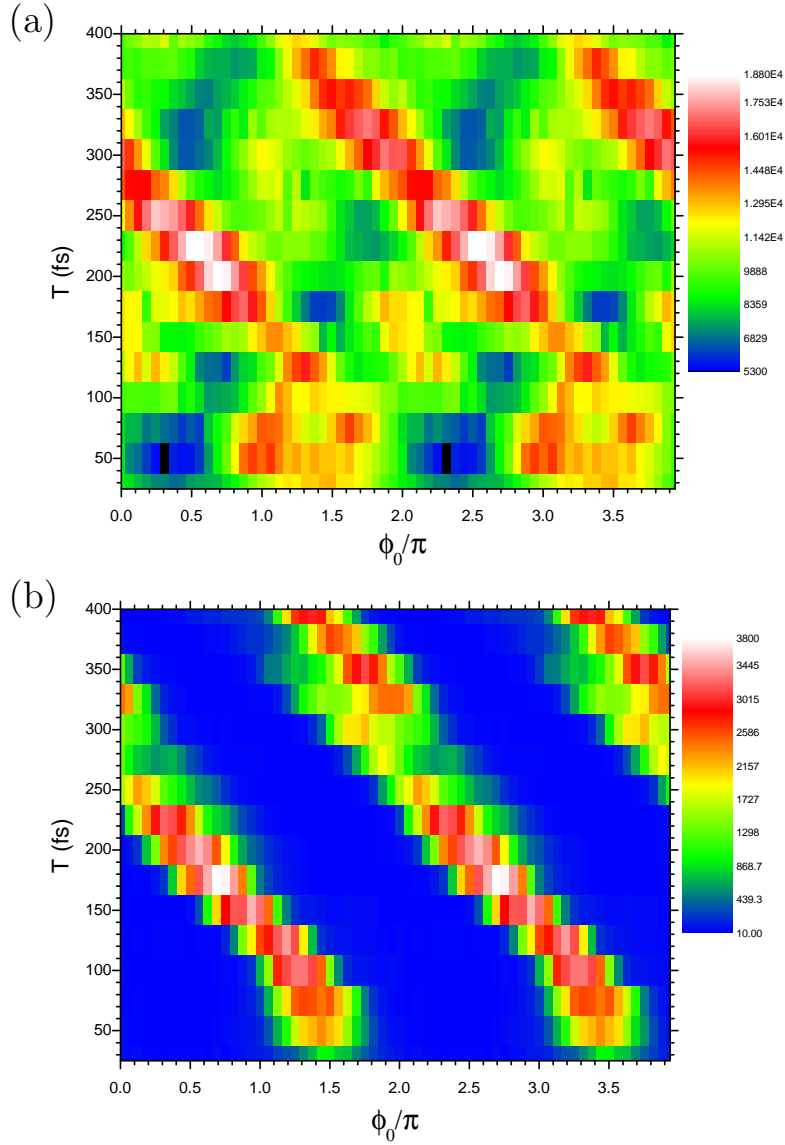


Figure 4.19: A plot of counts with a phase profile given by Eq 4.12 versus  $T$  and  $\phi_0$  gated on the entire PAI peak (a), or on the long TOF tails (b). The contrast is extremely large; a factor of 230 exists between the bin with the most counts and the bin with the least counts. The theoretical slopes of the features is given by Eq 4.15. The peaks near  $T = 175$  fs and  $\phi_0 = 0.75\pi$  and  $2.75\pi$  are the crossings of the ridges corresponding to the upper and lower transition wavelengths. The temporal shape that gives the most counts is shown in Fig 4.18.

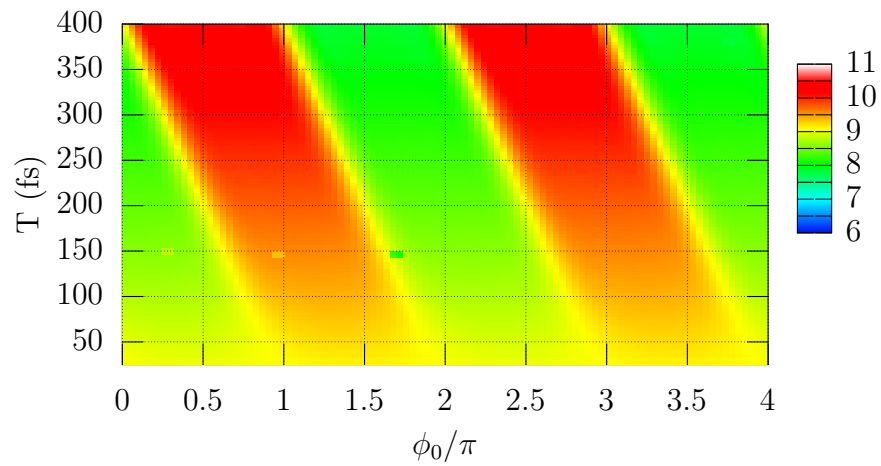


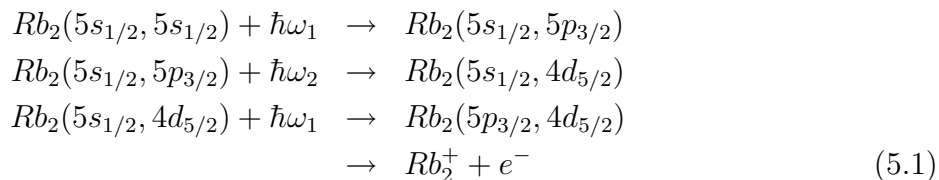
Figure 4.20: Theoretical result using the Dudovich model, namely Eq 2.6, for the count rate *versus*  $T$  and  $\phi_0$ . The slope is the same as for the experimental results in Fig 4.19(b), but the contrast is much smaller than experiment, and the width of the sloping ridges is also significantly wider than experiment. The reasons are currently unknown. The level structure used in these calculations is a three level ladder system with the upper and lower transitions having wavelengths of 781 nm and 783 nm respectively.

# Chapter 5

## Conclusions & Future Possibilities

### 5.1 CW PAI/PADI

The pathway for CW PAI has been determined for the case of two colors of photons, one slightly to the red of the  $5s_{1/2}F = 2 \rightarrow 5p_{3/2}F' = 3$  transition and the other slightly to the blue of the  $5p_{3/2}F = 3 \rightarrow 4d_{5/2}F' = 4$  transition. The deduced pathway is



where the last step is autoionization of the highly excited  $Rb_2$  molecule. This was determined from the quantitative dependence of count rate on intensity, which agreed nearly perfectly with theory, and the appearance of a PAI peak when the trap, which has a frequency near  $\omega_1$  is turned on after L1 and L2 are turned off. Additional support comes from the several linewidths detuning from atomic resonance of the lasers. It is recognized that other pathways could be opened up for other cw laser wavelengths, but when a narrow linewidth laser, detuned only slightly from the  $5s_{1/2}F = 2 \rightarrow 5p_{3/2}F' = 3$  resonance in  $^{87}Rb$  is used, the excitation pathway is limited to that of Eq 5.1.

The energy spectrum of the CW PADI peak has been measured. It has a width at half-max of 13.5 meV total kinetic energy release for the process. This was determined from momentum measurements in a calibrated momentum spectrometer.

### 5.2 KLS PAI

It has been shown that, in the case of the ultrafast PAI process involving an ultrafast pulse near 790 nm and a quasi-CW laser near the  $5p_{3/2} \rightarrow 4d_{5/2}$  transition in atomic Rb, important wavelengths in the ultrafast laser are 795 nm and a number of wavelengths near 780 nm.



The various measurements seem to probe slightly different pathways in that different intermediate and final molecular states are important in the excitation to the  $\text{Rb}_2^+$  state. The results are in qualitative agreement with a simple model based on second order perturbation theory.

The coarse pathway has been determined to consist of two ultrafast photons and then an L2 photon absorbed. This makes sense when one considers that the excitation rates that can be achieved with a quasi-cw laser are not sufficient to excite a sizable population in the short time that the ultrafast pulse is present. Further verification of this was obtained by delaying L2 with respect to the ultrafast KLS pulse.

Control of the KLS PAI count rate has been demonstrated. The amount of control, as measured by the contrast between high and low count rate configurations, is extremely high. In the case of a sinusoidal phase profile, this contrast is as high as 230. This contrast, and the high sensitivity of the process to the specifics of a sinusoidal phase are not in agreement with theory. The reasons for this are currently unknown.

### 5.3 Summary

An experimental apparatus was constructed and/or retooled to study the PAI and PADI processes in cold atomic vapor. Because of the range of experiments conducted, a great deal of flexibility had to be incorporated into the hardware and software alike. Especially in the case of ultrafast laser PAI, the starting point for understanding the physics was starting from square one. That is, these experiments were—and are—the only ones of their kind. No other group has used the spectral *phase* of an ultrafast pulse to do spectroscopy, even the relatively coarse spectroscopy presented here. Even in the case of CW PAI, no other group has investigated the higher excited states, or three photon PAI. In the case of Rb, no group has investigated collisional PAI of any kind. These experiments also led to the discovery of PADI, a process that has not been observed by any other group. Quite a lot of experimental machinery had to be developed in order to do these experiments; some of these are described in the appendices. Generally speaking, each of these are novel devices, conceived of and implemented for the first time, to our knowledge.

### 5.4 Future

Currently, the frequencies of the CW lasers are fixed. This limits the ability to obtain information about the system. A future direction of investigation would be to attempt PAI spectroscopy of the excited states along the indicated pathway. Some of the required apparatus has been developed, but more lasers are needed to do the experiment properly. Even in the KLS PAI experiments, being able to vary the frequency of L2 could potentially provide a large amount of information, and help in exhibiting more control. Control is paramount to the stated eventual goal of producing cold trapped molecules.

The ultrafast spectroscopy from section 4.2.3 is predicted<sup>42</sup> to be sensitive to  $\lambda_0$ , the center wavelength of the ultrafast pulse. This can be changed, to a limited degree, by

the Dazzler, allowing more extensive tests of models. In other systems<sup>43</sup> pulse fluence has some effect on the detail of the spectra. There is preliminary evidence for this in these experiments as well. Varying the fluence would provide an interesting check of the limits of the perturbation model.

On the control front, there is a lot more that could be done. A genetic algorithm, or some other optimization algorithm would be able to find the optimal pulse shape for PAI production. Additionally, it may be possible to limit the PAI production to a particular range of incubation times, indicating that a single optimal state has been excited. This would be useful for the eventual work on bringing the population back down from the excited states into the ground vibrational state of the molecule.

While a lot has been done on this system, there is a huge amount still to be done. The foundation has been constructed and the possibilities are impressive.

# Bibliography

The red numbers at the end of each reference refer to the pages in which the reference was cited.

- [1] A. E. Leanhardt, T. A. Pasquini, M. Saba, A. Schirotzek, Y. Shin, D. Kielpinski, D. E. Pritchard, and W. Ketterle, “Cooling Bose-Einstein Condensates Below 500 Picokelvin,” *Science* **301**, 1513–1515 (2003). **1**
- [2] C. Monroe, W. Swann, H. Robinson, and C. Wieman, “Very cold trapped atoms in a vapor cell,” *Phys. Rev. Lett.* **65**, 1571–1574 (1990). **1**
- [3] H. Metcalf and P. van der Straten, “Cooling and trapping of neutral atoms,” *Phys. Rep.* **244**, 203 (1994). **1**
- [4] G. Herzberg, *Molecular Spectra and Molecular Structure: I. Spectra of Diatomic Molecules*, 2 ed. (D. Van Nostrand Company, Inc., 1950), Vol. 1. **1, 9**
- [5] R. Dörner, V. Mergel, O. Jagutzki, L. Spielberger, J. Ullrich, R. Moshammer, and H. Schmidt-Böcking, “Cold Target Recoil Ion Momentum Spectroscopy: a ‘momentum microscope’ to view atomic collision dynamics,” *Phys. Rep.* **330**, 95–192 (2000). **1**
- [6] D. R. Miller, “Free Jet Sources,” in *Atomic and Molecular Beam Methods*, G. Scoles, ed., (Oxford University Press, 1988), Vol. 1, pp. 14–53. **1**
- [7] S. Y. T. van de Meerakker, P. H. M. Smeets, N. Vanhaecke, R. T. Jongma, and G. Meijer, “Deceleration and Electrostatic Trapping of OH Radicals,” *Phys. Rev. Lett.* **94**, 023004 (2005). **1**
- [8] D. Egorov, T. Lahaye, W. Schollkopf, B. Friedrich, and J. M. Doyle, “Buffer-gas cooling of atomic and molecular beams,” *Phys. Rev. A* **66**, 043401 (2002). **1**
- [9] E. A. Donley, N. R. Claussen, S. T. Thompson, and C. E. Wieman, “Atom-molecule coherence in a Bose-Einstein condensate,” *Nature* **417**, 529–533 (2002). **1**
- [10] S. Ospelkaus, A. Pe’er, K. Ni, J. J. Zirbel, B. Neyenhuis, S. Kotochigova, P. S. Julienne, J. Ye, and D. S. Jin, “Ultracold dense gas of deeply bound heteronuclear molecules,” *Phys. Rev. Lett.* , (2008), submitted. **1, 2, 6**
- [11] H. R. Thorsheim, J. Weiner, and P. S. Julienne, “Laser-induced photoassociation of ultracold sodium atoms,” *Phys. Rev. Lett.* **58**, 2420–2423 (1987). **2**

- [12] P. D. Lett, K. Helmerson, W. D. Phillips, L. P. Ratliff, S. L. Rolston, and M. E. Wagshul, “Spectroscopy of  $\text{Na}_2$  by photoassociation of laser-cooled Na,” *Phys. Rev. Lett.* **71**, 2200–2203 (1993). [2](#)
- [13] J. D. Miller, R. A. Cline, and D. J. Heinzen, “Photoassociation spectrum of ultracold Rb atoms,” *Phys. Rev. Lett.* **71**, 2204–2207 (1993). [2](#)
- [14] D. Hoffmann, P. Feng, and T. Walker, “Measurements of Rb trap-loss collision spectra,” *J. Opt. Soc. Am. B* **11**, 712–720 (1994). [2](#), [3](#), [11](#), [12](#)
- [15] M. Kemmann, I. Mistrik, S. Nussmann, and H. Helm, “Near-threshold photoassociation of  $^{87}\text{Rb}_2$ ,” *Phys. Rev. A* **69**, 022715 (2007). [3](#), [9](#), [10](#), [11](#)
- [16] A. N. Nikolov, E. E. Eyler, X. T. Wang, J. Li, H. Wang, W. C. Stwalley, , and P. L. Gould, “Observation of Ultracold Ground-State Potassium Molecules,” *PRL* **82**, 703–706 (1999). [3](#)
- [17] A. N. Nikolov, J. R. Ensher, E. E. Eyler, H. Wang, W. C. Stwalley, and P. L. Gould, “Efficient Production of Ground-State Potassium Molecules at Sub-mK Temperatures by Two-Step Photoassociation,” *PRL* **84**, 246–249 (2000). [3](#)
- [18] E. Tiesinga, C. J. Williams, and P. S. Julienne, “Near-threshold photoassociation of  $^{87}\text{Rb}_2$ ,” *Phys. Rev. A* **57**, 4257–4267 (1998). [3](#)
- [19] K. M. Jones, P. S. Julienne, P. D. Lett, W. D. Phillips, E. Tiesinga, and C. J. Williams, “Measurement of the atomic  $\text{Na}(3P)$  lifetime and of retardation in the interaction between two atoms bound in a molecule,” *Europhys. Lett.* **35**, 85 (1996). [3](#)
- [20] P. L. Gould, P. D. Lett, P. S. Julienne, W. D. Phillips, H. R. Thorsheim, and J. Weiner, “Observation of associative ionization of ultracold laser-trapped sodium atoms,” *Phys. Rev. Lett.* **60**, 788–791 (1988). [3](#)
- [21] P. S. Julienne and R. Heather, “Laser modification of ultracold atomic collisions: Theory,” *Phys. Rev. Lett.* **67**, 2135–2138 (1991). [3](#)
- [22] D. Leonhardt and J. Weiner, “Direct two-color photoassociative ionization in a rubidium magneto-optic trap,” *Phys. Rev. A* **52**, R4332–R4335 (1995). [4](#)
- [23] M. L. Trachy, G. Veshapidze, M. H. Shah, H. U. Jang, and B. D. DePaola, “Photoassociation in Cold Atoms via Ladder Excitation,” *Phys. Rev. Lett.* **99**, 043003 (2007). [5](#)
- [24] D. DeMille, “Quantum Computation with Trapped Polar Molecules,” *Phys. Rev. Lett.* **88**, 067901 (2002). [6](#)
- [25] S. Kallush and R. Kosloff, “Momentum control in photoassociation of ultracold atoms,” *Phys. Rev. A* **76**, 2053408 (2007). [6](#)

- [26] J. K. G. Watson, “Reflection symmetries of linear-molecular rovibronic levels,” *J. Mol. Spec.* **145**, 130–141 (1991). [11](#)
- [27] A. Gallagher and D. E. Pritchard, “Exoergic Collisions of cold  $\text{Na}^*\text{-Na}$ ,” *Phys. Rev. Lett.* **63**, 957–960 (1989). [11](#)
- [28] W. Merkel, H. Mack, W. P. Schleich, E. Lutz, G. G. Paulus, and B. Girard, “Chirping a two-photon transition in a multistate ladder,” *Phys. Rev. A* **76**, 023417 (2007). [13](#), [48](#), [49](#)
- [29] N. Dudovich, B. Dayan, S. M. G. Faeder, and Y. Silberberg, “Transform-Limited Pulses Are Not Optimal for Resonant Multiphoton Transitions,” *Phys. Rev. Lett.* **86**, 47–50 (2001). [13](#), [42](#)
- [30] B. D. DePaola, R. Morgenstern, and N. Anderson, “MOTRIMS: Magneto-Optical Trap Recoil Ion Momentum Spectroscopy,” in *Advances in Atomic, Molecular, and Optical Physics*, E. Arimondo, P. Berman, and C. C. Lin, eds., (Elsevier Science & Technology Books, 2008), Vol. 55, pp. 139–189. [15](#)
- [31] H. Nguyen, X. Fléchar, R. Brédy, H. A. Camp, and B. D. DePaola, “Recoil ion momentum spectroscopy using magneto-optically trapped atoms,” *Rev. Sci. Instrum.* **75**, 2638–2647 (2004). [15](#)
- [32] M. A. Gearba, H. A. Camp, M. L. Trachy, G. Veshapidze, M. H. Shah, H. U. Jang, and B. D. DePaola, “Measurement of population dynamics in stimulated Raman adiabatic passage,” *Phys. Rev. A* **76**, 013406 (2007). [15](#)
- [33] M. H. Shah, H. A. Camp, M. L. Trachy, G. Veshapidze, M. A. Gearba, , and B. D. DePaola, “Model-independent measurement of the excited fraction in a magneto-optical trap,” *Phys. Rev. A* **75**, 053418 (2007). [15](#)
- [34] H. Nguyen, Ph.D. thesis, Kansas State University, Manhattan, KS, 2003. [15](#)
- [35] M. H. Shah, Ph.D. thesis, Kansas State University, Manhattan, KS, 2006. [15](#), [75](#)
- [36] H. A. Camp, Ph.D. thesis, Kansas State University, Manhattan, KS, 2005. [15](#), [74](#), [75](#)
- [37] FASTLITE, 45-47 rue Croulebarbe, 75013 Paris, France. [22](#)
- [38] F. Verluise, V. Laude, Z. Cheng, C. Spielmann, and P. Tournois, “Amplitude and phase control of ultrashort pulses by use of an acousto-optic programmable dispersive filter: pulse compression and shaping,” *Opt. Lett.* **25**, 575–577 (2000). [22](#)
- [39] A. Jraj, A. Allouche, M. Korek, and M. Aubert-Frécon, “Theoretical electronic structure of the alkali-dimer cation  $\text{Rb}_2^+$ ,” *CP* **290**, 129 (2003). [30](#), [33](#)
- [40] M. Frécon, private communication, 2006. [30](#), [33](#)

- [41] G. Veshapidze, M. L. Trachy, H. U. Jang, C. W. Fehrenbach, and B. D. DePaola, “Pathway for two-color photoassociative ionization with ultrafast optical pulses in a Rb magneto-optical trap,” *Phys. Rev. A* **76**, 051401(R) (2007). 35, 37
- [42] H. Suchowski, private communication, 2008. 54
- [43] C. Trallero-Herrero and T. C. Weinacht, “Transition from weak- to strong-field coherent control,” *PRA* **75**, 063401 (2007). 55
- [44] K. Schäfer, W. Y. Baek, K. Förster, D. Gassen, and W. Neuwirth, “Analysis of initial energies of fragments produced by 65-keV proton-molecule collisions using a time-of-flight mass spectrometer,” *Z. Phys. D* **21**, 137 (1991). 62
- [45] C. Combaret, “CAMAC TTL/NIM Translator,” 2004. 64, 66
- [46] H. U. Jang, J. Blicke, G. Veshapidze, M. L. Trachy, and B. D. DePaola, “An auto-incrementing nanosecond delay circuit,” *Rev. Sci. Instrum.* **78**, 094702 (2007). 66
- [47] U. Schünemann, H. Engler, R. Grimm, M. Weidemüller, and M. Zielonkowski, “Simple scheme for tunable frequency offset locking of two lasers,” *Rev. Sci. Instrum.* **70**, 242 (1999). 66

# Appendix A

## Nearest Neighbors

The nearest neighbor distribution equation given in section 2.3 can be easily derived from first principles. First we define that we want the probability that, given a particle, the nearest neighbor is between  $R$  and  $R + dr$  away.

We have a particle, called the reference particle, in a volume  $V$ . The probability that any given particle is between  $R$  and  $R + dr$  from the reference particle is simply the ratio of the volume of the shell, with radius  $R$  and thickness  $dr$ , and the total volume,  $V$ , which is

$$\frac{4\pi R^2 dr}{V}. \quad (\text{A.1})$$

The probability that we place a particle more than a distance  $R$  from the reference particle is given by the ratio of the volume outside the shell to the total volume, or

$$\frac{V - \frac{4}{3}\pi R^3}{V} = 1 - \frac{\frac{4}{3}\pi R^3}{V}. \quad (\text{A.2})$$

The probability, then that  $N - 2$  particles are placed more than a distance  $R$  from the reference particle is given by Eq A.2 raised to the power  $N - 2$ ,

$$\left(1 - \frac{\frac{4}{3}\pi R^3}{V}\right)^{N-2}. \quad (\text{A.3})$$

This can also be written as

$$\left(1 - \frac{\frac{4}{3}\pi R^3}{(N-2)\frac{V}{N-2}}\right)^{N-2}. \quad (\text{A.4})$$

As  $N$  becomes large, this approaches

$$\exp\left(-\frac{4}{3}\rho\pi R^3\right), \quad (\text{A.5})$$

where  $\rho$  is the number density,  $N/V$ .

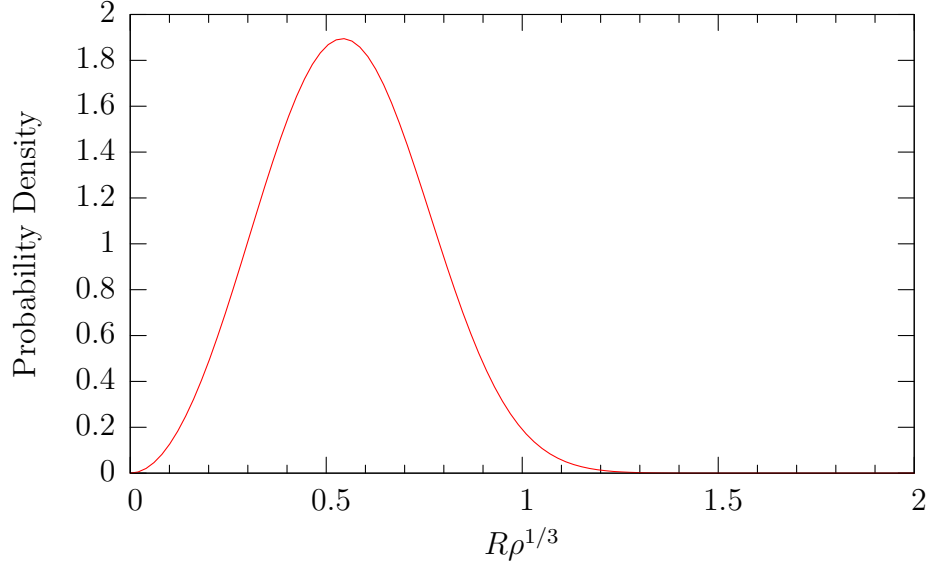


Figure A.1: A plot of the probability that the nearest neighbor of a particle will be between  $R$  and  $R + dR$  away.

The probability, then, of the first particle (after the reference particle) being a distance between  $R$  and  $R + dr$  from the reference particle, and  $N - 2$  others being more than a distance  $R$  away from the reference particle, is simply the product of Eq A.1 and Eq A.5 or

$$\frac{4\pi R^2 dR}{V} \exp\left(-\frac{4}{3}\rho\pi R^3\right). \quad (\text{A.6})$$

However, since we don't care *which* of the  $N - 1$  non-reference particles is the nearest neighbor, we must multiply Eq A.6 by  $N - 1 \approx N$  to get the final result of

$$4\pi\rho R^2 dR \exp\left(-\frac{4}{3}\rho\pi R^3\right). \quad (\text{A.7})$$

A plot of this result is shown in Fig A.1.



# Appendix B

## TOF to KER derivation

A well characterized momentum spectrometer, like the one in the setup described in this thesis, can be used to measure the kinetic energy of ions produced in the target. One method of doing this requires only a TOF spectrum and the calibration for the spectrometer<sup>44</sup>.

The spectrometer is designed to linearly map the component of the momentum of an ion parallel to the extraction axis of the spectrometer,  $p_{\parallel}$ , to TOF,  $t$ . This relationship is given by

$$t = t_0 + Bp_{\parallel} \quad (\text{B.1})$$

where  $t_0$  and  $B$  are given by the spectrometer calibration. From this, it is easy to see that the energy corresponding to that momentum,  $E$ , is given by

$$E = A(t - t_0)^2 \quad (\text{B.2})$$

where  $A$  is related to  $B$ . The SIMION calculations for the spectrometer actually give  $A$ .

Assuming the motion of the ions is isotropic, (which is reasonable in the work here, since the electron is ejected via autoionization), the distribution of momenta for a given energy corresponds to a spherical shell of radius  $\sqrt{2mE}$  where  $m$  is the mass of the ion. The distribution of momenta parallel to the extraction axis is the same as the projection of a spherical shell onto the axis of extraction,  $\hat{z}$ . A volume element on a spherical shell of radius  $R$  is given by

$$dV = \sin(\theta)R^2d\theta d\phi dr \quad (\text{B.3})$$

where  $dr$  is the thickness of the shell,  $\theta$  is the polar angle and  $\phi$  is the azimuthal angle. Since  $z = R\cos(\theta)$ ,  $dz = R\sin(\theta)d\theta$  and the area element becomes

$$dV = dzRd\phi dr, \quad (\text{B.4})$$

which implies that the projection of a spherical shell onto an axis is simply a rectangle with a width equal to the diameter of the sphere, and a height of  $2\pi Rdr$ . The TOF spectrum of a number of ions,  $N$  with energy between  $E$  and  $E + dE$  is equal to a rectangle with width  $\sqrt{E/A}$ , height  $N\sqrt{A/E}/2$  and centered on  $t_0$ .

Given a TOF spectrum  $C_t(t)$ , the number of counts with energies between  $E$  and  $E+dE$ ,  $C_E$  is given by

$$dC_t(t)\tau = C_E(E)dE \quad (\text{B.5})$$

where  $\tau = \sqrt{E/A} = |t - t_0|$ . Dividing both sides by  $dt$  and rearranging terms gives

$$C_E(E) = \left(\frac{dE}{dt}\right)^{-1} \frac{dC_t(t)}{dt} \tau. \quad (\text{B.6})$$

Substituting Eq B.2 results in

$$C_E(E) = 2 \left| \frac{dC_t(t)}{dt} \frac{1}{2A} \right| \quad (\text{B.7})$$

For the spectrometer used in this thesis,  $A = 3.75 \times 10^{-5} \text{ meV/ns}^2$ . Note that since two TOFs correspond to the same energy, the rising and falling edges of the TOF peak each gives an energy spectrum.

The error bar in the energy due to an uncertainty in  $t_0$  is given by

$$\delta E = 2\sqrt{A}\delta t_0\sqrt{E} \quad (\text{B.8})$$

for the spectrometer used in this thesis, the HWHM of the PAI peak (used as an estimate of  $\delta t_0$ ) of 30 ns and the width at half max of the PADI distribution of 7 meV for the ion, the uncertainty in energy is

$$\delta E = 2\sqrt{3.75 \times 10^{-5}} \times 30 \text{ ns} \sqrt{7 \text{ meV}} = 0.97 \text{ meV}, \quad (\text{B.9})$$

for the ion, or 1.9 meV for the KER.

# Appendix C

## Circuits

### C.1 Delay stepping

The programmable delay stepper circuit used in the KLS-L2 delay experiment described in subsection 4.2.2 allows the delay between two pulses to be stepped through up to 256 different values in increments on the nanosecond scale. The schematic for the circuit is shown in Fig C.1. The heart of the circuit is the DS1023 programmable delay line chip from Maxim Semiconductor. The chip comes in 5 varieties, with step increments ranging from 250 ps to 5 ns. For the experiment described, the 5 ns version was used. The chip can be programmed with either a 3-wire serial interface or an 8-bit parallel interface. The parallel interface was chosen for this circuit to ease the planning and design.

In this circuit the chip is programmed by the outputs of a pair of 4-bit counters, U1 and U2. The counters are counting the pulses from a 555 timer chip, U3. The output bits of the counters are masked by the switches S1-S8, which allows the setting of the size of the step, in powers of two times the step size of the delay line chip, and the number of steps. U4 and U7 are hexadecimal display chips that show the values on the counters, meaning the step number that the circuit is currently on. The input to the circuit, labeled “START” in the diagram, is a TTL level pulse. The pulse is then delayed by some amount, which is a constant determined by the chip, plus the programmed delay. The output TTL level pulse is then passed through two logic inverters to buffer the pulse and remove noise. The delayed TTL output comes out from the circuit at the point labeled “TO AOM”. The parts of the circuit that are highlighted in blue boxes are TTL to NIM level converters<sup>45</sup>, used because the CAMAC electronics used, namely the TDC and Event Trigger, take NIM level signals. The output labeled “TO TDC START” is just a level translated copy of the input signal, while the output labeled “TO TDC STOP” is a level translated copy of the output signal. The output labeled “TO EVENT TRIG” is a NIM level pulse that is produced every time the 555 timer chip pulses, to allow the data acquisition system to monitor when the step number has changed.

The circuit has only one external control, labeled “POT1” in the schematic. (The mask switches are user settable, but are situated on the circuit board and are not accessible

- 0.1 uF bypass caps on power to U1, U2, U3 & U4
- Pots 1 & 4 are off-board.
- Pots 2 & 3 are on-board.

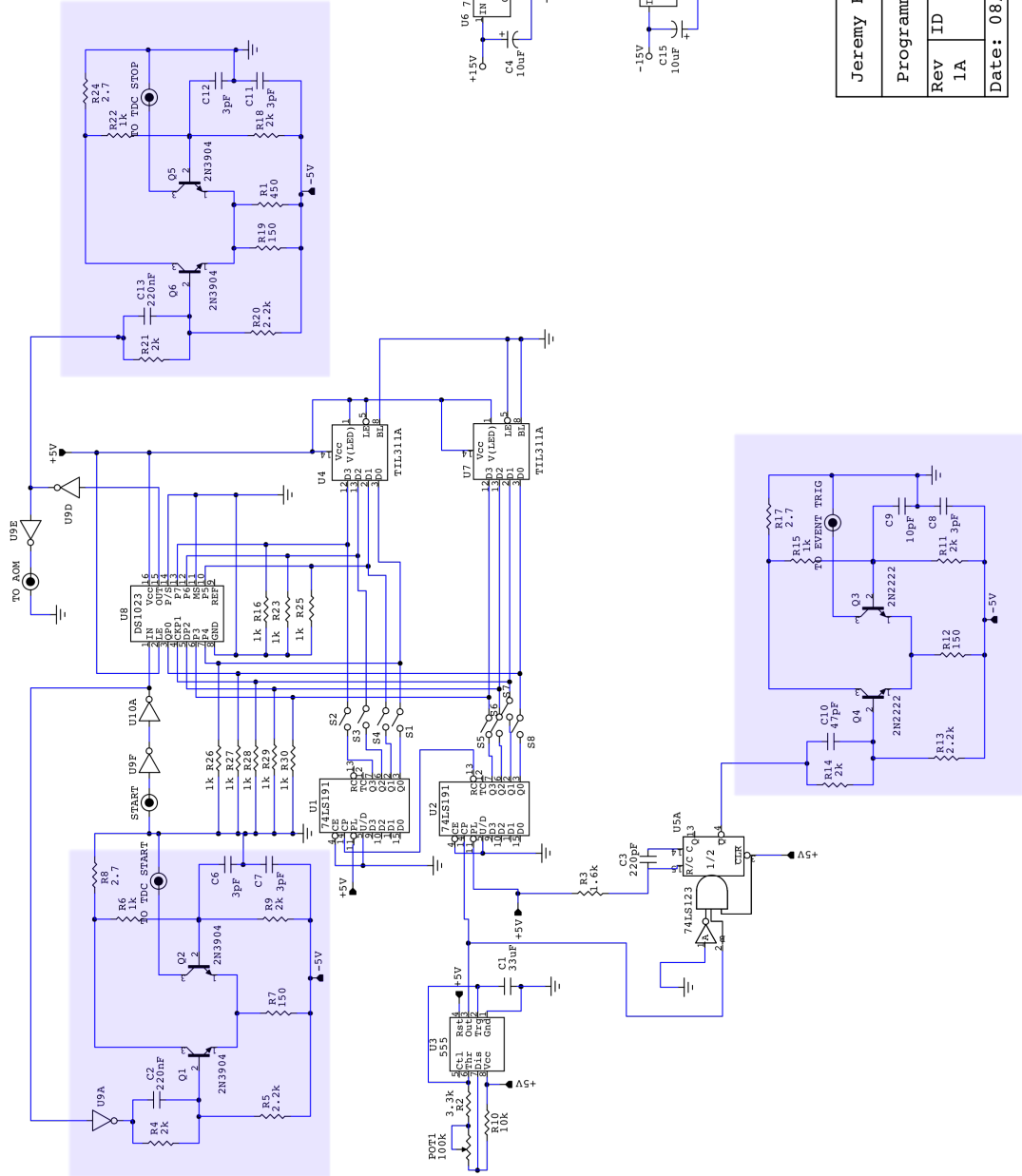


Figure C.1: Schematic for the programmable delay stepper

Jeremy Blicek	
Programmable Delay	
Rev	ID
1A	Programmable_Delay_VIA.ckt
Date:	08/9/2006
Page: 1 of 1	

without opening the circuit enclosure.) This potentiometer controls the amount of time spent on each step, from 380 ms to 5 s.

This circuit, as well as a simple example of another experiment using it, has been published by Jang *et al.*<sup>46</sup>.

## C.2 Delay Gate

The main delay gate generator used in most of the KLS experiments takes a single TTL signal as an input, and produces a number of outputs including a TTL to NIM level translated version of the input, and two TTL level delayed gates. The schematic is given in Fig C.2.

It is composed mostly of two 74LS123 chips (U1 and U2), which are dual monostable multivibrators, also called one-shots. Each of the '123 chips controls one of the delayed gates. The first one-shot in each chip (U1B and U2B) controls the delay between the input pulse and the beginning of the gate, while the second one-shot (U1A and U2A) control the width of each gate. The part of the circuit in the blue box is a TTL to NIM level converter<sup>45</sup>.

The controls for this circuit consist of one potentiometer to control each time, giving a total of four pots, and the switch labeled “S1” in the diagram which toggles a logic inverter on the input.

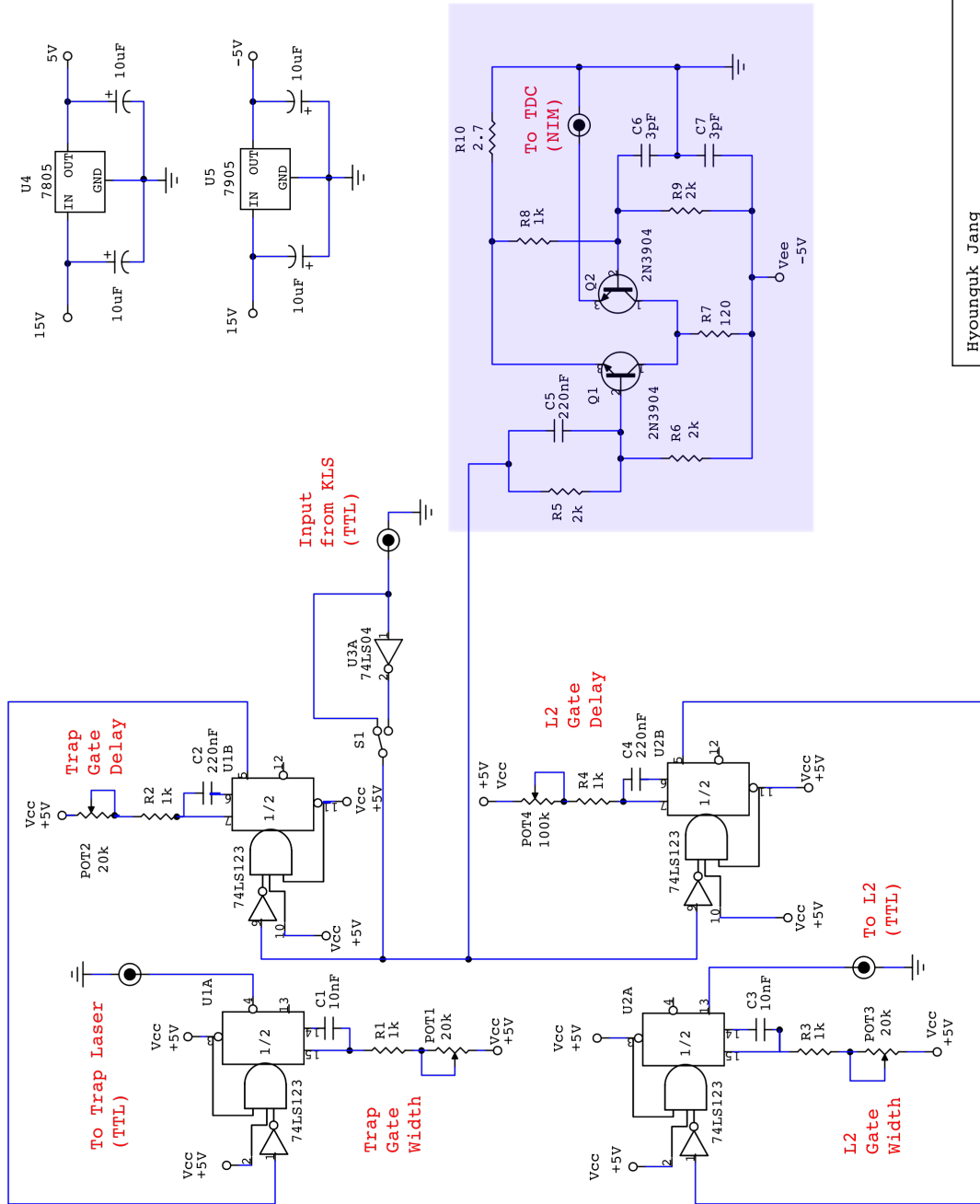
## C.3 Optical beat note lock

The optical beat note lock is a circuit which allows one to lock the frequency difference between two lasers with  $\sim 2$  MHz precision over a range from 50 MHz to 1.1 GHz. It is based on the work of Schünemann *et al.*<sup>47</sup>.

The circuit, shown in block diagram format in Fig C.3, works by beating the a reference frequency,  $\omega_1$  against the optical beat note,  $\omega_{optical}$  detected by a photodiode in a Radio Frequency (RF) mixer. This electrical beat note, called  $\omega_2 = |\omega_1 - \omega_{optical}|$  is measured by an interferometer. The interferometer consists of a power splitter, a delay line made of a length of coaxial cable, and a phase detector. The RF power is split, and one half of the signal is delayed in the delay line. The phase shift caused by the delay is proportional to the frequency,  $\omega_2$ . The two halves are then combined in a phase detector. When the phase difference between the two halves is equal to  $\pi/2$ , the voltage output of the phase detector is zero. Then an external PID controller (also designed and constructed in house, but not shown) is used to alter the frequency of the laser in order to keep the voltage zero.

By changing the reference frequency, it is possible to change the frequency difference between the two lasers. The range of reference frequency is, however, generally beyond that of inexpensive Voltage Controlled Oscillators (VCOs). To get this range, two VCOs, which can produce frequencies between 1 GHz and 2.2 GHz are used. One of the VCOs is kept at a constant 1 GHz, while the other is used to tune the frequency. The two VCOs are mixed, and the beat note between the two is the reference frequency  $\omega_1$ .

When mixing two sine waves together in an RF mixer, the result is both the sum and the difference frequency. In this circuit, the sum frequency is always filtered out, except



Hyounguk Jang	
Laser Gate and Delay	
Rev	ID
1A	gate_delay_01A
Date:	11/06/2006
Page: 1 of 1	

Figure C.2: Schematic for the delay gate

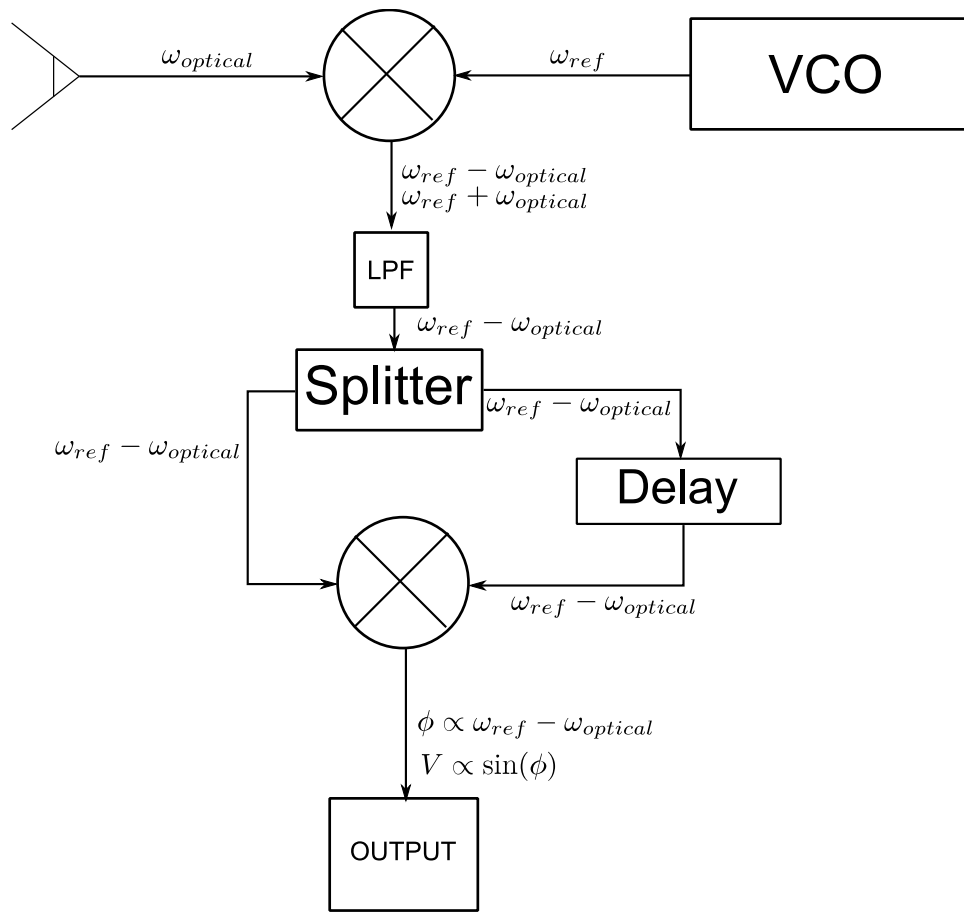


Figure C.3: Block diagram for the optical beat note lock (beat box)





	$\omega_{laser1} > \omega_{laser2}$	$\omega_{laser1} < \omega_{laser2}$
$\omega_{optical} > \omega_1$	A	B
$\omega_{optical} < \omega_1$	B	A

Table C.1: The four possibilities for the relationship between the frequencies involved require different polarities for the PID feedback loop in the lock. These polarities are here called A and B, because there is an overall sign that depends on which laser is controlled (laser1 or laser2) by the loop and the internals of the laser itself.

after the phase detector, because the PID loop that is attached to the output of this circuit is not able to detect the sum frequency, so filtering is not necessary.

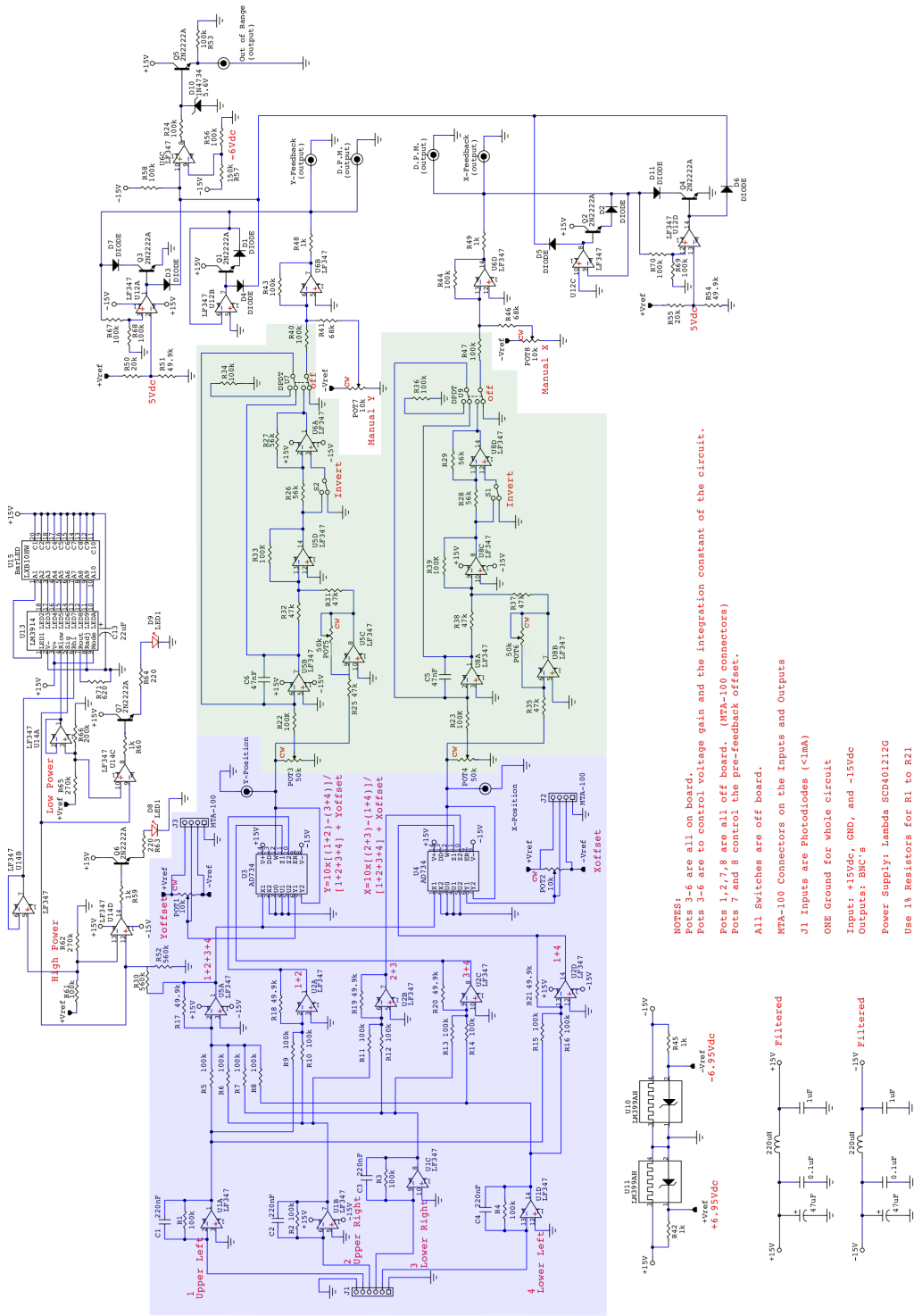
The circuit has a single RF input, namely the optical beat note. It also has a low frequency input, for example, a triangle wave, to control the reference frequency. This input is summed with the voltage determined from the position of the potentiometer labeled “R13” to give the voltage to the VCO. The reference frequency and optical beat note, after amplification are also output, to allow the user to monitor the frequencies with a frequency counter.

In operation, there are four different possibilities for the relationship between the two laser frequencies and the reference frequency. Laser 1 can have a higher or lower frequency than laser 2, and the optical beat note can be higher or lower in frequency than the reference frequency. These four possibilities will have different effects on the laser locking. Either the output voltage, which the PID loop tries to keep at zero will increase or decrease with increasing laser frequency (assuming the other laser is constant). These four possibilities are outlined in table C.1. The circuit was designed by this thesis author, and laid out by KSU’s Electronic Design Laboratory.

## C.4 Pointing Stabilizer (ALPS)

The Automatic Laser Pointing Stabilizer (ALPS) is a very general purpose beam stabilizer. It has seen heavy use in other experiments, mostly conducted by another group. It uses a PI feedback loop and a PZT mirror to stabilize the beam position on a detector. Using two of these circuits stabilizes the beam position in all four degrees of freedom. The circuit diagram in Fig C.5 can be looked at in terms of two different blocks. The first, in the blue box in the diagram, is a circuit to compute the beam position relative to the center of a simple photodiode quadrant detector. The second part of the circuit, in the green box in the diagram, is a pair of simple PI controllers that work to keep the position voltages computed in the first step at zero. The entire control circuit is composed of analog electronics. This allows for a wide range of applicability from CW lasers to pulsed lasers with relatively low pulse repetition rates (tested at 1 kHz). Extension to even lower repetition rates can be easily accomplished by changing the filter capacitor in the input stage.

The circuit contains a number of nice features including over-range signaling, and a power monitor which informs the user of the amount of laser power on the detector compared to



**NOTES:**  
 Pots 3-6 are all on board.  
 Pots 3-6 are to control voltage gain and the integration constant of the circuit.  
 Pots 1,2,7,8 are all off board. (WPA-100 connectors)  
 Pots 7 and 8 control the pre-feedback offset.  
 All Switches are off board.  
 WPA-100 Connectors on the Inputs and Outputs  
 J1 Inputs are Photodiodes (<1mA)  
 ONE Ground for whole circuit  
 Inputs: +15Vdc, GND, and -15Vdc  
 Outputs: BMC's  
 Power Supply: Lambda SCD401212G  
 Use 1% Resistors for R1 to R21  
 For extra Precision use OP-497 for U1,U2  
 If using +/- 12V Power Supply, make sure u6B,u6D can reach +10V into 10k.  
 U15 off board  
 Total circuit current ~ 500 mA + 250 mA (High voltage P.S.) + 500 mA (if supplying shutter power)

Rev ID	Pointing_Stabilizer_04.ckt
1.1	
Date: 11/13/2007	Page: 1 of 1

Figure C.5: Schematic for the Automatic Laser Pointing Stabilizer (ALPS)

what the circuit should have for proper operation.

A manual for the use of the full device, including two ALPS circuits, high voltage amplifiers and panel meters monitoring the voltage supplied to the PZT mirrors is in appendix **F**. A provisional patent has been granted for this device.

# Appendix D

## Data Acquisition Software

The data acquisition software used in this work is entirely built on the SpecTcl package written by Ron Fox of Michigan State University. The software is open source, written in C++ and licensed under the GNU General Public License (GPL). This software is designed for passive event mode data acquisition. This means that the computer responds to notifications that an event has been measured by the hardware and collects this data, but is not designed to control the experiment in any way.

The SpecTcl software provides a base from which to build a usable data acquisition system. Many parts must be supplied by the user. As maintained by the lab's acquisition computer expert, Kevin Carnes, the readout part of the system is configured to use the CAMAC hardware that is in heavy use in the J. R. Macdonald lab. In this case, the part of the software that needs to be written by the user for data acquisition consists of the contents of a number of functions in the file `skeleton.cpp`. The most used of these functions are `initevt` which controls the initialization of the CAMAC system and any modules that need to be specifically initialized, `readevt` which handles the readout of the event data, and `clearevt` which is responsible for clearing the CAMAC modules.

In the experiments involving the Dazzler, the passive nature of the software was not appropriate. What is required is a method of controlling the Dazzler and letting the data acquisition computer know what the Dazzler had been instructed to do. Since the Dazzler is controlled by a LabVIEW program running on a Windows computer, the matter became complicated.

The Dazzler control computer, named Rabi, runs the LabVIEW program that comes with the Dazzler. This program can be configured to check for a file that tells it how to configure the Dazzler. The process works in the following steps. A file is written to a specific location, with a specific name, `C:\Program Files\Dazzler\request.txt`. This file contains the path to another file, which contains the configuration the Dazzler should be programmed with. The Dazzler software periodically checks for the existence of `request.txt` and, if it exists, reads it. The Dazzler software then programs the Dazzler with the contents of the file pointed to by `request.txt`. Once this programming has been completed, and the Dazzler is using the new configuration, the Dazzler software deletes `request.txt`.

The readout program that comes with SpecTcl provides the capability to read a scaler at

user defined intervals. This capability is facilitated by a call to a function called `readscl`. To facilitate control of the Dazzler, code was inserted into `readscl` to write the `request.txt` file on Rabi's hard drive. This allows for the readout program on the data acquisition computer to change the Dazzler configuration at user defined intervals. The configurations are numbered, and the current configuration number is inserted into each event's data buffer.

In order to prevent events from being recorded while the Dazzler's configuration is uncertain, the `readscl` function blocks data acquisition until `request.txt` has been deleted by the Dazzler software. In the case that the Dazzler software is not configured to look for this file, and consequently doesn't delete it, `readscl` will block forever, effectively cutting off the stream of events.

SpecTcl proper is an event mode analysis system. It includes support for histogramming data of one or two parameters. Again, a number of functions need to be provided by the user. These functions are contained in the file `MySpecTclApp.cpp` and include the function operator of the `EventProcessor` object, which for historical reasons is called, for these experiments `STIRAP5EventProcessor`, since much of the code is reused from the days when the research group did STIRAP experiments<sup>36</sup>; the member function `onAttach`, which contains code that must be executed every time a new data source is attached, such as a new data file to be analyzed or attaching to the readout program; `onBegin`, which is executed when a new run begins, whether it is the start of a data file or a new run from the readout program directly; and `onEnd`, which runs every time a run ends.

In a typical experiment, a number of software parameters are needed to control the analysis, or sorting, of the incoming events. In SpecTcl, this is handled by interfacing the C++ program with a TCL interpreter. This allows the user significant flexibility in controlling the analysis. It also provides a way for the user to write "one off" scripts that can examine the contents of spectra and do operations on them. Much of the interface between the C++ program and the TCL interface takes the form of variables that can be accessed from either space. Each variable requires a few lines of C++ code to complete this interfacing. Early versions of SpecTcl did not run `onAttach` properly. For this reason this code was inserted into `onBegin`. Since the necessary code is much the same for each variable, a simple program was written to take a list of variable names and default values, and insert this code into `MySpecTclApp.cpp`. This simplifies life considerably.

A number of commands were also written in C++ to allow such operations as writing spectra in a format that is easily used in the popular scientific analysis program Origin; cropping spectra, to allow for smaller exports when only a portion of the original spectrum is of interest; and doing projections<sup>(1)</sup>. This code interfaces with the TCL interface, allowing simple Graphical User Interfaces (GUIs) to be constructed with TCL/Tk to improve the user experience. Many more advanced operations are possible, with the full power of the C++ programming language.

---

<sup>(1)</sup>While modern versions of SpecTcl come with support for projections, these projections must be taken over the area of a gate, which is often more of a pain than it's worth for these experiments.

# Appendix E

## Locking the Lasers

Laser locking is critical to many experiments involving cold atoms. Because of this, the MOTRIMS research group has put considerable time into improving the locks. Advances have been made in both the optics and the electronics.

In the PhD theses by Shah<sup>35</sup> and Camp<sup>36</sup>, the peak lock circuits are described. A diagram illustrating the central idea is in Fig E.1. Briefly, a signal is created, usually by dithering the laser frequency across a Doppler free absorption feature. This signal is then inverted halfway through the scan and integrated, effectively giving a voltage proportional to the left-right asymmetry of the signal. This inversion is obtained by simply passing the input signal through an amplifier that has a gain of 1 for the first half of the scan, and -1 for the other half. (It's actually a modulator/demodulator chip, but it works as described.) Any constant (DC) offset in the input signal should average out. However, like all electronics, this amplifier is not perfect. This imperfection gives a finite voltage when the left-right asymmetry is in fact zero when the DC offset is nonzero. In many cases this is not a large problem, and the circuit works very well, but since the PAI processes seem to be dependant on MOT density and temperature (both of which are functions of the trapping laser frequency) more control is needed to get good results. To obtain this control, it is important to filter out the DC component of the input signal.

The circuit measures the left-right asymmetry of the input signal, not the actual frequency of the laser with respect to the atomic resonance. A false left-right asymmetry can be created if the dither signal sent to the laser is not symmetric about zero. Traditional function generator chips like the MAX038 from Maxim Semiconductor claim a total harmonic distortion of 2%, but the signal can be seen on a scope to have unacceptable distortions in terms of the symmetry. In the current lock circuit, these function generator chips have been replaced with “low tech” Wein oscillators. These oscillators have significantly higher harmonic distortion, but the symmetry is good, making them more suitable to this locking circuit.

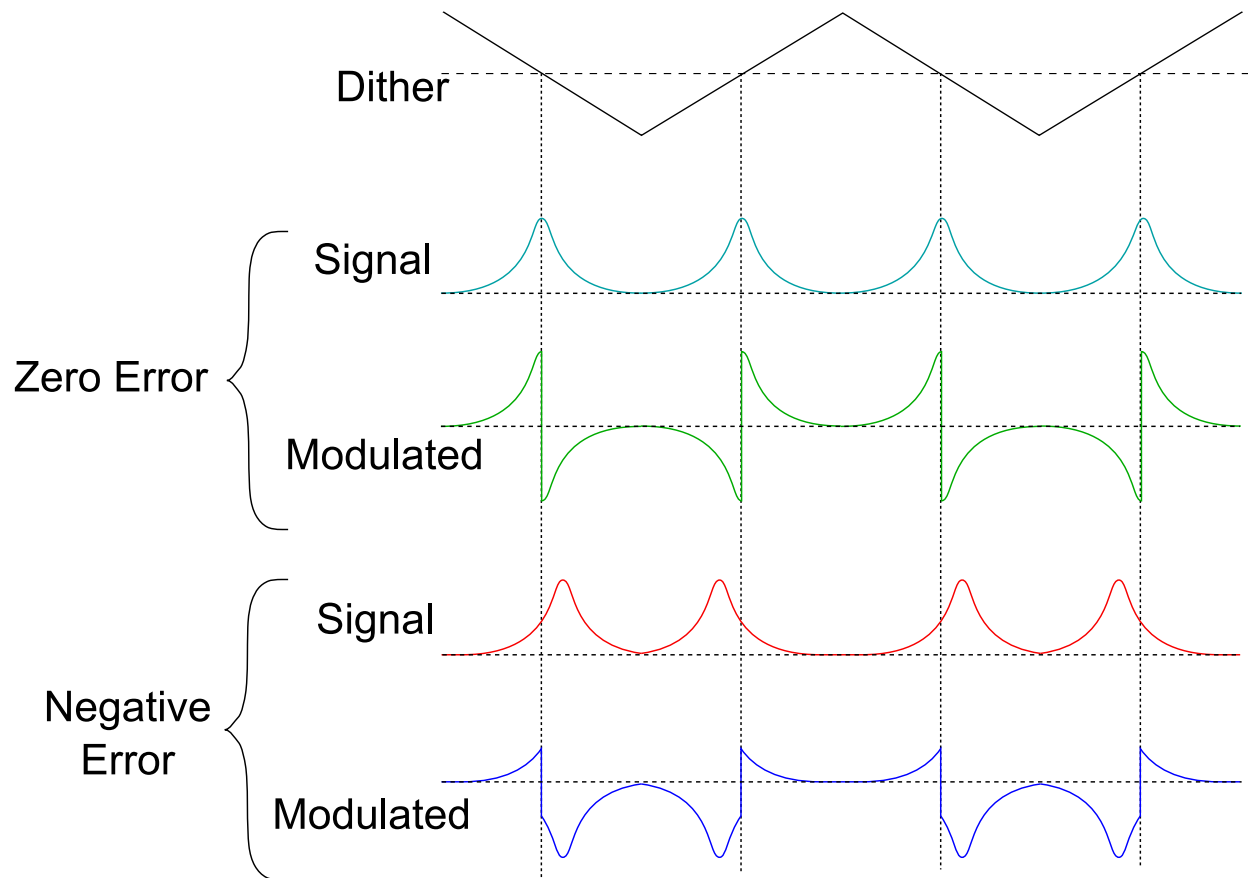


Figure E.1: The central idea of the peak lock circuit. When the laser is locked, the integral of the modulated signal is zero.

# Appendix F

## Automatic Laser Pointing Stabilizer (ALPS) Manual

### F.1 Optics

The ALPS is designed to keep the beam position on a detector fixed. To do this, an optics setup must be chosen to set up the beam optics, including PZT mirror mounts and detector so as to make sure that stabilizing the position on a detector will stabilize the beam in space. The amount of laser power on the detectors needs to be between  $730 \mu\text{W}$  and  $170 \mu\text{W}$  for best operation (in the case of a focused beam, lower power must be used). Four suggested setups are shown in Fig F.1. The setup in Fig F.1(a) is suggested for high power setups, where leakage through the mirrors is near the reliable operating range of powers. Figure F.1(b) is suggested when beam powers are not sufficient to use the high power setup. The setup in Fig F.1(c) can be useful when integrating the ALPS into an existing setup and control needs to be as near to the target as possible. Figure F.1d has been used with good results, but is very sensitive to matching the detector position to the focal point, where the beam is to be stabilized; not matching these distances, shown as “a” in the figure, can lead to *worse* stability of the laser at the focus than without the pointing stabilizer.

**For a two detector setup, the criteria for stability are that the optical path length between PZT2 and Detector2 is long compared to the optical path length between PZT2 and Detector1, and that the optical path length between PZT1 and Detector1 is not significantly shorter than the optical path length between PZT1 and Detector2.** If possible, it is also desirable to have both detectors *after both* PZT mirrors as in Fig F.1(b). If this is not possible, or is not desirable, for instance if setup (a) is used, Detector1 should be as close to PZT2 as possible.

Since there are four degrees of freedom in a beam, there need to be four controls to stabilize the beam in all degrees of freedom. A PZT mirror can provide two controls, so two PZT mirrors are needed for full stability. Likewise, to detect motion in the four degrees of freedom, two detectors are needed.

The PZT mirror mounts are designed to accept a quadrant detector in the fixed plate.



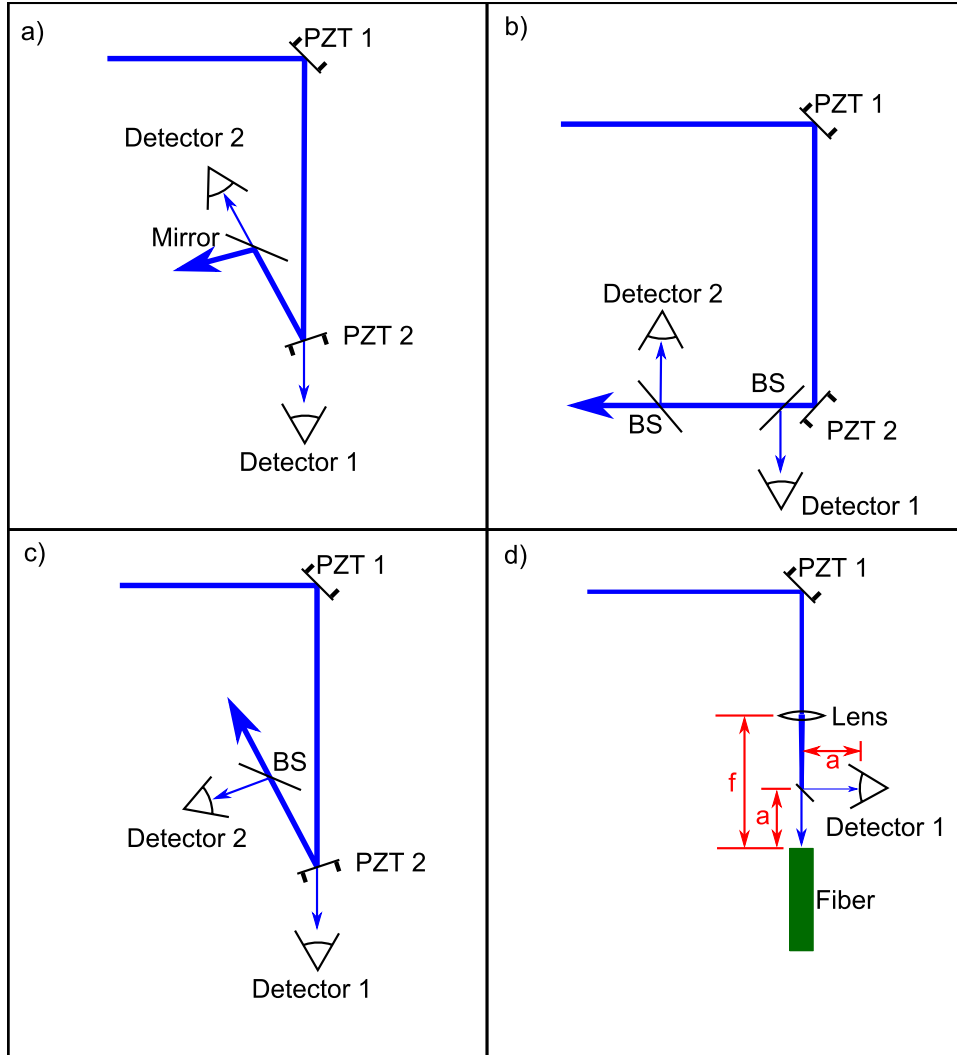


Figure F.1: Suggested optics configurations for the ALPS system. **(a)** is suggested if the power in the beam is sufficient to put between  $730 \mu\text{W}$  and  $170 \mu\text{W}$  of power on the detectors by leaking through the mirrors. **(b)** is suggested otherwise. **(c)** is useful in some cases where tight control is required, or another mirror cannot be inserted. **(d)** can be used when the beam is focused, and the direction of propagation at the focus is not important. Care must be taken in case **(d)** to make sure the detector is not burned.

The detector is fixed in place with a set screw. However, the PZT mirror mounts do not have clearance for a beam at 45 degrees to the normal to pass through the mirror and mount. If the beam is to pass through the mirror and the mount to get to the detector, the beam must be near normal incidence.

The detector is shown in Fig F.2. It should be mounted with the indicated pin below the other pins, as shown.

## F.2 Connection

Connecting the ALPS is relatively simple, as nearly all connectors are labeled, as shown in Fig F.3. All connections are made in the back of the box. Power is supplied with a standard HP style power cable. Each unit contains two separate systems, each consisting of a detector and PZT mirror mount; these two systems are called “1” and “2”. The detectors are connected to the DB-9 connectors labeled “DETECTOR 1 INPUT” or “DETECTOR 2 INPUT”. The PZT mirrors are connected so that the actuator controlling the horizontal motion of the beam spot on the detector is connected to “X1 PZT” or “X2 PZT”, while the vertical motion controlling actuator is connected to “Y1 PZT” or “Y2 PZT”. A scope can be connected to “X1 POSITION” and “Y1 POSITION” or “X2 POSITION” and “Y2 POSITION” to monitor the position of the beam as detected by detector 1 or 2 respectively. This is especially well suited to looking at the signals on a scope in “XY” mode. The “OVER RANGE” outputs produce TTL level signals of  $\sim 5$  V when the numbered ALPS board has reached its output limits and is thus no longer able to correct the beam position. This output can be connected, with appropriate electronics to a shutter to block the beam when this happens, so as to prevent damage to any sensitive optics such as fibers. *If a shutter is used it is important to put the shutter downstream of the detectors. If the beam is not hitting the detector at all, the ALPS will output this signal, which will keep the shutter closed.*

## F.3 Operation

Operating the ALPS, is a relatively simple affair. Most of the controls and the indicators are on the front panel, shown in Fig F.4. The panel meters, labeled “X” and “Y” give the voltage applied to the PZT divided by 15. This puts the range of values shown at 0 – 10 V. The meters display the voltages for only one PZT mirror at a time, and the switch to the left of the meters, labeled “METER SELECT” controls for which PZT mirror mount the meters are measuring the voltages.

The rest of the controls and indicators are for each individual pointing stabilizer system. There is an LED bar indicating the amount of optical power on the detector, compared to the ideal range. If too much power is incident on the detector, the “OVERPOWER” light will turn on. If there is not enough light on the detector, the “UNDERPOWER” light will turn on.

The switches turn the feedback loop on and off. There is a separate switch for x and y. When the lock is off, the knobs labeled “MANUAL” control the voltage applied to the PZT

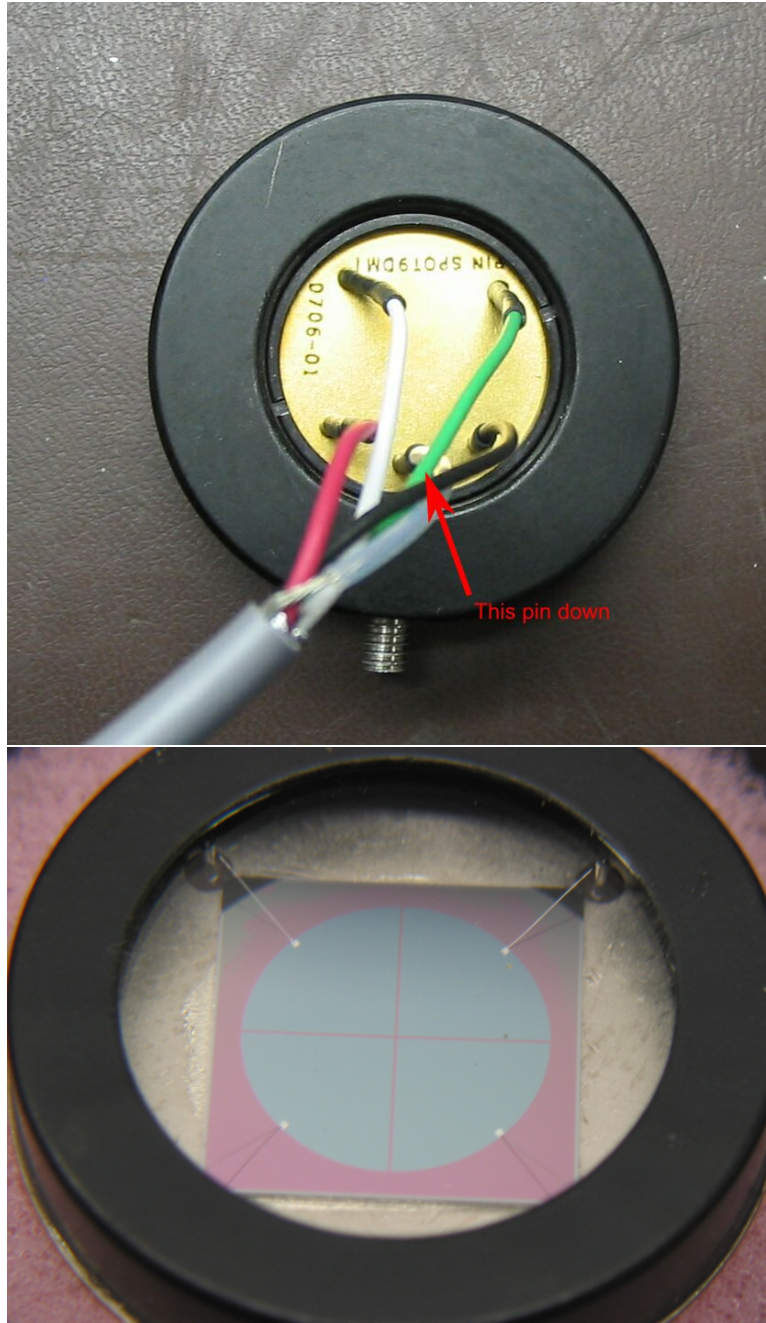


Figure F.2: The ALPS detector back and front. The indicated pin should be the lowest pin.



Figure F.3: Back panel of the ALPS



Figure F.4: Front panel of the ALPS

actuators, allowing the user to fine tune beam position. When the lock is on, the stabilizer will attempt to put the beam on the “origin” of the detector. The location of the origin on the detector is controlled by the “OFFSET” knobs. When the knobs are set at the middle of the range, meaning the top number is 5 and the dial reads zero, the origin of the detector is at the center of the detector.

The polarity of the feedback loop must be correct in order to properly stabilize the beam. The switches for the polarity are located on the back panel and are labeled “INVERT”. If the polarity is wrong, the stabilizer will anti-lock for any axis that has the wrong polarity. If this happens, toggling the appropriate “INVERT” switch will solve the problem. The x polarity will need to be changed any time a mirror is inserted into the path between the PZT mirror mount and the detector. The y polarity will usually not need to be changed once initially set.

In most cases, the PI feedback loop gains will work well with the tunings provided at the time of construction. In some cases, these gains will need to be adjusted. This adjustment is done by way of potentiometers inside the box, on the pointing stabilizer boards. There is a separate potentiometer for each of the gains, proportional for x and y, and integral for x and y. See Fig F.5 for locations of the potentiometers.

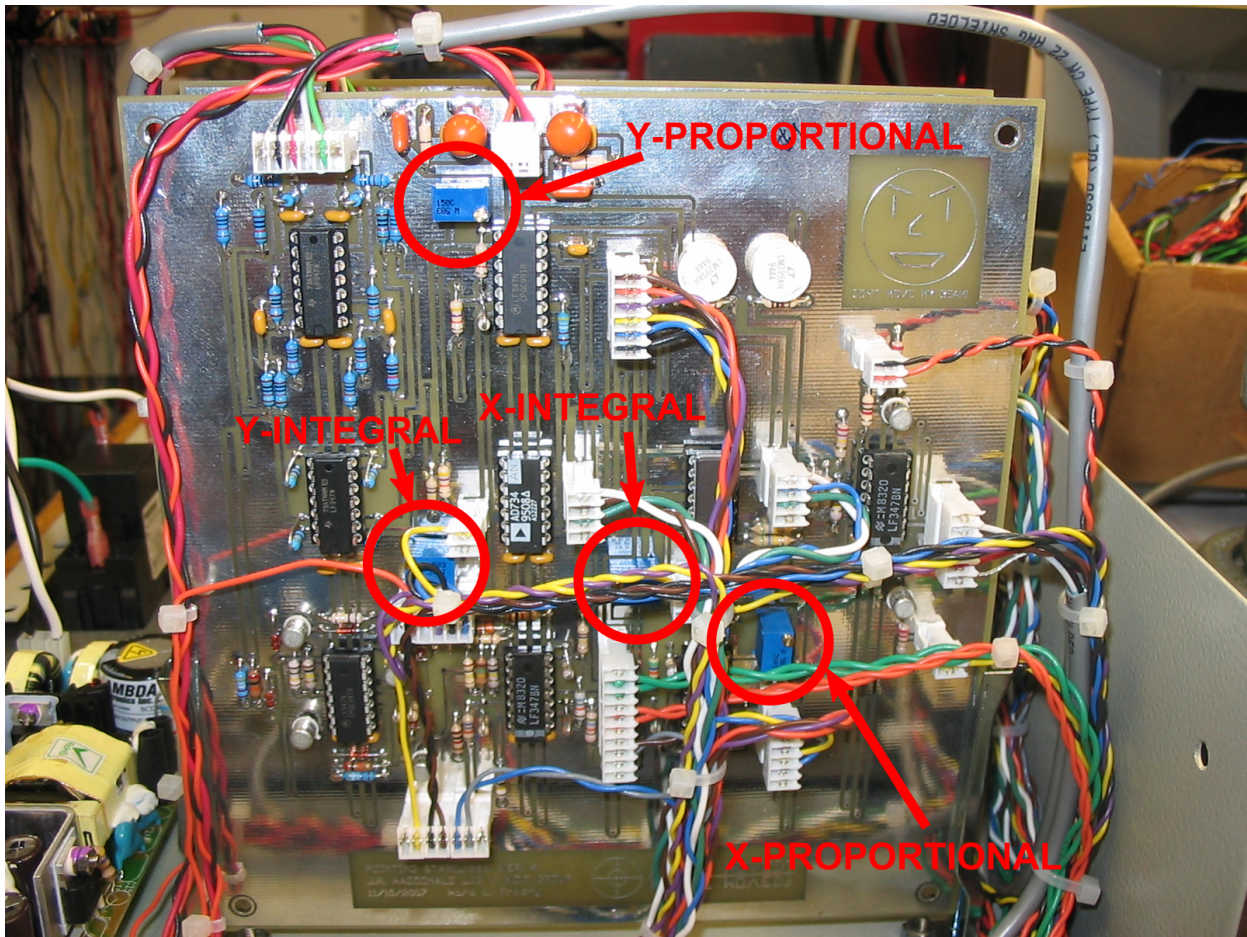


Figure F.5: The ALPS circuit board. The potentiometers for tuning the PI feedback loops are indicated.